

AD-A171 526

INVESTIGATION OF MILLIMETER WAVE PROPAGATION IN THE
ATMOSPHERE(U) NATIONAL OCEANIC AND ATMOSPHERIC
ADMINISTRATION BOULDER CO WA. S F CLIFFORD ET AL.

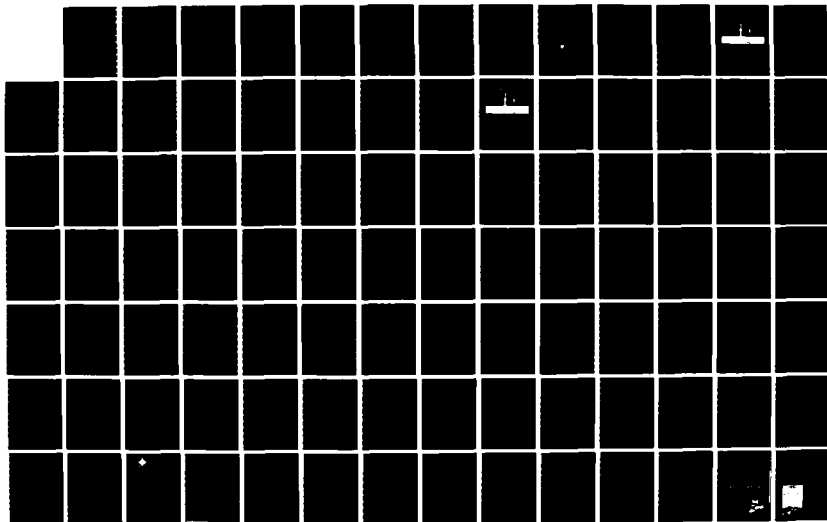
1/2

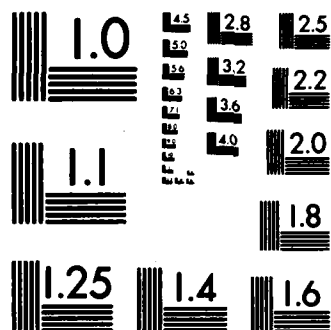
UNCLASSIFIED

18 JUL 86 ARO-18029. 18-GS ARO-55-01

F/G 20/14

NL





XEROCOPY RESOLUTION TEST CHART
NATIONAL BUREAU OF STANDARDS-1963-A

INCLASSIFIED

SECURITY CLASSIFICATION OF THIS PAGE (When Data Entered)

2

AD-A171 526

REPORT DOCUMENTATION PAGE		READ INSTRUCTIONS BEFORE COMPLETING FORM
1. REPORT NUMBER ARO 18029.18-GS	2. GOVT ACCESSION NO. N/A	3. RECIPIENT'S CATALOG NUMBER N/A
4. TITLE (and Subtitle) Investigation of millimeter wave propagation in the atmosphere.		5. TYPE OF REPORT & PERIOD COVERED Final Report 15 Sep '81 - 20 Mar 86
		6. PERFORMING ORG. REPORT NUMBER
7. AUTHOR(s) S. F. Clifford, R. J. Hill, and W. P. Schoenfeld		8. CONTRACT OR GRANT NUMBER(s) ARO55-81, 21-82, 123-83, 127-84, 122-85
9. PERFORMING ORGANIZATION NAME AND ADDRESS Propagation Studies, R/E/WPI NOAA/ERL/Wave Propagation Laboratory 325 Broadway, Boulder, CO 80303 406 292		10. PROGRAM ELEMENT, PROJECT, TASK AREA & WORK UNIT NUMBERS
11. CONTROLLING OFFICE NAME AND ADDRESS U. S. Army Research Office Post Office Box 12211 Research Triangle Park, NC 27709		12. REPORT DATE July 18, 1986
		13. NUMBER OF PAGES
14. MONITORING AGENCY NAME & ADDRESS (if different from Controlling Office)		15. SECURITY CLASS. (of this report) Unclassified
		15a. DECLASSIFICATION/DOWNGRADING SCHEDULE
16. DISTRIBUTION STATEMENT (of this Report) Approved for public release; distribution unlimited.		
17. DISTRIBUTION STATEMENT (of the abstract entered in Block 20, if different from Report) NA		
18. SUPPLEMENTARY NOTES The view, opinions, and/or findings contained in this report are those of the author(s) and should not be construed as an official Department of the Army position, policy, or decision, unless so designated by other documentation.		
19. KEY WORDS (Continue on reverse side if necessary and identify by block number) Millimeter waves, turbulence, meteorology, propagation, scattering severe weather, boundary layer, fluxes, absorption, refractive-index fluctuations		
20. ABSTRACT (Continue on reverse side if necessary and identify by block number) This report documents the results of five years of research conducted on the propagation of millimeter waves through the atmospheric surface layer. At a site in Flatville, Illinois, radiation in the frequency range from 116 GHz to 230 GHz was propagated along at 1.4 km horizontal path instrumented with multiple meteorological sensors to characterize the state of the atmosphere. The millimeter wave beam propagated at a height of 3.7m to a receiver van that had four receiver antennas spaced in a non-redundant manner to allow measurements of amplitude, phase difference and mutual coherence at spacings from—		

DTIC
ELECTE
AUG 27 1986
S A

DTIC FILE COPY

UNCLASSIFIED

SECURITY CLASSIFICATION OF THIS PAGE(When Data Entered)

1.43m to 10m. Comparisons between the clear air propagation data and theory showed close agreement.

UNCLASSIFIED

SECURITY CLASSIFICATION OF THIS PAGE(When Data Entered)

ARO 18029.18-65

INVESTIGATION OF MILLIMETER WAVE
PROPAGATION IN THE ATMOSPHERE

FINAL REPORT

S.F. CLIFFORD
R.J. HILL
W.P. SCHOENFELD

JULY 18, 1986

U.S. ARMY RESEARCH OFFICE

CONTRACT NUMBERS: FUNDING DOCUMENTS
ARO55-81, 21-82, 123-83, 127-84, 122-85

PROPAGATION STUDIES GROUP
WAVE PROPAGATION LABORATORY
NATIONAL OCEANIC AND ATMOSPHERIC ADMINISTRATION

APPROVED FOR PUBLIC RELEASE;
DISTRIBUTION UNLIMITED

NOTICE

The view, opinions, and/or findings contained in this report are those of the author(s) and should not be construed as an official Department of the Army position, policy or decision, unless so designated by other documentation.

CONTENTS

	Page
I. RESEARCH HIGHLIGHTS.....	1
II. DATA BASE USER GUIDE.....	11
III. LIST OF PUBLICATIONS ON THE NOAA/GIT RESEARCH PROJECT (NOAA CONTRIBUTIONS ONLY).....	74
IV. ACKNOWLEDGMENTS.....	77
V. APPENDICES.....	79

[illegible]

I. RESEARCH HIGHLIGHTS

In August of 1981, we recieved approval from the Army Research Office (ARO) to conduct research on the propagation of millimeter waves through the atmospheric boundary layer. Georgia Institute of Technology (GIT), whose expertise in millimeter wave sources and receivers is reknown, were co-investigators. The GIT responsibility was to develop transmitters and receivers in accordance with specifications in our jointly derived experiment design. Investigators the National Oceanic and Atmospheric Administration designed and implemented the meteorological support stations and would perform the bulk of the data analyses and the theoretical support. The overall mission of the experiment was to establish a data base for propagation of millimeter waves at a variety of frequencies in a well-documented, wide-variety of atmospheric conditions.

Before embarking on such an ambitious research program as the NOAA/GIT experiment, we performed more than one year of preparatory research and site selection. This latter task was accomplished after an examination of more than twenty sites (see Table I) over a period of eighteen months. This was necessitated because of the stringent requirements necessary for efficient, economic operation and to ensure the correct conditions for the applicability of the Monin-Obukov similarity theory, that allows us to accurately characterize the boundary layer processes attendant at such a site (Table II). We settled on an exceptional site at Flatville, Illinois (see Fig. 1) and signed contracts with the affected farmers in early 1983. At that time, the equipment was deployed on the 1.4 km Flatville site as depicted in Fig. 2.

Before selecting instruments for final deployment, we performed preliminary tests on both the millimeter-wave¹⁻⁵ and atmospheric instruments.^{4,6,7} A major result of the NOAA effort was to redesign the Lyman-alpha humidimeter⁶ to improve its frequency response. Our design changes were adopted by the manufacturers. During this period GIT successfully designed and constructed the transmitter and receiver vans and antennas. This was no simple task because of the stringent receiver stability requirements of maintaining less than one wavelength of random motion of the receiver array over the approximately twenty-six thousand wavelength long array. The final design incorporated a 13-m I-beam, the supports of which were bolted to a concrete pad beneath the receiver van (see Appendix I).

TABLE I: SITE SURVEY

FIELD SITE CANDIDATES VISITED -

- Illinois River Valley near Havana, Illinois
- Kilbourne, Illinois
- Chanute AFB, Rantoul, Illinois
- Flatville, Illinois
- Champaign-Urbana, Illinois
- Sandusky, Ohio
- Wallops Island, Virginia
- Redstone Arsenal, Huntsville, Alabama
- Great Bend, Kansas
- Sikeston, Missouri
- Otis Air Force Base, Massachusetts
- Kennedy Space Flight Center, Cape Canaveral, Florida

FIELD SITE CANDIDATES RULED OUT BY TELEPHONE -

- O'Neill, Nebraska
 - North Air Field (USAF), North, South Carolina
 - Aberdeen Proving Ground, Maryland
 - Moody AFB, Valdosta, Georgia
 - Robins AFB, Warner-Robins, Georgia
 - Fort Rucker, Alabama
 - Fort Stewart, Georgia
 - Fort Benning, Georgia
 - Morris AAF, Fort Gillem, Atlanta, Georgia
 - Whiteman AFB, Missouri
 - Eglin AFB, Florida
-

TABLE II: SITE EVALUATION FACTORS

Topography - flatness
 Fetch - lack of trees, direction of prevailing wind
 Annual precipitation and its predictability
 Occurrence of snow and fog
 Availability of electrical power
 Access roads
 Land use: crops and their uniformity over section
 Number of owners involved
 Cost to use
 Security
 Fences and other interference objects
 Telephone lines
 Accessibility via common carrier
 Temporary housing, e.g., distance to motels
 Storage facilities
 Proximity to mm-tech facilities, NWS observers

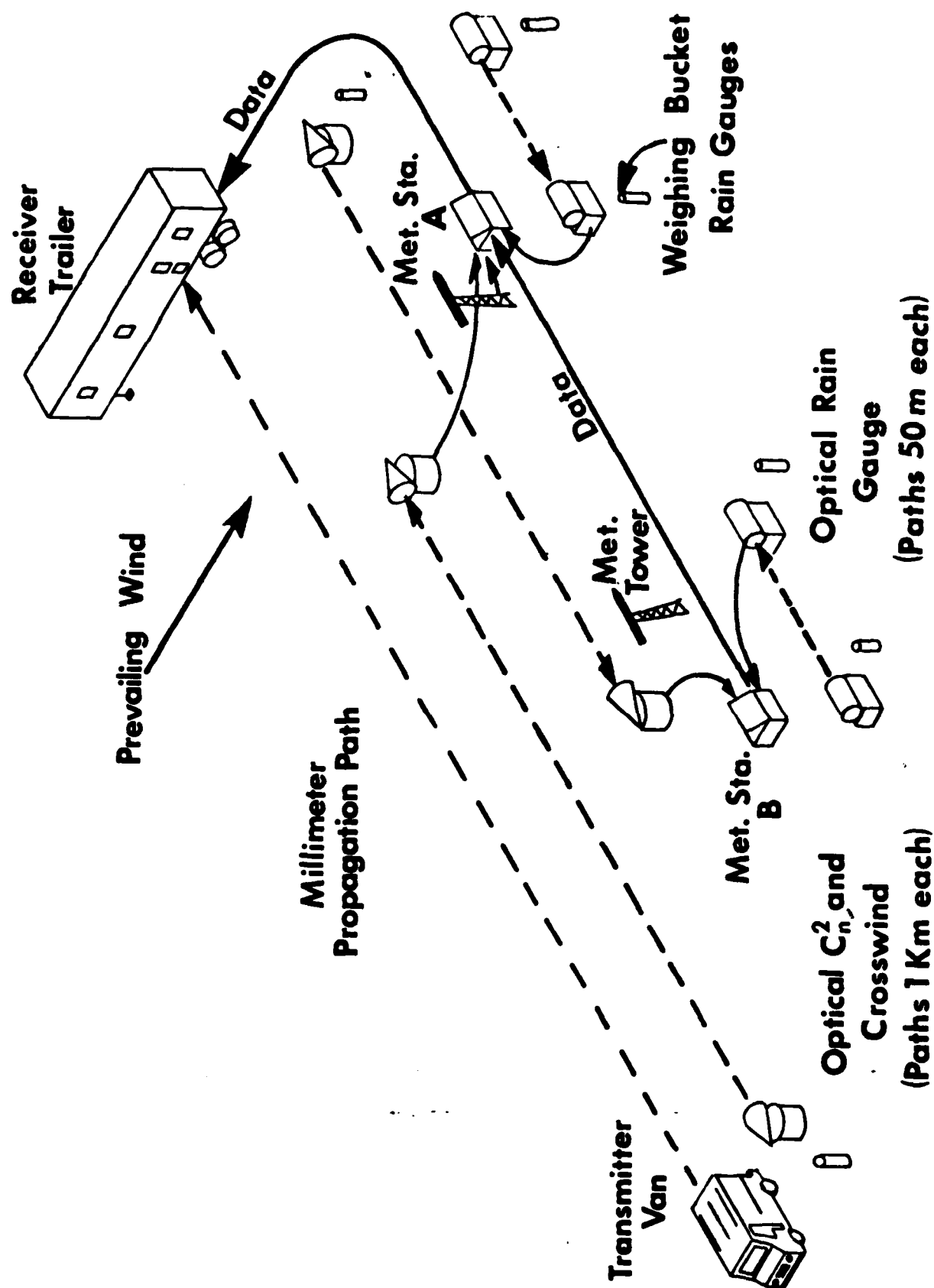


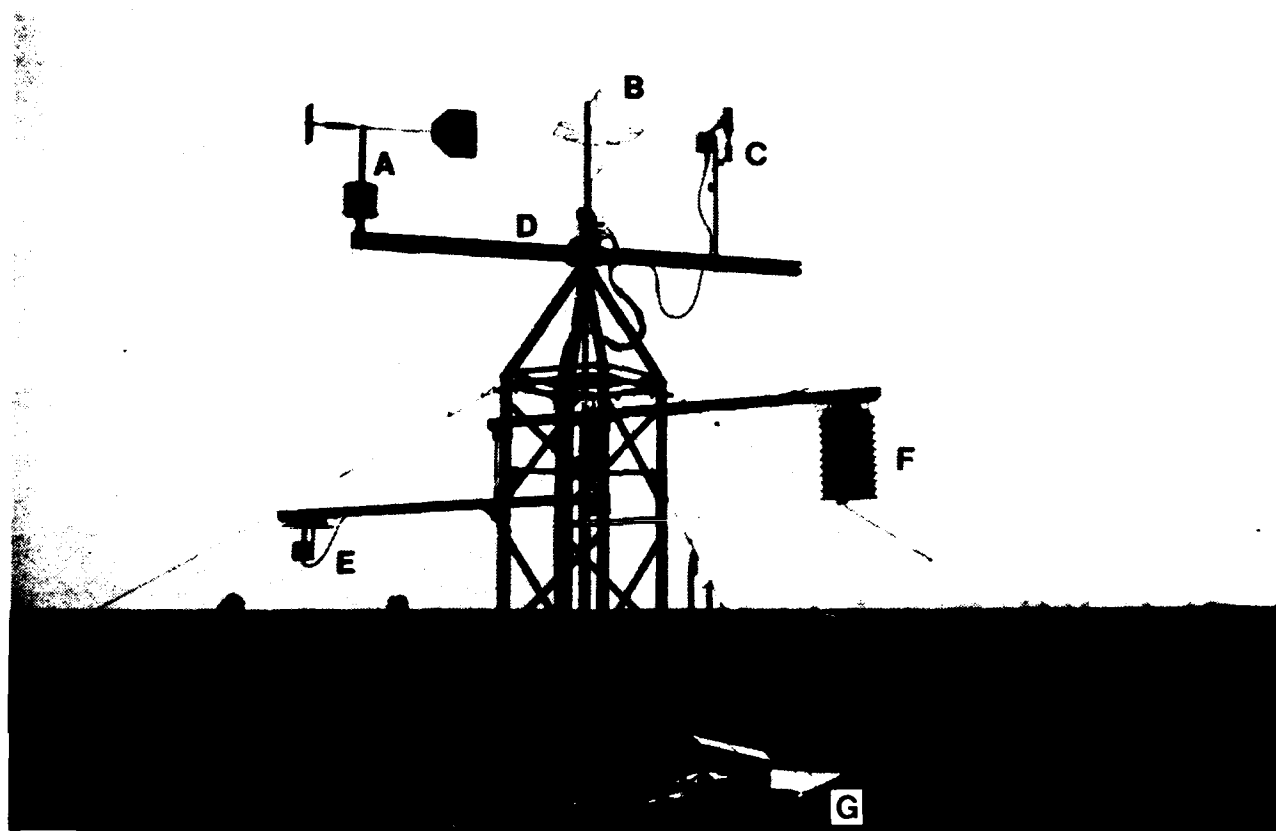
Figure 2.

After the redesign of the Lyman-alpha humidimeter, a preliminary test was run to choose the optimum available humidity sensor from a group of candidates.⁷ Another equally important aspect of this work was to gain familiarity with the instruments in a boundary layer experiment and to see if we could eliminate the need for the labor-intensive radio refractometer needed to measure the refractive-index fluctuations in the near millimeter wave range. It was concluded that it was possible to derive the refractive-index-fluctuation statistics in terms of C_T^2 , C_Q^2 and C_{TQ} from our theoretical calculations (Appendix II and ref. 8), using a combination of Lyman-alpha humidity and fine-wire temperature measurements, with sufficient accuracy for our purposes. A noteworthy result of the preliminary experiment⁷ was the strong degree of absolute correlation between the humidity and temperature fluctuations. The correlation nearly +1 during the daytime when both temperature and humidity gradients were negative and nearly -1 when the temperature gradient reversed a night due to radiational cooling of the ground. The transition periods were quite brief on the order of 15 minutes.

Also during the preparation phase, we made progress on theoretical studies of propagation of millimeter beam waves in complex refractive media⁹ and the use of optical and millimeter wave devices to measure surface layer fluxes.¹⁰ This latter work is significant because we believe that a combination visible, infrared and millimeter wave system can give path-averaged values of heat, momentum and moisture fluxes that may be more representative and certainly more quickly measured than results using conventional in situ devices. This technique would be extremely advantageous for use at inaccessible sites such as irregular terrain or over-water paths. To test the ideas proposed in Ref. 10, was one of the NOAA groups' major goals.

At the conclusion of the above research, we decided on a set of meteorological instruments to be deployed on site at Flatville at the two locations along our 1.4 km propagation path shown in Fig. 2. Table III lists the available instruments and their associated data recording channel numbers. The data flowed to recorders in the receiver trailer via a buried fiber-optic cable from both Met. Station A and Met. Station B. Each station consisted of the standard in situ instrumentation listed as channels 0-12 and deployed on the meteorological tower as shown in Fig. 3. In addition, three optical remote sensors, channels 13-15, gave path-averaged values of path-crosswind, optical refractive-turbulence strength and rain rate.

Meteorological Instrumentation Tower



- A: Propeller-vane anemometer
- B: Three-axis sonic anemometer with wire temperature sensor in center
- C: Lyman- α hygrometer with wire temperature sensor in center
- D: Rotatable boom
- E: Vaisala humidity probe
- F: Aspirated psychrometer
- G: Electronics cabinet

TABLE III. METEOROLOGICAL INSTRUMENTS

Channel #	Station A	Station B
0	Lyman- α humidimeter	Lyman- α humidimeter
1	T' (temperature sensor) for Ly- α	T' (temperature sensor) for Ly- α
2	T' for sonic anemometer	T' for sonic anemometer
3	psychrometer	psychrometer
4	disdrometer	Vaisala temperature probe
5	Vaisala relative humidity probe	Vaisala relative humidity probe
6	sonic anemometer U	sonic anemometer U
7	" " V	" " V
8	" " W	" " W
9	angle encoder	angle encoder
10	barometer	pyranometer
11	propellor	propellor
12	vane	vane
13	optical cross-wind	optical cross-wind
14	optical C_n^2	optical C_n^2
15	optical rain gauge	optical rain gauge

One of the optical rain gauges gave both rain rate and drop-size distribution (channel 4, station A). The rain sensor data were compared with a set of six weighing-bucket rain gauges deployed as shown in Fig. 2. The optical rain sensor is discussed in detail in Appendix III. On site we used a 50-m laser path. By the spring of 1983 we were recording both millimeter wave and meteorological data.¹¹ Once on site we carried out five experimental phases. These data-taking sessions were in June-July 1983, Nov.-Dec. 1983, Feb.-March 1984, June-July 1984, and Feb.-March 1985. These varied sessions allowed us the maximum opportunity to take multi-wavelength data during clear-air, rain, fog, sleet and snow.¹²⁻¹⁶ More accurate dates and precise millimeter frequencies are shown in Table IV.

Fundamental theoretical work on propagation theory¹⁷ was undertaken to verify that the mutual coherence function (MCF), derived for optical waves propagating through the atmosphere, could be applied to the millimeter-wave case. Optical waves readily satisfy the condition $\lambda \ll \ell_0$, where λ is the wavelength and ℓ_0 the smallest size refractive-index irregularity in the medium, necessary for the validity of the parabolic (narrow-angle scatter) approximation, millimeter waves do not. Reference (17) proves that there is a broader range of applicability to the optical result and the optically derived MCF applies in the

TABLE IV. SCHEDULE OF FLATVILLE OBSERVATION PHASES

Session I:	4 June - 21 July 1983		
	Tapes 3 - 15:	f = 116.300 GHz	11 - 16 July
	Tapes 16 - 29:	f = 172.910 GHz	17 - 20 July
Session II:	31 Oct. - 10 Dec. 1983 (Break: 19-29 Nov.)		
	Tapes 2 - 32:	f = 116.300 GHz	11 Nov - 2 Dec
	Tapes 33 - 45:	f = 173.001 GHz	3 - 6 Dec
Session III:	5 Feb. - 9 March 1984		
	Tapes 1 - 33:	f = 142.000 GHz	11 - 20 Feb
	Tapes 34 - 75:	f = 116.300 GHz	22 Feb - 2 Mar
	Tapes 76 - 93:	f = 142.000 GHz	2 - 6 Mar
Session IV:	31 May - 4 July 1984		
	Tapes 1 - 20:	f = 142.004 GHz	8 - 18 June
	Tapes 21 - 22:	f = 118.754 GHz	19 June
	Tapes 23 - 24:	f = 120.750 GHz	20 June
	Tapes 25 - 26:	f = 118.754 GHz	20 June
	Tapes 27 - 65:	f = 142.004 GHz	21 - 30 June
	Tapes 66 - 70:	f = 173.005 GHz	1 - 2 July
	Tapes 71 - 76:	f = 172.620 GHz	3 July
Session V:	31 Jan. - 24 Mar 1985 (Break: 22 Feb. - 4 Mar.)		
	Tapes 1 - 13:	f = 229.250 GHz	8 - 11 Feb
	Tapes 14 - 78:	f = 230.441 GHz	11 Feb - 18 Mar

millimeter wave region. This was confirmed in our subsequent data. Further theoretical work on absorption sharpened our understanding and the accuracy of absorption spectrum¹⁸⁻²⁰ in general, and the refractive and absorptive behavior of the atmosphere and its constituent gases in the millimeter wave region in particular.^{18,19}

After collecting 291, thirty-nine-minute magnetic tapes, each containing 60 channels of either meteorological or millimeter wave data at more than 10 different frequencies, a massive data collection, handling and processing problem presented itself. The processing architecture²¹ is documented in detail in Appendix IV and in Reference 22. Procedures used to pre-process data to reduce noise problems^{23,24} and algorithms to process rain data²⁵ were developed. The final result is a database²⁶ of answer files where time series, spectra, varian-

ces and higher order moments, probability density functions etc. of both millimeter-wave and meteorological data are stored for ready access by the NOAA-GIT team or other interested users. This so-called users guide is the subject of Section II of this report.

Although the database has been tapped only modestly, we have performed several theoretical studies and tested them using our Flatville data. References 27 and 28 compare the observed clear-air, millimeter-wave, amplitude and phase difference spectra with a theoretical model derived by the authors from work based on single-scatter theory. The results show a very close agreement between theory and experiment and also indicate that the millimeter wave link can act as an accurate monitor of the path crosswind in a fashion analogous to our on-site optical remote sensors shown in Fig. 1. Other work analyzed phase difference power spectra of infrared waves, to determine their sensitivity to rain rate and eventual use as a long-path rain-rate monitor.²⁹ Another study³⁰ reported a detailed analysis of an oscillatory rain rate fluctuation and showed it correlated nearly perfectly with intensity fluctuations observed simultaneously on the millimeter wave link. Other work, conducted primarily by the GIT staff, analyzed the Flatville observations for effects of severe weather, fog and snow.^{31,32} A recent paper³³ compares the behavior of variances, structure functions, and probability distribution functions of amplitude and phase differences, and mutual coherence functions, with the first-order-single-scatter theory prediction using the observed meteorological data, and finds excellent agreement between theoretical prediction and experiment in nearly all respects. Finally, Ref. 34 describes the first demonstration of a successful derivation of the fluxes of heat, momentum and moisture from multi-wavelength scintillation data. These results were compared with directly measured fluxes using the meteorological-station data, and good agreement was found. This was one of the key results of the experiment and further work in verifying the results under a wide variety of weather conditions is under way.

Although we have just begun to tap the data, many theoretical predictions have been confirmed and many tantalizing new results observed. The ultimate value of the database will be determined by interested researchers both inside NOAA-GIT and outside agencies. We have taken great pains to make the database accurate, accessible and available. If Army and other workers will use the results of our efforts and expand the research activity, we are convinced the

Flatville data set will be more than worth the extraordinary effort it took to produce it.

II. DATA BASE USER GUIDE

II.1 General Descriptions of the Data Base

The Data Base described herein is a collection of statistical quantities, probability distributions, and spectra of data taken by the NOAA-GIT mm wave experiment held in Flatville, Illinois between October 1983, and March 1985. The purpose of the study is to provide a general purpose scientific data base which contains quantities essential to the investigation of millimeter wave propagation in the turbulent and turbid atmosphere. Thus, the data base necessarily contains meteorological data designed to complement the millimeter wave data. A detailed description of the experiment and data analysis is described in Ref. 21 (Appendix IV). The meteorological data contained in the database is weather dependent because of the extended use of state-of-the art instrumentation. For example; temperature fluctuations were measured using 2 micron diameter platinum wires, and humidity fluctuations were measured using Lyman-alpha hygrometers. During precipitation events, these instruments were covered because the rain drops would break the fine wires, and the excess moisture would saturate the Lyman-alpha gap rendering these data meaningless. In such circumstances, structure parameters are not calculated and only macroscopic meteorological data is entered in the database. These data are derived from instruments which respond too slowly to detect turbulence scales.

The database resides on the CYBER 180/855 at the National Bureau of Standards in Gaithersburg, Maryland. It is not portable because we have taken advantage of vendor software. We decided to do so after learning of NOAA's commitment to the purchase of CDC hardware and believe that this data will be available for a long time to come.

The system design of the data base is "user friendly"; which in this case has literal meaning...all items are accessed by their name. Furthermore, one may select data which falls into a predefined category. For example, one may wish to collect all the mutual coherence functions (a complex quantity) for all blowing snow data at a specific mm wave frequency. This is done by setting keys which selectively gather records from which data is extracted by name. This report explains how to do this.

The data base is a specially structured random access file in the sense of a FORTRAN '77 definition. The special parts of the file are twofold. On the first part, software provided by CDC Corp. was used to initialize and make entries to the file making it a true database. The second part of it's special nature is a concept of an index and dictionary we developed and built into the file. The index is akin to the table of contents one finds in a standard reference book in that it contains lists of categories that can be used to selectively accumulate data from records. The dictionary contains all the data names, their location and length. The index and dictionary items are predefined. If one requests a data category, and/or a data item which is not defined, the software will stop softly describing the erroneous entries.

An optional product of our data base interrogation software is a smaller file containing the categorical items requested by the user. This file can be sequential access with records of varying lengths, or it can be random access. The random access option produces an ANSI standard FORTRAN '77 DIRECT ACCESS* file; it is portable only to the extent that the CYBER 60-bit words can be properly converted for the use by the recipient system. The random access file feature is intended for, but not restricted to, use on our, or other, CYBER installations.

The sequential access file option can be formatted, or unformatted. An unformatted sequential file contains positionally placed binary data and has the advantage that precision is maximized, but the disadvantage that conversion software must be used to move the data to another system. Formatted data however, transfers most easily using a wide variety of commercially available text file communications software. We recommend that investigators transferring the data to a smaller personal computer use the formatted sequential access option.

The database can be queried for named data belonging to categories of items that are defined in the index. The user is not restricted to one category, or

* DIRECT ACCESS IN FORTRANese, but we avoid this terminology because of the special definition of DIRECT ACCESS files when one refers to a CYBER.

one index. There are seven indices each with several categories. There is complete flexibility for the user to retrieve data from a single, or from a range of categories in any combination of the seven indices.

Arrays are stored in contiguous regions of the record. The FORTRAN default memory organization, columnwise storage, is used. Since the data are known to the system by name, the user only has to allocate space to the array items and let the interrogation software fill the arrays. All variable sizes are specified in Appendix A.

As will be seen below, the Fourier transforms are multifaceted, each face with it's own subset of items within a namelist. The namelists follow patterns which allows the user to reduce his inventory of variables. This feature will often improve the user's computational efficiency.

Also stored in the records are normalized Probability Density Functions (PDF's). These arrays have the obvious property that the whole PDF must be used. There are thirteen one-dimensional PDF's normalized to unit area, and two joint PDF's normalized to unit volume.

Where complex quantities are stored, we have elected to separate the real and imaginary parts because often an investigator is interested in one, and not the other. This was also computationally efficient by eliminating the overhead caused by computing complex quantities. Thus vectors which represent complex quantities are stored as the Re, then the Im parts separately, and not as vectors of complex pairs.

We have included for convenience an integer function which returns a value that defines the most efficient size array to declare for reading records from the database. Using this feature will optimize your program's I/O.

At the simplest level, a single subroutine call will retrieve all the requested data and put them into a smaller file. The user needs only to specify which items he wants transferred, and those items are placed in records in the order specified. There is one output record for data base record which meets the selection criteria.

More sophisticated use of the data base interrogation software requires allocation of working storage. Since our design gets data by names according to some rule, there are seven required arrays and a name buffer of user particular size.

II.2 The GIT mm Wave Propagation Experiment

The GIT millimeter-wave data consist of 28 channels recorded at 100 Hz. (In this report "millimeter-wave" is abbreviated as mm-wave.) Figure 4 shows the arrangement of receiver antennas as viewed from the transmitter; the antennas are designated by a number. There are six possible horizontally separated antenna pairs, each with a different spacing. The antenna pair numbers and

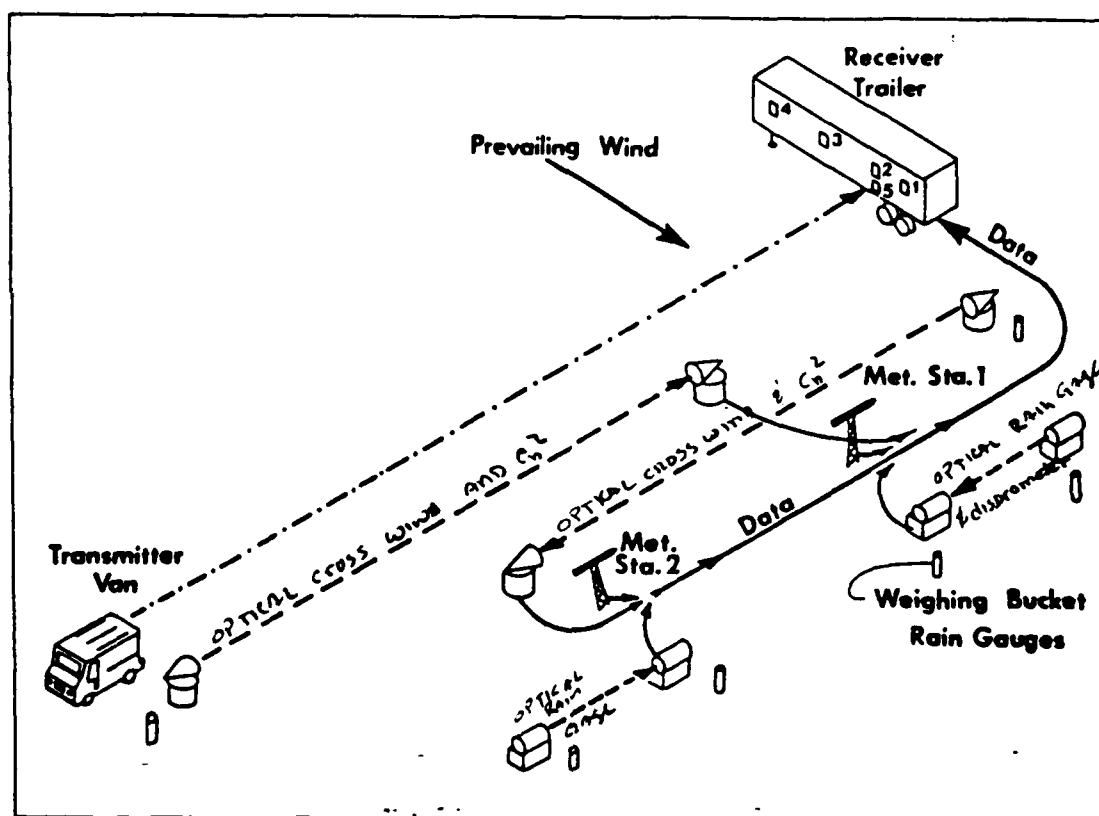


Figure 4. The instrument positions at the experiment site. The dashed and dotted line denotes mm-wave propagation path (1.4 km); the long-dashed lines, the optical propagation paths (1 km each); and the short-dashed lines, the optical rain gauge paths (50 m each). Solid lines show the flow of micrometeorological data to the data acquisition system in the receiver trailer. Antennas are numbered 1 to 5 in the receiver trailer. The relative positions shown are drawn approximately to scale.

their spacings are given in Table V. For a few experiment runs, the fifth antenna, below antenna 2 was used in place of antenna 4; the objective was to observe anisotropy and multipath effects. As described in Ref. 21, the data yield the intensity at all four antennas, the phase difference between all six antenna pairs, as well as some instrumentation checks known as figures of merit.

Table V. Antenna pairs

Pair number	Antenna pair	Spacing in meters
1	1 & 2	1.43
2	1 & 3	4.29
3	1 & 4	10.00
4	2 & 3	2.86
5	2 & 4	8.57
6	3 & 4	5.71

The mm-wave data is complemented by data collected from two micrometeorological (MET) stations. Each station contains an ensemble of instrumentation designed to determine the microstructure of turbulence in the surface boundary.

The NOAA micrometeorological data are obtained at two towers, 3.6 m in height, located adjacent to the propagation path at approximately one-third and two-thirds of the distance from the mm-wave receiver to the transmitter. These are designated as stations 1 and 2 respectively, as shown on Fig. 4. The instrument arrangement on each tower is shown in Fig. 5. The two optical paths were located 50 m and 65 m east of the mm-wave path. The micrometeorological towers were 80 m east of the mm-wave path, and the optical rain gauge/disdrometer paths were 90 m east. Each tower has a three-axis sonic anemometer with a platinum resistance-wire thermometer in the center of the sonic array, a nearby Lyman- α hygrometer with another wire thermometer within its gap, a prop-vane anemometer, and a psychrometer for mean temperature and humidity. The wire thermometers and Lyman-hydrometer were sampled at 100 Hz. The sonic

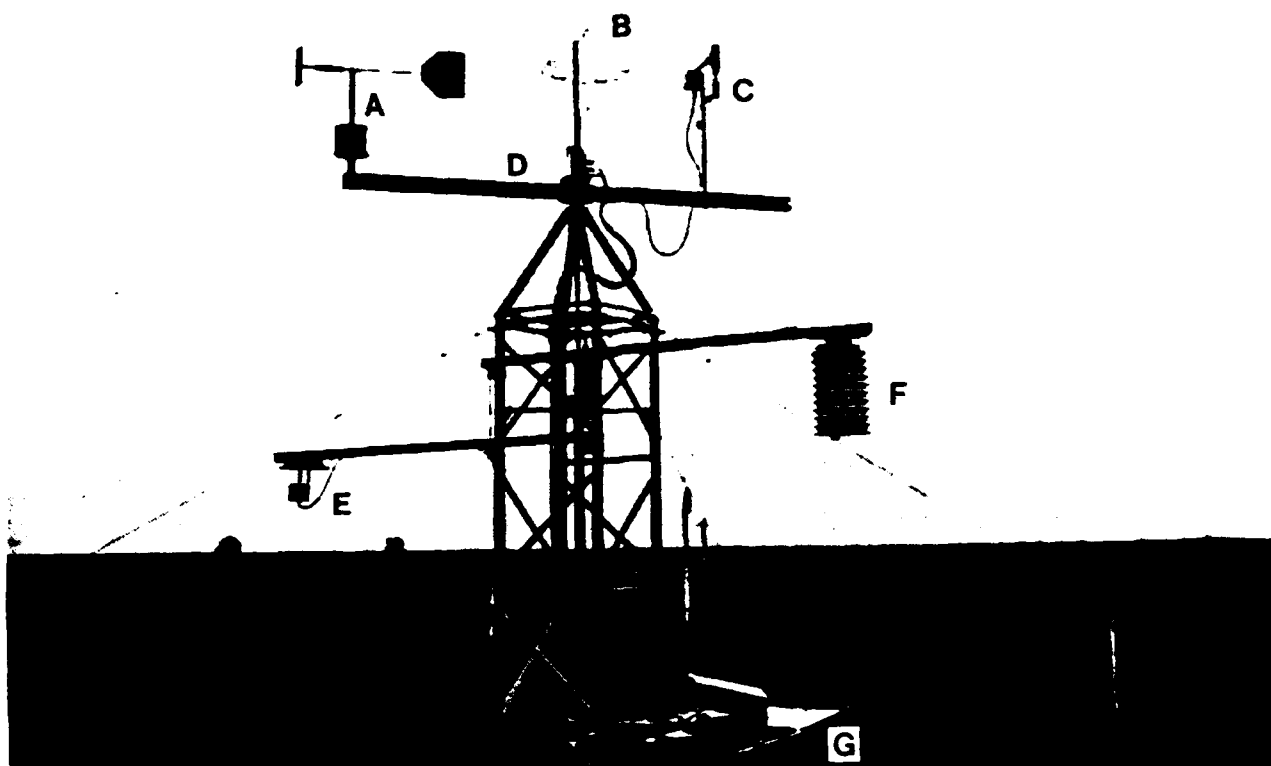


Figure 5. MET tower micrometeorological instrumentation at each station. The optical instruments associated with each station are shown schematically in Fig. 4. A = Propeller-vane anemometer; B = Three-axis sonic anemometer with wire temperature sensor in center; C = Lyman- α hygrometer with wire temperature sensor in center; D = Rotatable boom with angle encoder; E = Vaisala humidity probe; F = Aspirated psychrometer; and G = Electronics cabinet containing power conditioning and data telemetry systems.

and prop-vane anemometers were sampled at 25 Hz. Beginning with the 0.39-Hz pulse, the psychrometer gives six commutation cycles repeated at the 25-Hz rate. A commutation cycle consists of data from the wet and dry bulbs and two reference values, four quantities in all. The psychrometer then returns toward thermal equilibrium until the next 0.39-Hz pulse calls for data; this minimizes self-heating in the psychrometer due to power dissipation. Station 2 has a Vaisala mean temperature and humidity instrument sampled at 25 Hz, but the Vaisala readings of humidity are judged inferior to those of the psychrometer. Station 2 included an up-looking all sky pyranometer for solar radiation and cloud-shadow-occurrence measurements, and station 1 included a barometer; these were sampled at 25 Hz. A combined optical C_n^2 and optical cross-wind meter was

operated on the path from near the mm-wave transmitter to station 1 and another from near the mm-wave receiver to station 2; these optical paths overlap. Optical rain gauges were deployed near both stations and six weighing bucket rain gauges were deployed along the path. At station 1 the optical rain gauge included a disdrometer. The data from these optical instruments were sampled every 2.56 seconds. The reduction of the data from the rain instruments is discussed in Appendix III.

Additional optical instrumentation was deployed during the fourth experiment session. A 10.6- μm CO₂ laser, for measurement of infrared C_n^2 in clear air and for phase-difference spectra in rain, was operated from near the mm-wave transmitter to inside the mm-wave receiver trailer. A third large-aperture optical C_n^2 and cross-wind meter was operated over the northern two-thirds of the range directly below its existing counterpart. The purpose was to measure vertical shear averaged along the 50 m path. A He-Ne laser scintillometer and LED scintillometer were deployed over the same short path to measure the inner scale of turbulence by its effect on optical scintillation. At station 1, an up-looking photocell was installed to compare cloud cover measurements with those of the pyranometer at station 2. In addition, another psychrometer was installed at station 2 to determine the instrument's reliability by comparison with its existing counterpart. Except for the CO₂ laser, these additional instruments were recording data during the second half of the fifth session as well.

The heights of the instrumentation as well as subjective estimates of the 3σ errors in the heights are as follows: The mm-wave beam and CO₂-laser beam average $3.68 \text{ m} \pm 0.01 \text{ m}$; the Lyman- α gap, horizontal sonic transducers, prop-vane, and platinum wires are at $3.61 \text{ m} \pm 0.05 \text{ m}$; the psychrometer inlets are at $1.91 \text{ m} \pm 0.05 \text{ m}$; the upper-level optical wind and C_n^2 meters and the optical inner-scale meter are at $3.78 \text{ m} \pm 0.1 \text{ m}$; and the lower-level optical wind and C_n^2 meter are $2 \text{ m} \pm 0.02 \text{ m}$ below the upper-level meters.

II.3 Data Quantities

All data entered are accumulated over experiment times when statistics are stationary. Specifically, over times of constant variance in most, or all quantities. Consequently, a given data tape may contain several stationary intervals. In such a case, a given data tape may be used to enter several records in the data base. One may imagine a frontal passage during a run where the humidity changes drastically. Figure 6 depicts this event, and shows the two resultant stationary intervals which would be entered. Because this study is based upon stationary statistics, transient data are not entered in the data base. This data is, however, available to interested investigators via our archival system. All data described in this section, and named in Appendix A (this section) are entered as a single record, one for each stationary interval.

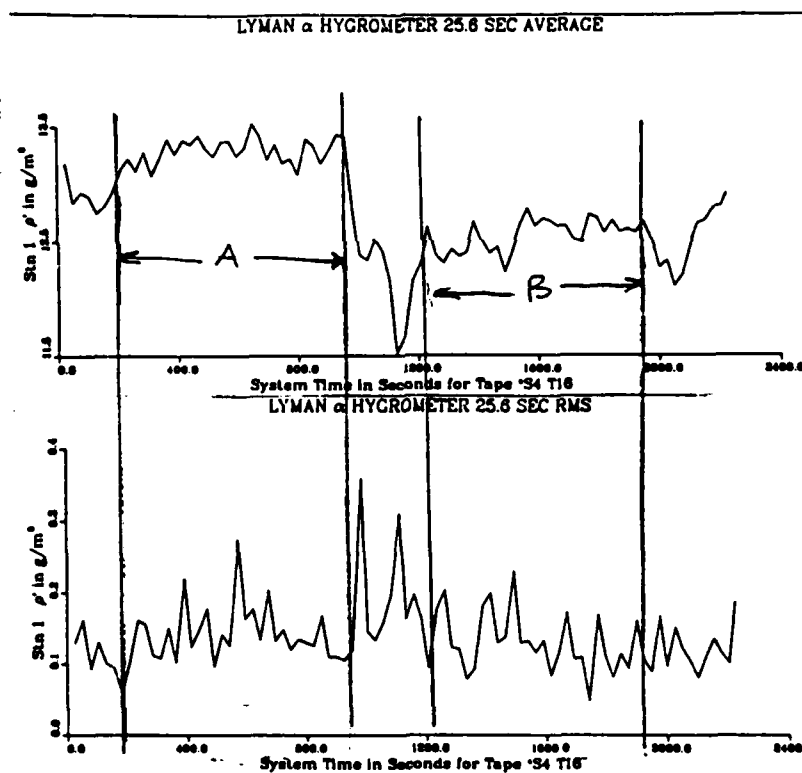


Figure 6. Example experiment with two stationary intervals.

All statistical quantities are built up from sets of local time averages. The interim files MILSUMS and METSUMS 21 (Fig. 7) contain sums, and sums-of-squares of quantities over 25.6 second intervals over the whole data

tape. They also contain sums of parameters for the MIL- and MET- statistics as described here. When these sums files are reviewed for statistical stationarity, the intervals are selected, and the sums are used in MILRDR and METRDR to accumulate and normalize statistics. All probability distributions are included in this process. Both the MIL and MET data used have been repaired [Ref. (23) and (24)], and data which cannot be repaired is excluded from the sums files so as to not contaminate the statistics.

The resultant statistics are incoherent moments about the mean for simple variables, and normalized probability distributions tallied over the interval of stationarity. The interval of stationarity will also be referred to as "the interval."

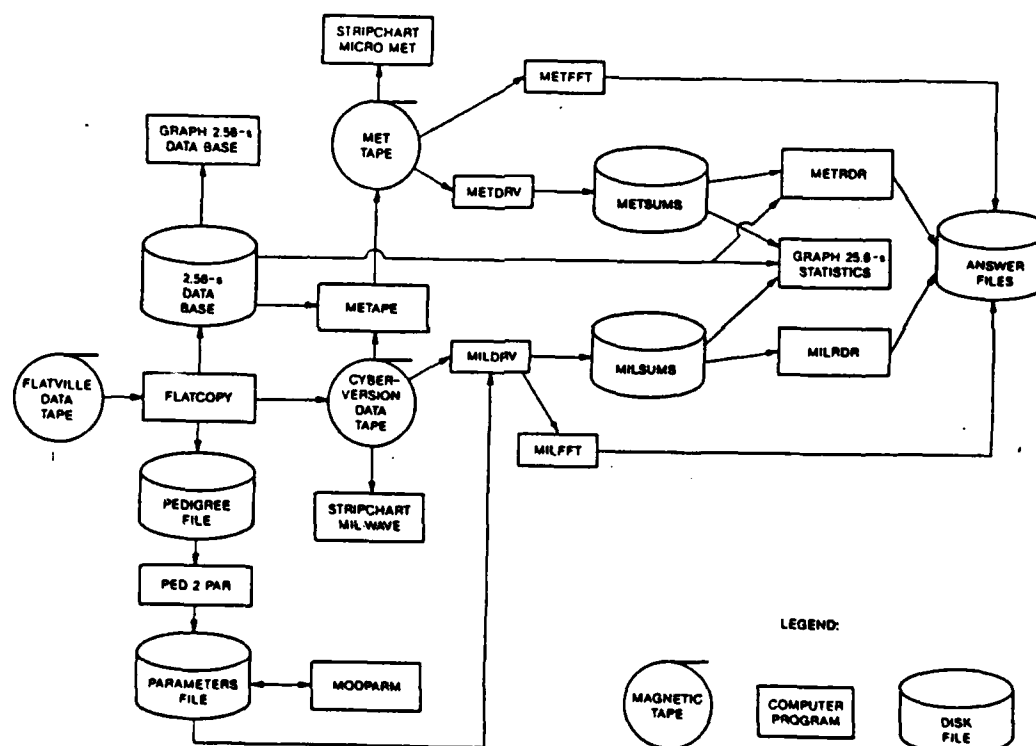


Figure 7. Overview of the data processing software..

Fourier analysis of both data sets is also entered, but the processing is necessarily quite different. High frequency (hf) spectra are produced by collecting as many 4096-point blocks of contiguous data as can be within the predefined stationary interval. When data are of good quality, and the interval of stationarity spans more than 81920 data, the FFT program divides the interval into 20 non-overlapping, evenly spaced regions from which twenty-4096 point spectra are taken. This rule is invoked over any subrange of data when break-point pairs are included in the interval. Any number of 4096 point contiguous time series, up to 20, may be established over the interval of stationarity, individually transformed and averaged together to produce the hf power and cross spectra. The spectra are then combined into 36 bins for MET data, or 72 bins for MIL data over approximately logarithmically spaced frequency bins. In each case, the first bin represents the DC component of spectra.

Low frequency (lf) spectra are produced by block averaging the data into longer averaging time bins and transforming these bins. The length of the bins depend upon the length of the interval, but have an upper limit of 0.6 sec per bin if the whole tape is used. Gaps in the lf data bins due to break points, frame-or-block loss are filled using a 4-point LaGrangian interpolation. This ensures a contiguous lf time series for Spectral Analysis.

There is only one lf transform over the entire interval of stationarity. All lf spectra have poor statistical significance until some intermediate frequency is reached. This manifests itself as noisy spectra in the low frequency region of the lf spectra. Figure 8 shows this concept for a MET coherence spectra where it is most evident. Because of this bin-only averaging, there is a frequency below which all coherence-spectral components are identically 1. This is designated f_1 in Fig. 8.

The list of cross spectra for all pairs processed are as follows:

Co-spectra: Given two quantities x_1 and x_2 , whose spectral transforms are r_1 and r_2 having the spectral components at some discrete frequency are shown in Fig. 9. (The r 's represent vectors in the complex plane.)

Met Station 1 25Hz Data FFT
 Lyman- α Hygrometer ρ *Lyman- α Wire T
 Coherence Spectra For Tape *S4 T16

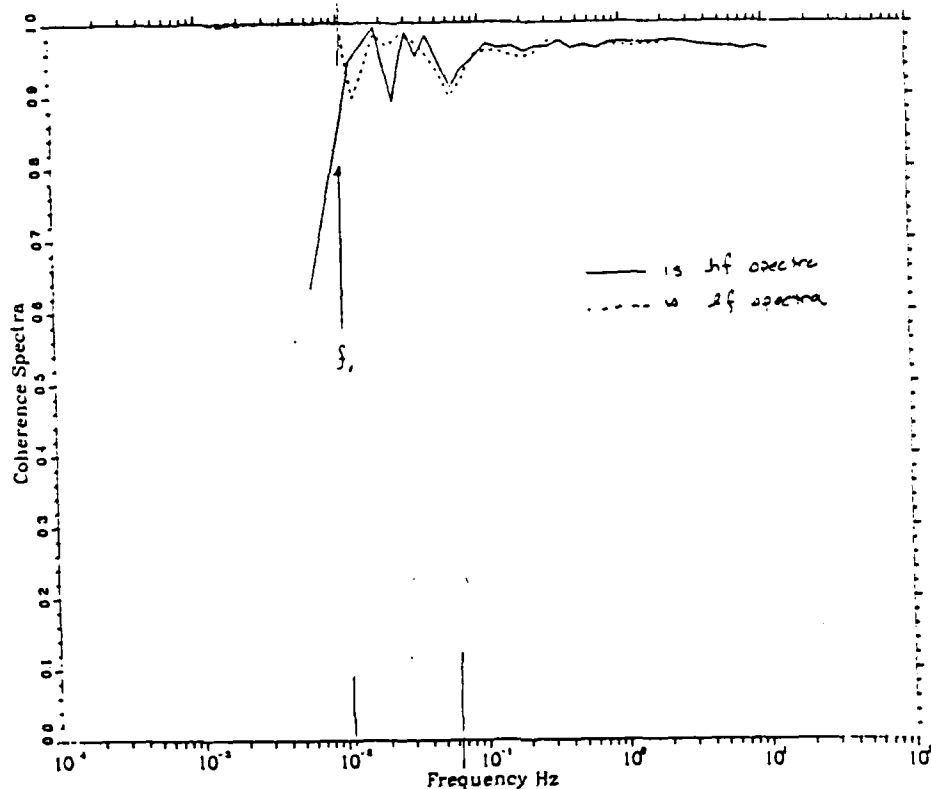


Figure 8. Temperature-humidity coherence spectra. The poor statistics at low frequencies is evident below f_1 .

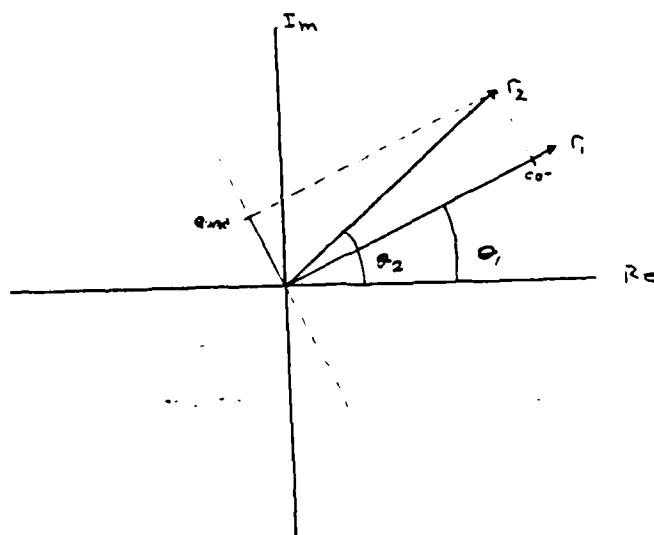


Figure 9. Phase relationship between two transformed quantities at a spectral component.

We define the co-component as the projection of r_2 on r_1 at this frequency. The co-spectra is then the spectrum of all the $r_1 r_2 \cos(\theta_2 - \theta_1)$ quantities. It represents the fraction of energy in r_2 which is in phase with r_1 .

Quad-spectra: The quadrature component is defined as the projection of r_2 on a line perpendicular to r_1 . It represents the energy in r_2 which is 90° out of phase with r_1 , and makes no contribution to the energy density of r_1 . The quadrature spectra is the spectrum of all the $i r_1 r_2 \sin(\theta_2 - \theta_1)$ quantities, where $i = \sqrt{-1}$.

The CYBER tape is used as input for the MILFFT processing. Although the incoherent averages have been filtered, the data used in the FFT's are not. Trends in the data due to parametric drift in the amplifiers, mixers, etc., contaminate the lf spectra, and the lf region of the hf spectra.

The MET-tape is used as input to the METFFT's. Because the MET data problems are dealt with at METAPE generation, filters are not necessary, and the METFFT's are generally quite good.

The quantities calculated from the millimeter-wave data and the equations used for the computations are described in detail in Ref. 21. Here we list the calculated quantity. We calculate the phase difference variance and intensity covariance for each of the six antenna pairs as well as the intensity variance for each of the four antennas. We calculate the largest and smallest observed phase difference for each antenna pair and intensity for each antenna. The probability density functions are calculated for each of the six phase differences and four intensities. The cross correlation between intensity and phase difference is calculated. The second and fourth moments of the electromagnetic field are determined. We calculate the power spectra and cross spectra of the intensities and phase differences. Quantities known as figures of merit are obtained.

The micrometeorological (hereafter called MET) instrumentation is designed to collect data which will provide statistics on clear air turbulence. From this data we calculate structure functions of temperature, humidity and refractive index. Also calculated are Fourier spectra and cross-spectra from data taken at 25 and 100 Hz sample rates. In support of this, we calculate averages, variances, and cross-correlation statistics. All MET data are in mgs units.

During clear air runs for which the MET stations were fully operating, we calculate average and rms values of air temperature $\langle T \rangle$, humidity $\langle q \rangle$, solar irradiance $\langle S \rangle$, wind speeds $\langle V \rangle$, wind velocity components $\langle u \rangle$, $\langle v \rangle$, $\langle w \rangle$, and wind direction $\langle \theta \rangle$. Variances are centered about the mean. Static pressure averages $\langle P \rangle$ in millibars are entered without variances. We have several ways of measuring temperature and humidity. All such determined values are entered in the data base except the Vaisala probe because of its poor performance.

Cross correlations between wind components, temperature fluctuation and humidity, temperature and vertical wind (temperature flux, and humidity flux respectively) are calculated about the mean. An instrument offset is subtracted from the mean to correct for misalignment of the sonic anemometers. When the mean wind directions in the MET-tower coordinates (boom normal) are determined, wind averages are rotated into the streamwise components. Horizontal and vertical momentum fluxes are calculated for both down- and cross-stream components. In addition, we calculate these fluxes assuming a horizontally homogeneous surface layer. The equations used for calculating the quantities are given in Ref. 21 (Appendix IV), as is the definitions of geographic and instrumentation-boom wind angles as well as the convention for the optical scintillometer wind readings.

We choose a rotation so that u_0 becomes the downstream component of wind, and v_0 becomes the cross-stream components. Selection of the angle through which wind related data is rotated depends upon the performance of the wind instruments. This angle (θ) may be the average vane angle, or the angle $\tan^{-1}(\langle v \rangle / \langle w \rangle)$ from the sonics. The latter is the conventional method but we prefer the former for most runs because the sonics offsets are not well known. In addition, we may select θ assuming a horizontally homogeneous boundary layer; $\theta = \tan^{-1}(\langle vw \rangle / \langle uw \rangle)$, or by some externally derived method, $\theta = \text{input}$. A flag is entered in the data base which specifies how θ was determined for each station. For each station, the wind selection code, THETSELECT values mean:

<u>THETSELECT</u>	<u>selection</u>
1	average vane angle
2	average sonics angle
3	horizontally homogeneous wind layer
4	externally derived value

II.4. Simple Macroscopic variables

The angle encoders at each MET-tower give the geographic direction in which boom is facing.

Simple variables that use sonics data are entered in the data base in both the boom-normal and stream-normal coordinates. For each station, data include:

average wind components	$\langle u \rangle, \langle v \rangle, \langle w \rangle; \langle u_\theta \rangle, \langle v_\theta \rangle$
variance of wind components	$u', v', w'; u'_\theta, v'_\theta$
wind stresses	$\langle uw \rangle, \langle vw \rangle; \langle u_\theta w \rangle, \langle v_\theta w \rangle$
cross products	$\langle uv \rangle; \langle u_\theta v_\theta \rangle$
momentum flux	$\langle u'v' \rangle; \langle u'_\theta v'_\theta \rangle$

The simple variables which are directionally independent include humidity corrected dry air density, buoyancy flux, radio frequency refractive index, dry bulb air temperature, wet bulb temperature, structure parameters of optical refractive index C_n^2 , optical, C_T^2 derived from optical C_n^2 , the boom's geographic orientation, atmospheric barometric pressure, integrated all-sky solar irradiance, absolute humidity calculated from both Lyman- α averages and the psychrometer data, the horizontal wind speed ($\langle V \rangle$), and wind direction (θ). Directionally independent cross correlations of simple variables include:

humidity flux	$\langle qw \rangle$
temperature flux	$\langle Tw \rangle$
latent heat content	$\langle qT_L \rangle, \langle qT_S \rangle$
fine-wire cross correlation	$\langle T_L T_S \rangle$
horizontal wind stress	$\langle w \sqrt{u^2 + v^2} \rangle$
dry air buoyant stability	Z/L
moist air buoyant stability	Z/L_v

II.5. Turbulence data

The quantity L above is the Monin-Obukov stability length and is based upon the downstream wind stress u_*^3 , known as friction velocity

$$L = \frac{u_*^3 T}{g \kappa \langle T_s' w \rangle} \quad (\text{II.5.1})$$

where $g = 9.8 \text{ m s}^{-2}$, κ = Von Karman constant, T is temperature in K, and only the sonics temperature fluctuations, T_s' are used, we use $\kappa \approx .4$. We also stored in the file for each MET station the friction velocity

$$u_* = \langle u_{\theta} w \rangle^{1/2}, \quad (\text{II.5.2})$$

and heat flux of moist air

$$Q_v = \langle T_s' w \rangle + 0.61 \frac{\langle Q_l w \rangle}{\rho} \left(\frac{\langle T_s w \rangle}{\langle T_l w \rangle} \right). \quad (\text{II.5.3})$$

Q_v is used in place of the temperature flux in (II.5.1) to calculate the moist air buoyant stability parameter, z/L_v . In each case, the buoyancy parameter is also calculated and stored assuming a horizontally homogeneous surface layer using temperature flux calculations as though THETSELECT = 3.

In clear air, the dry bulb and wet bulb temperatures at each station, $n = 1, 2$, (TD_n , TW_n) are determined from the psychrometer data. Temperature variances are taken from the fine wires. The humidity fluctuation is from the calibrated Lyman- α data. The psychrometer is used to calibrate the Lyman- α , this is high quality humidity data, and all run calibrations are scrutinized before an entry is made. The humidity in gm^{-3} is stored from both the Lyman- α and psychrometer.

The density of the air is calculated using the measured pressure and temperature in the ideal gas law. We apply a moisture correction term using average humidity from the psychrometer as follows:

$$\rho_{\text{air}} = \frac{P}{R_{\text{air}} T_{\text{abs}}} - 0.61 \rho_{\text{H}_2\text{O}} \text{ gm}^{-3}. \quad (\text{II.5.4})$$

II.6. Structure parameters

The details of the calculation of the following structure parameters is given in Appendix IV. The space-lagged structure parameter obtained from the temperature difference between the platinum wire thermometers in the sonic anemometer and Lyman- α hygrometer is obtained. Under an assumption of isotropic turbulence the space-lagged temperature-humidity cross-structure parameter is also obtained. Time-lagged temperature and humidity structure parameters as well as the temperature-humidity cross-structure parameter are calculated using three different time lags all of which are in the inertial subrange. The radio refractive-index structure parameter is calculated from the above MET structure parameters using sensitivity coefficients A_T and A_Q obtained from the radio refractive-index equation.

These data are stored in the array TIMELAGS which is dimensioned. The first index, $n = 1,3$ refer to the three time lags described above. The second position index has the following meaning:

<u>i</u>	<u>time lagged parameter</u>
1	C_q^2 from Lyman- α humidity
2	C_T^2 from Lyman- α wire
3	C_T^2 from sonic wire
4	C_{Tq} from Lyman- α humidity and its wire

The actual time lags are not interesting and are not stored.

Of the path averaged optical data described in section II.1, only the optical cross wind and refractive index structure parameter, C_n^2 , is averaged over the interval and entered in the data base, we also calculate \dot{C}_T^2 from the optical C_n^2 using

$$C_T^2 = \frac{C_n^2}{(79 \times 10^{-6} P/T^2)^2} \quad (\text{II.6.1})$$

Probability distribution functions (PDF's) are calculated for the pyranometer solar flux (w m^{-2}) and wind angles at each station (deg-arc) from the

vaness. Each PDF is a 50 element array. The central 48 elements is the normalized PDF, and the 1st and 50th are catch bins for values outside the PDF limits. One must also retrieve the PDF limits from the file so the data have meaning.

The MET station PDF's are stored as arrays of real numbers which represent the probability that a value x lies in the range $(x, x + \Delta x)$. The increment Δx is calculated from the retrieved limits using

$$\Delta x = \frac{x_{\max} - x_{\min}}{48} .$$

The useful bins are for $i = 2$ to 48 inclusively; thus the i^{th} bin represents the probability that a value x lies in the range

$$[(x_{\min} + (i-2) * \Delta x), (x_{\min} + (i-1) * \Delta x)] .$$

Joint PDF (JPDF) of Lyman- α humidity and its fine wire temperature fluctuation is also calculated for each station. The structure of the JPDF is the two-dimensional analog of the PDF. The catch bins become a square perimeter around the 48×48 cell JPDF whose limits are also stored on file. The joint probability that the temperature lies in the i^{th} bin of its range and the humidity lies within the j th bin of its range is stored in the (i,j) element of the JPDF array.

For all PDF's, the cell widths are determined by reading the limits and dividing the spread by 48.

$$\text{i.e., } \Delta T' = (T'_{\max} - T'_{\min})/48$$

II.7. Fourier spectra of MET data

We calculate the power spectra of the fluctuating temperature and humidity from the resistance-wires and the Lyman- α hygrometer, as well as the temperature-humidity cospectra and quadrature spectra from these instruments. We also calculate the power spectra of all three orthogonalized components of the fluctuating wind from the sonic anemometers, as well as the cospectra and quadrature spectra of these components taken in pairs. The cospectra and quadrature spectra are calculated for temperature and vertical velocity, and

for humidity and vertical velocity.

FFT's are combined to produce sets of cross spectra between pairs of quantities. The cross spectra produced include cospectra, quadrature spectra, coherence, phase spectra, normalized co- and quadrature-spectra. Power, and cross spectra on the interval of stationarity come in two parts. The high frequency (hf) spectra are transformed from a 4096-point time series. This corresponds to 40.96 sec of data if only 100-Hz quantities are involved or 163.84 sec of data if at least one quantity is of the 25-Hz sampling rate. When data are of mixed sample rate, the higher data rate is block averaged into a time series at the lower data rate is averaged into a time series at the lower rate. The FFT's are then combined into 36 bins and entered in the file.

In addition to the cross spectra described in section II.3 the MET spectra includes:

Normalized co-, and normalized quad-spectra: The co- and quadrature-spectra described in II.3 are normalized and stored.

Phase spectra: We also calculate the spectrum of phase angles between the Fourier components (see Fig. 9):

$$(\theta_2 - \theta_1)$$

Coherence spectra: We define the coherence spectra as the spectra of $\langle r_1 r_2 \rangle / \langle r_1 \rangle \langle r_2 \rangle$, described in Fig. 9, where averages are taken over contributions in each of the log-averaged bins and the r's represent vectors in the complex plane. It offers a measure of how well frequency bins were chosen, and how well the bin average spectra mimics the full transform. The low frequency components of coherence are reduced to the trivial identity, 1, because only one component of the original transform of $x_1 x_2$ contributed to those 1f bins.

For each MET station, $n = 1, 2$, both 25 MHz and 100 MHz spectra are calculated. The pairs of MET quantities use in cross spectra are:

r_1		r_2	
at 100 MHz,			
Lyman- α hygrometer	*	Lyman- α Fine Wire	$q_n T'_L$,
at 25 MHz,			
Lyman- α	*	Sonics w	$q_n w_n$
Sonics wire	*	Sonics w	$T'_s w_n$
Sonics u	*	Sonics v	$u_n v_n$
Sonics u	*	Sonics w	$u_n w_n$
Sonics v	*	Sonics w	$v_n w_n$

Because the fourier transform produces a complete set of basis vectors, we leave rotations and other orthogonal transforms on the FFT's to the user.

During inclement weather experiments, the fine wires and Lyman- α hygrometers are covered. Rain drops in the volume sampled by Sonic anemometers cause spurious signals not related to wind speeds to contribute to measurement errors there. Furthermore, in session V, ice buildup was observed at the inlet of the psychrometer at station 2 which may have changed its psychrometric constant used in data reduction, and on several runs, the Prop-vane had froze producing no data at all. These tapes were not used to make entries in the data base, but it alerts us to problems with the data that rain and snow can cause. We advise users to be cautious when using MET quantities for other than clear-air data.

We do not make the METAPE for inclement weather. All MET data is derived from the 2.56s data base for these tapes. The primary purpose of inclement weather MET data entries is to support the interesting mm-wave data.

For MET station n , $n = 1, 2$, the horizontal components of wind are derived from the prop-vane using $\langle u_n \rangle = \langle V \cos \theta \rangle$ and $\langle v_n \rangle = \langle V \sin \theta \rangle$ where V is the prop speed, and θ is the vane angle returned from the 2.56s MET data base. We set $\langle w_n \rangle = 0$.

For completeness, we rotate the wind components as described in section 11.3. Clearly only an externally derived value for $\langle \theta \rangle$, or the average vane angles can be used to select the rotation angles.

We include for comparative purposes the average cross-path wind speed measured by the optical cross wind instruments. The two instruments look

towards each other so they must have opposite signs if there is agreement.

We suggest that the user resolve the prop-vane data into cross-path wind components and compare the answers to the optical data. This will yield a measure of data reliability. We have observed the following:

- a. In heavy rain, dense fog, or snow, the optical cross wind data can get contaminated from scintillation due to scattering by the particles; or attenuated due to absorption. In this case the prop-vanes are probably more reliable.
- b. In case of extreme cold and high humidity, the prop-vane may have accumulated ice causing errors in both wind speed and direction. If the precipitation is not too heavy, the optical data is probably better, but only one component of wind is known; and not well at that.
- c. In all cases of wind below about 2 m s^{-1} , the vane angle is usually wrong due to the long lag in response to directional changes. When the wind calms to below 1 m s^{-1} the prop becomes suspect. (In clear-air data we rely on the sonics).

The psychrometer is used to determine the humidity, dry bulb temperature and wet bulb temperature. This data is written on the file where Lyman- α hygrometer data would normally be. Temperature variances are based upon the dry bulb temperature from the psychrometer. Atmospheric pressure is derived from barometer as usual. The moisture-corrected air density is also calculated and entered using water vapor density from the psychrometer and the ideal gas law. A point of caution regarding the pyranometer data: Rain and snow tend to cool this detector so that the reported solar irradiance is generally low.

Perhaps the most interesting data to correlate with the mm-wave intensity fluctuations is rain rate and drop size distribution. Because of the special characteristics of the optical rain gauges, and need for per-event calibration. The optical rain gauge output is in volts-dc, and disdrometer average counts are stored unnormalized. A separate publication²⁵ is being prepared which will unravel the mystery of the optical rain gage as we produce calibration data for the several runs of interest.

The disdrometer data is somewhat simpler to reduce, but determination of drop size distribution is left to the user because of several models in the literature. The data in the array DROPSIZES are 129 integers representing the correlation for slit crossing times. The first 65 cells represents a correlation time from 0.0 to +0.64 s by 0.01 seconds, and the next 64 cells represent correlation times from -0.64 s to -0.01 s by 0.01 seconds. The number in each cell, N_c , is related to the correlation of the average rain drop passing between slits with a correlation time τ_c defined above. The normalized correlation coefficient(s) directly from the correlator is given by

$$r_{\tau} = \sin\left(\frac{\pi}{2} \frac{N_c}{8192}\right) \quad (\text{II.7.1})$$

The slit crossing times are related to rain drop vertical velocity, and therefore size; but just how depends upon the user's choice of a model of a droplet falling at terminal velocity, i.e., is it spherical, or does it have a flattened bottom? We present the correlation function only. Use of this data is user's discretion. Users of this data are encouraged to review articles referenced in Appendix III. Figure 10 depicts the data stored in the array DROPSIZES after folding the correlation time scale and normalizing using (II.7.1).

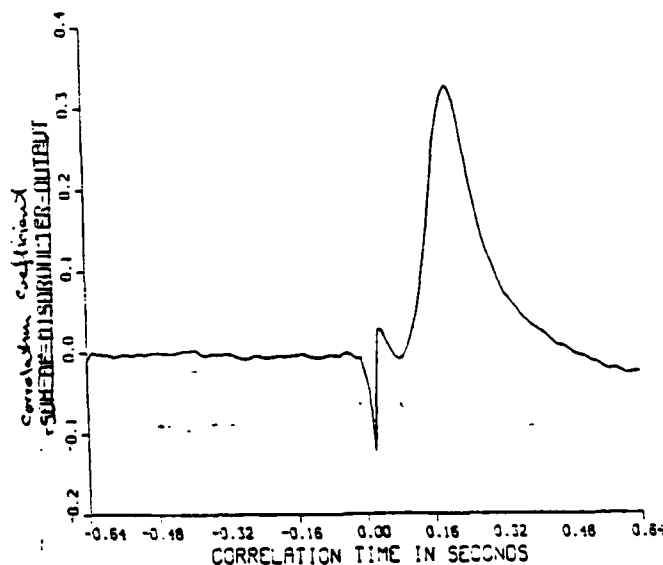


Figure 10. Disdrometer output folded back and normalized using Eq. II-7.1.

II.8. Accessing the Data

There is complete freedom for the user to build the subroutines into a program which uses the retrieved data, or to retrieve data and transfer it to a smaller local file for later investigation. The latter is the simplest use of the file, and the steps are:

1. Establish the rule by which data is to be retrieved.
2. Define which data to retrieve.
3. Get the data.

We refer to the data base interrogation software from here on as "the system."

II8.1 Establishing the keys of the records: making the rules

A rule by which records are read, (or ignored), is established by setting keys in seven categories. Table VI shows the categories and the maximum number of possible values that can be set in each category. Each category is an integer variable, or array of size up to the limit shown. Records may be collected in any combination of categories, and any combination of categorical values. An example follows where two weather conditions are selected.

One must also tell the system how many keys are set in each category. If the user specifies zero keys selected, the system does not use that category to select records (in other words, it will return records having all values of keys in that category) a bug, therefore, is inherent in the system. If a user selects 1 range of values in a category, and sets the key value of that category to zero, the system will look for records which have a zero value in that category. Except for the stationary interval category described above, no records will be found. Section II.9 describes a quick and easy way of getting data where we have dealt with this bug in the system.

Table VI. Record Key Categories

Key	Max length	Explanation
Weather	8	Weather condition during experiment
C _n ² -radio	8	A range of radio frequency refractive index structure parameters
Frequency	8	A range of mm-wave transmitter frequencies
Z/L	8	A range of bouyant stability values in the surface layer
Session	8	One of five experimental sessions
Tape	100	One of hundred of experiment data tapes taken in the 5 sessions
ISTA	8	One of several stationary intervals possible on each tape

II.8.2 Weather condition

The weather categories for the weather key values are in Table VII. If a person wished to collect data for all kinds of snow data only, he would select weather codes to be 4 and 5. An example of code follows:

```

      .
      .
      .
      INTEGER    WX(2)
      .
      .
      DATA    WX/4,5/, NWX/2/

```

the variable NWX tells the system that two weather keys are selected and to retrieve data from both keys specified in the array WX. To collect data in all weather conditions regardless of the values in WX, the user will set NWX = 0.

Table VII. Weather Condition Codes

Key Value	Weather Condition
1	Clear Air
2	Fog & Rain
3	Rain
4	Snow
5	Blowing Snow

II.8.3 Radio frequency refractive index structure keys

Table VIII shows the range of rf refractive index structure parameters selected by it's key. If a user wants to collect data for all C_n^2 -rad > 3.16×10^{-11} they would code the following:

```

.
.
.
INTEGER  CNZRAD (3)
DATA  CNZRAD/1,2,3/, NCNZR/3/
.
.
.

```

The system will return all records for which the radio frequency refractive index structure parameter is greater than 3.16×10^{-11} .

Table VIII. C_n^2 -rad Nominal Range Key

Key Value	Range of C_n^2 -rad
1	C_n^2 -rad $> 3.16 \times 10^{-10}$
2	$3.16 \times 10^{-11} < C_n^2$ -rad $< 3.16 \times 10^{-10}$
3	$3.16 \times 10^{-12} < C_n^2$ -rad $< 3.16 \times 10^{-11}$
4	$3.16 \times 10^{-13} < C_n^2$ -rad $< 3.16 \times 10^{-12}$
5	$3.16 \times 10^{-14} < C_n^2$ -rad $< 3.16 \times 10^{-13}$
6	$3.16 \times 10^{-15} < C_n^2$ -rad $< 3.16 \times 10^{-14}$
7	C_n^2 -rad $< 3.16 \times 10^{-14}$

To select all values of C_n^2 -rad, he would set NCNZR = 0. The ranges and values returned are clarified in Appendix B.

II.8.4 mm-wave transmitter frequency range keys

Table IX gives the mm-wave frequency range, f , in GHz for the key values in the frequency category. All frequency ranges will be selected when the user requests no categories similar to setting NCNZR = 0 above.

Table IX. mm-Wave Frequency Range Keys

Key Value	mm-Wave frequency range, GHz	Propagated mm-wave frequencies at Flatville
1	$f < 122$	116.30, 118.75 120.75
2	$122 < f < 157$	142.00
3	$157 < f < 200$	172.91, 173.00, 172.62
4	$f > 200$	229.25, 230.44

II.8.5 Buoyant stability condition, Z/L , keys

The parameter, Z/L , is the ratio of the height above ground of the measurement (3.68m) to the Monin-Oboukhov scale length, L . When the surface layer is unstable ($Z/L < 0$), the turbulence is driven mainly by buoyant plumes rising, these plumes are driven by upward heat flux from the surface. This condition prevails in sunny (afternoon) weather. The ranges of this stability parameter are given in Table X. As in the previous key, if no ranges are selected, all Z/L key values will be returned.

Table X. Z/L Range Key

Key Value	Stability Parameter Range	Condition
1	$Z/L < -0.5$	unstable
2	$-0.5 < Z/L < -0.1$	
3	$-0.1 < Z/L < 0.1$	near neutral
4	$0.1 < Z/L < 0.5$	stable
5	$Z/L > 0.5$	

II.8.6 Session, tape, and interval keys

Because occasionally an investigator may wish to access data from a particular experiment, we include these categories. Not all tapes are processed through to the data base because of a variety of problems not unusual to an experiment of this scope. As described earlier, one will generally specify that the number of session id's, the number of tape id's, and the number of stationary interval id's are each zero so the system will not use this unscientific data as selection criteria i.e., set NSES = NTPE = NSTA = 0 below.

For investigators who are interested in one or more particular runs, the range of session data and tape values are given in Table XI. For all sessions and all tapes, the valid values of the interval keys are 0-9 representing stationary intervals A-J respectively. For example, if one wished to review the data shown in Fig. 6, they would code

```
INTEGER SES, WSES, TPE, WTPE, ISTA(2), NSTA
DATA SES/4/, NSES/1/, TPE/16/, NTPE/1/, ISTA/0,1/, NSTA/2/
```

This would tell the system that one session, one tape and 2 intervals are to be returned: namely intervals A and B from session 4's tape 16.

Table XI. Session-Tape Key Values: An Experiment Overview

Session Key value	Valid Tape Key values	Session Data	Season
1	8,9,14,15,22-25,27	15 July '83 - 20 July '83	Summer
2	2-45	12 Nov '83 - 6 Dec '83	Fall
3	1-93	11 Feb '84 - 6 Mar '84	Winter
4	3-75	8 Jun '84 - 3 July '84	Summer
5	1-77	8 Feb '85 - 18 Mar '85	Winter

II.8.7 Data names

There are 538 named data items in the Dictionary. Each name has up to ten characters (1 CYBER word). The list of names, and their meaning is detailed in Appendix A.

II.8.8 Accessing the data; method I: The easy way

We provide a single specific subroutine which will act independently to open the data base, get requested data by name according to your rule as described in section II.8.1, transfer the data to a smaller local file, then close the data base. We require that each of the specification categories be imensioned to their maximum size shown in Table VI, and an array of variable names be declared large enough to hold all the data names requested. When all elements of a category are zero, the system will not use this category in selection.

The Format:

```
CALL READATA (LUNAE, LUNOUT, ITYPE, WX, SES, ZOVRL, F, TAPE,
              CNZRF, ISRA, VARRAY, NITEMS, NUMID)
```

The inputs to READATA are:

LUNAF = The DATA BASE logical unit specifier as declared in a program card.

LUNOUT = The logical unit specifier for the output file created by this subroutine.

- ITYPE = The type of data file to create as follows:
- 1 = Sequential unformatted (Binary)
 - 2 = Sequential formatted-list directed
 - 3 = Random access unformatted
- WX = 8 element integer array containing the weather categories of interest, or all zeros, ref. section II.8.2.
- SES = 8 element integer array containing the session numbers of interest, or all zeros, ref. section II.8.6.
- ZOVRL = 8 element integer array containing the stability keys of interest, or all zeros, ref. section II.8.5.
- F = 8 element integer array containing all mm-wave frequency categories, or all zeroes, ref. section II.8.4.
- TAPE = 100 element integer array containing all tape numbers of interest, or all zeroes, ref. section II.8.6.
- CNZRF = 8 element integer array containing all rf C_n^2 of interest, or all zeroes, ref. section II.8.3.
- ISTA = 8 element integer array containing all stationary intervals of interest, or all zeroes, ref. section II.8.6.
- VARRAY = An array of CHARACTER*10, NITEMS in length containing the names of data as described in the dictionary in Appendix A.
- NITEMS = The number of data items requested, and the length of VARRAY.

The output of READATA is:

- NUMID = The number of records found which meet the criteria specified in the category arrays; WX, SES, ZOVRL, F, TAPE, CNZRF, and ISTA.

If the user specified all zeroes in all category arrays, READATA will put the data lists into the output file for every record entered in the data base. This is the opposite of the bug described in section II.8.

The local file created by READATA on unit LUNOUT is called NEWFIL. Each record contains the requested data in VARRAY in the order of items in VARRAY. There are NUMID records in the file NEWFIL.

We provide an example of this usage in Appendix B.

II.9 Accessing the Data: Method II, the Programmer's Way

This section describes the intermediate level subroutines available to the user. READATA described in section II.8.8 uses these routines to create NEWFIL. The advantage to using this method is that an interim file is not needed, and the user may work with the data in memory. The disadvantage is that the data base will normally remain connected to the job and cannot be used by others until it is released. We encourage users of this method to make a local copy of the data base, then return the file before using its clone. Programs in Appendix C is an example of this method of data acquisition. We now describe the requirements for using this method.

II.9.1 Method II: required work space

All required work buffers used by the system and not by the user are allocated "behind-the scenes" for this particular data base. The user need only allocate space for his purposes as follows:

II.9.2 Category key buffers

Each category, described in section II.8, requires an integer space of length equivalent to the number of keys selected in that category. If no keys are selected, then a simple integer must be specified for that category anyway. The system must also be told how many keys are selected in each category. There are seven variables or arrays, plus seven key counters.

II.9.3 Record identifier array

An integer array of record identifiers which meet the selection criteria must be provided. The length of this buffer depends upon how many records satisfy the criteria. 256 is a good number, but if your program requires more, then increase it. The maximum size that will ever be needed is equal to the total number of records in the file. See below.

II.9.4 Record space

A real array must be allocated of sufficient length to read the requested data. We supply an integer function, IWSRTR, which returns the most efficient length of a record buffer to specify. Its arguments are the variable names list, and the number of items requested, i.e.,

ISIZE = IWSRTR(VARRAY,NITEMS).

II.9.5 Variable space

There are three arrays required to access the data. These array do not store the data. For the sake of discussion, suppose the user is accessing NITEMS from the data base by name.

II.9.6 Variable names list

A character * 10 array of length NITEMS must be allocated. This array is filed with valid data names. The names of data are given in the Dictionary in Appendix A.

II.9.7 Variable locations list

An integer array of length NITEMS must be allocated to store the address of the named variables. Subroutine GETVAR, described below will return the locations so the user need not do this.

II.9.8 Variable sizes list

An integer array of length NITEMS must be allocated to store the lengths of the variable named. Subroutine GETVAR will return these lengths.

II.9.9 Data space

A list of variables or array which store the named data must be allocated with sufficient space to store the data returned. The variable sizes are listed in the Dictionary in Appendix A. No error will result if the lengths are wrong. The user will merely get unpredictable results.

II.9.10 Subroutine calls

We now describe the subroutines used for acquiring data from the file by Method II. They are presented in the usual calling sequence.

II.9.11 OPENDB: Open the data base

The Format is:

CALL OPENDB (LUNAF)

where LUNAF is the logical unit number assigned by the user to the data base.

II.9.12 GETVAR: Check the names list

This program checks the named items in character * 10 array items (NITEM) to see if they are valid dictionary names. If they are, it returns their locations and sizes. If one item is not in the dictionary, the program stops.

The Format is:

CALL GETVAR (ITEMS, NITEMS, LOCATN, NSIZES)

Inputs:

ITEMS = Character * 10 array, Section II.9.6.

NITEMS = Number of items requested, Section II.9.5.

Outputs:

LOCATN = Integer array of locations, Section II.9.7.

NSIZES = Integer array of sizes, Section II.9.8.

There is a 1:1:1 correspondence in the element locations of the data names in ITEMS to their locations and sizes.

II.9.13 IDS: Return record identifiers which meet selection criteria

This subroutine assembles a list of data base records which meet the selection criteria rule(s) described in section II.8.

Format:

```
CALL IDS (IWX, NWX, ISESN, NSESN, ISTAB, NSTAB, IFREQ, NFREQ,  
1         ITAPES, NTAPES, ICN2RF, NCN2RF, ISTAT, NSTAT, IDARRAY,  
1         NUMIDS)
```

Inputs:

IWX = Integer array of weather keys, section II.8.2.

NWX = The number of weather keys selected. If zero, all weather conditions are selected.

ISESN = Integer list of sessions, section II.8.6.

NSESN = The number of session keys selected. If zero all sessions will be selected.

ISTAB = Integer array of Bouyant Stability keys, section II.8.5.

NSTAB = The number of Z/L keys selected. If zero, all stability conditions will be selected.

IFREQ = Integer array of mm-wave transmitter frequencies range keys, section II.8.4.

NFREQ = The number of frequency range keys selected. If zero, all frequency ranges will be selected.

ITAPES = Integer list of session tape numbers to select, section II.8.6.

NTAPES = The number of session tapes selected. If zero, all tapes will be selected.

ICN2RF = Integer array of radio-frequency refractive-index structure parameter range keys selected, section II.8.3.

NCN2RF = The number of C_{nrf}^2 keys selected. If zero, all ranges will be selected.

ISTAT = Integer list of stationary intervals to select, section II.8.6.

NSTAT = The number of stationary intervals selected. If zero, all intervals will be selected.

Outputs:

IDARRAY = An integer list of records which meet the combined selection criteria on input.

NUMID = The number of records entered in IDARRAY.

A potential pitfall is if the user sizes IDARRAY to be less than NUMID returned by IDS. If this occurs, adjust the size of IDARRAY to be greater than or equal to NUMID, and rerun your job.

II.9.14 READDB: Read a data base record

This routine reads a single record from the data base.

Format:

CALL READDB (LUNAF, RECORD, LENREC, ID)

Inputs:

LUNAF = Logical unit number assigned to the data base.

LENREC = Length of the record to read. This is usually the value returned from IWSRTR, section II.9.4.

ID = Record identifier to read. This will normally be an element of IDARRAY in section II.9.12.

Outputs:

RECORD = An array of length LENREC, and mixed type.

II.9.15 GETVAL: Retrieve data from the data record

This program gets the requested data from a data base record.

Format:

CALL GETVAL (RECORD, LENREC, LOCAL, ISIZE, VALUE)

Inputs:

RECORD = Real array of length LENREC returned from READDB.

LENREC = Length of record above. This is usually the value returned from IWSRTR, section II.9.4.

LOCAL = Location of the variable being returned. This is normally an element of the array LOCATN returned from GETVAR, section II.9.12.

ISIZE = Length of the named variable being returned. This is normally an element of the array NSIZES returned in GETVAR, section II.9.12.

Output:

VALUE = Real array of size ISIZE containing the returned data.

II.9.16 CLOSEDDB: Close the file and release the resource

This program closes the data base and disconnects it from the user's program.

Format:

CALL CLOSEDDB (LUNAF)

Input:

LUNAF = Logical unit number assigned to the file.

ACKNOWLEDGMENTS

We wish to thank J. P. Riley of WPL for his assistance and comments during the design of the data base. A special thank you goes to Veronica A. Stahl, who maintained a sense of organization as well as humor during data analysis and production.

This work was made possible by a grant from the U.S. Army, ARO, grant number MIPR 122-85.

APPENDIX A

THE DICTIONARY OF DATA

Table A-1 is a listing of the dictionary giving the variable names, position, type, and description. For brevity "A" means the average of a value over the interval. "S.D." is the standard deviation of a value over the interval, or square root of its variance.

NOTES ON THE LISTING

- Note 1: References to all intensity related arrays in the mm-wave data contain values of intensity from antennas 1 through 4 inclusively in that order. References to 6 element antenna pair data refer to pairs 1&2, 1&3, 1&4, 2&3, 2&4, and 3&4 for indexes = 1 to 6 respectively.
- Note 2: The real and imaginary parts of M_4 in II.3 element indexes 1-33 refer to $ijnm$ values for cases 1-33 given in Table 2 of Appendix IV (Ref. 21) respectively.
- Note 3: The first 6 elements of array FIGAR contain the type figures of merits for antenna pairs 1 through 6. The second 6 elements contain the corresponding variances.
- Note 4: The first 6 elements of the array FIGVAR contain the Σ -type figures of merit for antenna pairs 1-6, the second 6 elements contain their variances. The next 4 elements contain the phase-type figures of merit for antenna triples, and the last element contains the phase-type figure of merit from 4 antenna pairs. These figures of merit are explained in Appendix IV (Ref. 21).
- Note 5: Generic FFT entries. Each FFT is preceded by a processing header. The spectra are entered as low frequency spectra "LF....", then high frequency spectra "HF....". The first item is the frequency bin assignments, next are the power spectra, then the cross spectra.
- Note 6: MIL FFT cross spectra consist only of co- and quadrature spectra designation "...COSPC" and "....QDSPC". The "Cij" mean "cross spectra

between channel i and j" where Table A-1 defines the data in "channel i or j".

TABLE A-1.

i or j	channel data
1	antenna 1 intensity
2	antenna 2 intensity
3	antenna 3 intensity
4	antenna 4 intensity
5	phase difference pair 1&2
6	phase difference pair 1&3
7	phase difference pair 1&4
8	phase difference pair 2&3
9	phase difference pair 2&4
0	phase difference pair 3&4

Thus, LFC17QDSPC at position 3624 decodes fo low frequency quadrature spectra between antenna 1 and phase difference pair 1-4. This sequences repeats for MIL data high frequency spectra, "HF....".

Table A-2

Dictionary of ANSWERS File Data

VAR NAME	VAR POSITION	VAR TYPE	VAR SIZE	Meaning
***** MET Stations Statistics Block *****				
RUMID	1	INTEGER	1	Experiment Tape Identifier
Q1AV	2	REAL	1	Absolute Humidity in gm-3 from Met Station 1 Lyman-Alpha hygrometer
Q1RMS	3	REAL	1	Standard deviation of Q1 above
T11AV	4	REAL	1	Average Temperature fluctuations at Stn 1 Lyman-Alpha Wire Degrees K
T11RMS	5	REAL	1	Standard deviation of T11 above
T21AV	6	REAL	1	Average Temperature fluctuations at Stn 1 Sonics Wire. Deg K
T21RMS	7	REAL	1	Standard deviation of T12 above
HWS1AV	8	REAL	1	Average horizontal wind speed from Stn 1 sonics. $\sqrt{U12 + V12}$
HWS1RMS	9	REAL	1	S.D. of HWS1 above
U1AV	10	REAL	1	Average u-component of wind from Stn 1 sonics.
U1RMS	11	REAL	1	Standard deviation of U1 above
V1AV	12	REAL	1	A. v-component of wind from Stn 1 sonics
V1RMS	13	REAL	1	S.D. of V1 above
W1AV	14	REAL	1	A. w-component of wind from Stn 1 sonics
W1RMS	15	REAL	1	S.D. of W1 above
SPEED1AV	16	REAL	1	A. wind speed from Stn 1 PROPVANE
SPEED1RMS	17	REAL	1	S.D. of SPEED1 above
VANE1AV	18	REAL	1	A. vane angle in degrees from Stn 1 PROPVANE
VANE1RMS	19	REAL	1	S.D. of VANE1 above
U1ROTATED	20	REAL	1	U1AV above rotated into average wind angle θ .
V1ROTATED	21	REAL	1	V1AV above rotated into average wind angle θ .
OPTCLRAIN1	22	REAL	1	Un-normalized average output of the Optical Rain Gauge at Stn 1.
U1PV1	23	REAL	1	Rotated wind stress
U1VARROTED	24	REAL	1	Rotated U1VAR above
V1VARROTED	25	REAL	1	Rotated V1VAR above
USTR31	26	REAL	1	Friction velocity parameter from Stn 1
USTR3W1	27	REAL	1	Friction velocity parameter assuming horizontal homogeneity, from Stn 1
ZOVR1	28	REAL	1	Dry air buoyancy, Z/L stability parameter
ZOVR1W1	29	REAL	1	Z/L above assuming a horizontally homogenous surface layer.
AIRDEN1	30	REAL	1	Density of dry air gm-3 with NCAR correction for humidity eqn
QV1	31	REAL	1	Total heat flux from Stn 1
ZOVR1V1	32	REAL	1	Moist air buoyant stability parameter at Stn 1.
ZOVR1W1	33	REAL	1	Moist air buoyant stability using horizontal homogeneity at Stn 1.
CN2RAD1	34	REAL	1	Radio frequency refractive index structure parameter
Q1T11	35	REAL	1	Cross correlation of Stn 1 Lyman alpha humidity with it's fine wire
Q1T21	36	REAL	1	Cross correlation of Stn 1 Lyman alpha humidity with the sonics wire
T1T21	37	REAL	1	Cross correlation of Stn 1 Lyman alpha wire and sonics wire
Q1W1	38	REAL	1	Humidity flux at Stn 1 gm-2s-1
T11W1	39	REAL	1	Temperature flux from Stn 1 Lyman alpha wire Deg-K m s-1
T21W1	40	REAL	1	Temperature flux from Stn 1 Sonics wire
U1W1	41	REAL	1	Cross correlation of sonics u with sonics v at Stn 1
V1W1	42	REAL	1	Wind stress in Boom normal coordinates
W1W1	43	REAL	1	Cross correlation of sonics v with sonics w at Stn 1
SSL101	44	REAL	1	Space-lagged humidity-temperature structure parameter
SSL1T1	45	REAL	1	Space-lagged Temperature structure parameter
TW1	46	REAL	1	Average wet-bulb temperature Deg C from Stn 1 psychrometer
TD1	47	REAL	1	Average Dry-bulb (air) temperature Deg C from Stn 1 psychrometer

Table A-2

Dictionary of ANSWERS File Data

VAR NAME	VAR POSITION	VAR TYPE	VAR SIZE	Meaning
WATERV0EN1	48	REAL	1	Absolute humidity gm-3 from Stn 1 psychrometer temps and psychrometric eqn
CN21	49	REAL	1	Optical refractive index structure parameter from Stn 1.
CT21	50	REAL	1	Temperature structure parameter via optical CA at Stn 1.
THETA1	51	REAL	1	Rotation angle, B, used for Stn 1 data.
PRESSURE	52	REAL	1	Barometric pressure in mb at the field site
DROPSIZES	53	REAL	129	Un-normalized rain drop size distribution
TIMELAGS1	182	REAL	12	Time lagged structure parameters from Stn 1
TIMELAGS2	194	REAL	12	Time lagged structure parameters from Stn 1
Q2AV	206	REAL	1	A. absolute humidity from Stn 2 Lyman alpha hygrometer in gm-3
Q2RMS	207	REAL	1	S.D. of Q2 above
T12AV	208	REAL	1	A. temperature fluctuations at Stn 2 Lyman alpha fine wire in Deg K
T12RMS	209	REAL	1	S.D. of T12 above
T22AV	210	REAL	1	A. temperature fluctuations at Stn 2 Sonics fine wire in Deg K
T22RMS	211	REAL	1	S.D. of T22 above
HWS2AV	212	REAL	1	A. horizontal wind speed, $\sqrt{U22^2 + V22^2}$, from Stn 2 sonics
HWS2RMS	213	REAL	1	S.D. of HWS2 above
U2AV	214	REAL	1	A. u-component of wind at Stn 2 in Boom normal coordinates
U2RMS	215	REAL	1	S.D. of U2 above
V2AV	216	REAL	1	A. v-component of wind at Stn 2 in Boom normal coordinates
V2RMS	217	REAL	1	S.D. of V2 above
W2AV	218	REAL	1	A. vertical wind at Stn 2
W2RMS	219	REAL	1	S.D. of W2 above
SPEED2AV	220	REAL	1	A. wind speed from Stn 2 PROPVANE
SPEED2RMS	221	REAL	1	S.D. of SPEED2 above
VANE2AV	222	REAL	1	A. wind direction relative to the boom at Stn 2
VANE2RMS	223	REAL	1	S.D. of VANE2 above
U2ROTATED	224	REAL	1	A. U2 above rotated; ie downwind component at Stn 2
V2ROTATED	225	REAL	1	A. V2 above rotated; ie cross wind component at Stn 2
OPTCLRAIN2	226	REAL	1	Un-normalized output of Stn 2 optical Raingauge, Volts DC
U2PW2	227	REAL	1	A. wind stress in stream-normal coordinates
U2VARROTATED	228	REAL	1	S.D. of U2ROTATED above
V2VARROTATED	229	REAL	1	S.D. of V2ROTATED above
USTR32	230	REAL	1	Friction velocity parameter at Stn 2.
USTR3H2	231	REAL	1	Friction velocity parameter at Stn 2 using horizontal homogeneity.
ZOVRL2	232	REAL	1	Dry air buoyant stability parameter Z/L at Stn 2
ZOVRLH2	233	REAL	1	Dry air buoyant stability parameter assuming horizontal homogeneity
AIRDEN2	234	REAL	1	Density of dry air at Stn 2 gm-3
QV2	235	REAL	1	Total heat flux at Stn 2.
ZOVRLV2	236	REAL	1	Moist air buoyant stability parameter at Stn 2
ZOVRLW2	237	REAL	1	Moist air Buoyant stability using horizontal homogeneity at Stn 2
CN2RA02	238	REAL	1	Radio frequency refractive index structure parameter at Stn 2
Q2T12	239	REAL	1	Cross correlation of Lyman alpha humidity with it's fine wire at Stn 2
Q2T22	240	REAL	1	Cross correlation of Lyman alpha humidity with the sonics fine wire at Stn 2
T1T22	241	REAL	1	Cross correlation of Lyman alpha wire with sonics wire at Stn 2
Q2W2	242	REAL	1	Humidity flux gm-2s-1 at Stn 2
T12W2	243	REAL	1	Temperature flux based on Lyman alpha wire at Stn 2
T22W2	244	REAL	1	Temperature flux based on sonics wire at Stn 2
U2V2	245	REAL	1	Cross correlation of sonics u with sonics v at Stn 2
U2W2	246	REAL	1	Wind stress at Stn 2 in boom-normal coordinates
V2W2	247	REAL	1	Cross correlation of sonics v with sonics w at Stn 2
SSLTQ2	248	REAL	1	Space lagged humidity-temperature structure parameter at Stn 2

Table A-2

Dictionary of ANSWERS File Data

VAR NAME	VAR POSITION	VAR TYPE	VAR SIZE	Meaning
SSLT12	249	REAL	1	Space lagged temperature structure parameter at Stn 2
TW2	250	REAL	1	A. wet bulb temperature Deg C from Stn 2 psychrometer
TD2	251	REAL	1	A. dry bulb (air) temperature Deg c from Stn 2 psychrometer
WATERVDEN2	252	REAL	1	A. absolute humidity calculated from Stn 2 psychrometer data
CN22	253	REAL	1	A. optical refractive index structure parameter measured at Stn 2
CT22	254	REAL	1	Temperature structure parameter calculated from C2 above at Stn 2
THETA2	255	REAL	1	Rotation angle used to rotated wind related data at Stn 2
SOLARAV	256	REAL	1	A. solar irradiance Wm-2 at the site
SOLARRHS	257	REAL	1	S.D. of solar irradiance above
MAXIN	258	INT	1	The maximum number of 25.6 data records useable for this tape
WEATHER	259	INT	1	Weather condition code
ISTAT	260	INT	1	Stationary interval number
THETSELECT	261	INT	2	Wind rotation selection code for each MET station
METFLAGS	263	FLAGS	12	Met station instrument status flags...not used
OPTXWIND1	275	REAL	1	A. wind across mm wave propagation path from Stn 1 optical crosswind sensor m/s
OPTXWIND2	276	REAL	1	A. wind across mm wave propagation path from Stn 2 optical crosswind sensor m/s
MMFREQ	277	REAL	1	mm wave transmitter frequency
T1	278	REAL	1	Time in seconds from start of tape to begin interval MET statistics
T2	279	REAL	1	Time in seconds from start of tape to end interval MET statistics
***** Millimeter Wave Data Statistics block *****				
NAME	280	INT	1	Same as RUNID. Used to check for possible error
NSWPPER	281	INT	1	RC Filter time constant, sec/radian, if used
RCFILTERNST	282	REAL	1	The number of filter on the filter file called
MFILTERS	283	INT	1	The number of intensity PDF bins
NBININTEN	284	INT	1	The minimum intensity value of each of 4 intensity PDF's
NBINMININT	285	REAL	4	The maximum intensity value of each of 4 intensity PDF's
BINMAXINT	289	REAL	4	The number of Phase-difference PDF bins in each of 6 Phase Diff PDF's
NBINPHAS	293	INT	1	The min phase difference in each of 6 phase difference PDF's
BINMINPHAS	294	REAL	6	The max phase difference in each of 6 phase difference PDF's
BINMAXPHAS	300	REAL	6	The number of breakpoints in the MIL data for this interval
NTIMES	306	REAL	1	Time in seconds from start of tape to begin MIL statistics interval
TIME1	307	REAL	1	Free space
FREE2	308	FREE	9	Time in seconds from start of tape to end MIL statistics interval
TIME2	317	REAL	1	Free space
FREE3	318	FREE	9	A. Intensity in each of 4 antennas
INTNSTYAV	327	REAL	4	S.D. of intensity at each of 4 antennas
INTNSTYVAR	331	REAL	4	A. unfiltered intensity at each of 4 antennas
INTNSTUFV	335	REAL	4	Intensity covariance at each of 6 antenna pairs
INTNSTYCOV	339	REAL	6	Real part of the mutual coherence function at each of 6 phase diff pairs
RENCFAV	345	REAL	6	Im part of the MCF at each of 6 phase difference pairs
IMCFAV	351	REAL	6	A. phase difference at each of 6 antenna pairs
PHASEDIFAV	357	REAL	6	Variance of phase differences at each of 6 antenna pairs
PHASDIFVAR	363	REAL	6	First 6 elem are eqn 7 ref 1. Second 6 are 2nd term in brackets
XPROD	369	REAL	12	A. Real part of M4. note 2
REFOURAV	381	REAL	33	A. Imaginary part of M4. note 2
INTFOURAV	414	REAL	33	notes 1 and 3
FIGAR	447	REAL	12	notes 1 and 4
FIGVAR	459	REAL	17	Minimum intensity at each antenna in the interval. note 1
INTNSTYMIN	476	REAL	4	

Table A-2

Dictionary of ANSWERS File Data

VAR NAME	VAR POSITION	VAR TYPE	VAR SIZE	Meaning
PHASDIFMIN	480	REAL	6	Minimum phase difference at each antenna pair in the interval. note 2
INTNSTYMAX	486	REAL	4	Maximum intensity at each antenna in the interval. note 1
PHASDIFMAX	490	REAL	6	Maximum phase difference at each antenna pair in the interval. note 2
MCFAAMPLAV	496	REAL	6	A. Modulus of MCF for each antenna pair. note 2
MCFPHASAV	502	REAL	6	A. Phase of MCF for each antenna pair. note 2
MLFFTHDR	508	REAL	1537	FFT program processing header. Required only re-create the spectra
LFREQBINS	2045	REAL	36	Log-spaced frequency bin assignments
LF11POWER	2081	REAL	36	Antenna 1 intensity power spectra
LF12POWER	2117	REAL	36	Antenna 2 intensity power spectra
LF13POWER	2153	REAL	36	Antenna 3 intensity power spectra
LF14POWER	2189	REAL	36	Antenna 4 intensity power spectra
LF12POWER	2225	REAL	36	Phase difference (11-12) power spectra
LF13POWER	2261	REAL	36	Phase difference (11-13) power spectra
LF14POWER	2297	REAL	36	Phase difference (11-14) power spectra
LF23POWER	2333	REAL	36	Phase difference (12-13) power spectra
LF24POWER	2369	REAL	36	Phase difference (12-14) power spectra
LF34POWER	2405	REAL	36	Phase difference (13-14) power spectra
LFC12COSPC	2441	REAL	36	see note 6
LFC1200SPC	2477	REAL	36	see note 6
LFC13COSPC	2513	REAL	36	see note 6
LFC1300SPC	2549	REAL	36	see note 6
LFC14COSPC	2585	REAL	36	see note 6
LFC1400SPC	2621	REAL	36	see note 6
LFC23COSPC	2657	REAL	36	see note 6
LFC2300SPC	2693	REAL	36	see note 6
LFC24COSPC	2729	REAL	36	see note 6
LFC2400SPC	2765	REAL	36	see note 6
LFC34COSPC	2801	REAL	36	see note 6
LFC3400SPC	2837	REAL	36	see note 6
LFC58COSPC	2873	REAL	36	see note 6
LFC5800SPC	2909	REAL	36	see note 6
LFC59COSPC	2945	REAL	36	see note 6
LFC5900SPC	2981	REAL	36	see note 6
LFC80COSPC	3017	REAL	36	see note 6
LFC8000SPC	3053	REAL	36	see note 6
LFC60COSPC	3089	REAL	36	see note 6
LFC6000SPC	3125	REAL	36	see note 6
LFC69COSPC	3161	REAL	36	see note 6
LFC6900SPC	3197	REAL	36	see note 6
LFC50COSPC	3233	REAL	36	see note 6
LFC5000SPC	3269	REAL	36	see note 6
LFC37COSPC	3305	REAL	36	see note 6
LFC3700SPC	3341	REAL	36	see note 6
LFC26COSPC	3377	REAL	36	see note 6
LFC2600SPC	3413	REAL	36	see note 6
LFC15COSPC	3449	REAL	36	see note 6
LFC1500SPC	3485	REAL	36	see note 6
LFC16COSPC	3521	REAL	36	see note 6
LFC1600SPC	3557	REAL	36	see note 6
LFC17COSPC	3593	REAL	36	see note 6
LFC1700SPC	3629	REAL	36	see note 6

Table A-2

Dictionary of ANSWERS File Data

VAR NAME	VAR POSITION	VAR TYPE	VAR SIZE	Meaning
LFC25COSPC	3665	REAL	36	see note 6
LFC2500SPC	3701	REAL	36	see note 6
LFC28COSPC	3737	REAL	36	see note 6
LFC2800SPC	3773	REAL	36	see note 6
LFC29COSPC	3809	REAL	36	see note 6
LFC2900SPC	3845	REAL	36	see note 6
LFC36COSPC	3881	REAL	36	see note 6
LFC3600SPC	3917	REAL	36	see note 6
LFC38COSPC	3953	REAL	36	see note 6
LFC3800SPC	3989	REAL	36	see note 6
LFC30COSPC	4025	REAL	36	see note 6
LFC3000SPC	4061	REAL	36	see note 6
LFC47COSPC	4097	REAL	36	see note 6
LFC4700SPC	4133	REAL	36	see note 6
LFC49COSPC	4169	REAL	36	see note 6
LFC4900SPC	4205	REAL	36	see note 6
LFC40COSPC	4241	REAL	36	see note 6
LFC4000SPC	4277	REAL	36	see note 6

***** MIL data high frequency power spectra *****

HFFREQ81MS	4313	REAL	72	see note 6
HFI1POWER	4385	REAL	72	see note 6
HFI2POWER	4457	REAL	72	see note 6
HFI3POWER	4529	REAL	72	see note 6
HFI4POWER	4601	REAL	72	see note 6
HFI12POWER	4673	REAL	72	see note 6
HFI13POWER	4745	REAL	72	see note 6
HFI14POWER	4817	REAL	72	see note 6
HFI23POWER	4889	REAL	72	see note 6
HFI24POWER	4961	REAL	72	see note 6
HFI34POWER	5033	REAL	72	see note 6
HFC12COSPC	5105	REAL	72	see note 6
HFC1200SPC	5177	REAL	72	see note 6
HFC13COSPC	5249	REAL	72	see note 6
HFC1300SPC	5321	REAL	72	see note 6
HFC14COSPC	5393	REAL	72	see note 6
HFC1400SPC	5465	REAL	72	see note 6
HFC23COSPC	5537	REAL	72	see note 6
HFC2300SPC	5609	REAL	72	see note 6
HFC24COSPC	5681	REAL	72	see note 6
HFC2400SPC	5753	REAL	72	see note 6
HFC34COSPC	5825	REAL	72	see note 6
HFC3400SPC	5897	REAL	72	see note 6
HFC58COSPC	5969	REAL	72	see note 6
HFC5800SPC	6041	REAL	72	see note 6
HFC59COSPC	6113	REAL	72	see note 6
HFC5900SPC	6185	REAL	72	see note 6
HFC80COSPC	6257	REAL	72	see note 6
HFC8000SPC	6329	REAL	72	see note 6

Table A-2

Dictionary of ANSWERS File Data

VAR NAME	VAR POSITION	VAR TYPE	VAR SIZE	Meaning
HFC6000SPC	6401	REAL	72	see note 6
HFC6000SPC	6473	REAL	72	see note 6
HFC6000SPC	6545	REAL	72	see note 6
HFC6000SPC	6617	REAL	72	see note 6
HFC5000SPC	6689	REAL	72	see note 6
HFC5000SPC	6761	REAL	72	see note 6
HFC3700SPC	6833	REAL	72	see note 6
HFC2600SPC	6905	REAL	72	see note 6
HFC2600SPC	6977	REAL	72	see note 6
HFC2600SPC	7049	REAL	72	see note 6
HFC1500SPC	7121	REAL	72	see note 6
HFC1500SPC	7193	REAL	72	see note 6
HFC1600SPC	7265	REAL	72	see note 6
HFC1600SPC	7337	REAL	72	see note 6
HFC1700SPC	7409	REAL	72	see note 6
HFC2500SPC	7481	REAL	72	see note 6
HFC2500SPC	7553	REAL	72	see note 6
HFC2500SPC	7625	REAL	72	see note 6
HFC2800SPC	7697	REAL	72	see note 6
HFC2800SPC	7769	REAL	72	see note 6
HFC2900SPC	7841	REAL	72	see note 6
HFC3600SPC	7913	REAL	72	see note 6
HFC3600SPC	7985	REAL	72	see note 6
HFC3600SPC	8057	REAL	72	see note 6
HFC3800SPC	8129	REAL	72	see note 6
HFC3800SPC	8201	REAL	72	see note 6
HFC3000SPC	8273	REAL	72	see note 6
HFC3000SPC	8345	REAL	72	see note 6
HFC4700SPC	8417	REAL	72	see note 6
HFC4700SPC	8489	REAL	72	see note 6
HFC4900SPC	8561	REAL	72	see note 6
HFC4900SPC	8633	REAL	72	see note 6
HFC4000SPC	8705	REAL	72	see note 6
HFC4000SPC	8777	REAL	72	see note 6
***** MET Stations Spectra processing headers *****				
MTFND1FLAG	8849	FLAG (INT)	1	MET Station 1 100 Hz data FFT header entry flag
MTFFT1HEAD	8850	REAL	2049	MET Station 1 100 Hz data FFT processing header.
MTFND2FLAG	10899	FLAG	1	MET Station 2 100 Hz data FFT header entry flag
MTFFT2HEAD	10900	REAL	2049	MET Station 2 100 Hz data FFT processing header
MTFND3FLAG	12949	FLAG	1	MET Station 1 25 Hz data FFT header entry flag
MTFFT3HEAD	12950	REAL	2049	MET Station 1 25 Hz data FFT processing header
MTFND4FLAG	14999	FLAG	1	MET Station 2 25 Hz data FFT header entry flag
MTFFT4HEAD	15000	REAL	2049	MET Station 2 25 Hz data FFT processing header
***** MET Station 1 100 Hz data low frequency spectra *****				
MTFFT1FLAG	17049	FLAG	1	MET Station 1 100 Hz data FFT entry flag
S1LF100FBN	17050	REAL	36	Low frequency FFT frequency bin assignments
S1LYA10LPS	17086	REAL	36	Strn 1 Lyman-alpha power spectra

Req'd to recreate spectra

Table A-2
Dictionary of ANSWERS File Data

VAR NAME	VAR POSITION	VAR TYPE	VAR SIZE	Meaning
S1TL10LPS	17122	REAL	36	Stn 1 Lyman-alpha wire power spectra
S1TS10LPS	17158	REAL	36	Stn 1 Sonics wire power spectra
S1RAMPL	17194	REAL	36	Spectra of a continuous ramp (a filler)
S1QTL10LCO	17230	REAL	36	Stn 1 Lyman-alpha hygrometer X Lyman alpha wire Co-spectra
S1QTL10LQD	17266	REAL	36	Quadrature spectra of the above pair
S1QTL10LNC	17302	REAL	36	Normalized Co-spectra of the above pair
S1QTL10LMQ	17338	REAL	36	Normalized quadrature spectra of the above pair
S1QTL10LCH	17374	REAL	36	Coherence spectra of the above pair
S1QTL10LPH	17410	REAL	36	Phase spectra of the above pair
***** MET Station 1 100 Hz data high frequency spectra *****				
S1MF100FBM	17446	REAL	36	Frequency bin assignments
S1LYA10HPS	17482	REAL	36	Stn 1 Lyman alpha hygrometer power spectra
S1TL100HPS	17518	REAL	36	Stn 1 Lyman alpha wire power spectra
S1TS100HPS	17554	REAL	36	Stn 1 Sonics wire power spectra
S1RAMPH	17590	REAL	36	Filler spectra
S1QTL10HCO	17626	REAL	36	Lyman-alpha hygrometer X Lyman-alpha wire co-spectra
S1QTL10HQD	17662	REAL	36	Quadrature spectra of the above pair
S1QTL10HNC	17698	REAL	36	Normalized Co-spectra of the above pair
S1QTL10HMQ	17734	REAL	36	Normalized quadrature spectra of the above pair
S1QTL10HCH	17770	REAL	36	Coherence spectra of the above pair
S1QTL10HCH	17806	REAL	36	Phase spectra of the above pair
***** MET Station 2 100 Hz data low frequency spectra *****				
M1FFT2FLAG	17842	FLAG	1	MET Station 2 100 Hz data Low frequency FFT entry flag
S2LF100FBM	17843	REAL	36	Low frequency bin assignments
S2LYA10LPS	17879	REAL	36	Stn 2 Lyman-alpha hygrometer power spectra
S2TL100LPS	17915	REAL	36	Stn 2 Lyman-alpha wire power spectra
S2TS100LPS	17951	REAL	36	Stn 2 Sonics wire power spectra
S2RAMPL	17987	REAL	36	Filler data
S2QTL10LCO	18023	REAL	36	Lyman-alpha hygrometer X Lyman alpha wire co-spectra
S2QTL10LQD	18059	REAL	36	Quadrature spectra for the above pair
S2QTL10LNC	18095	REAL	36	Normalized co-spectra for the above pair
S2QTL10LMQ	18131	REAL	36	Normalized quadrature spectra for the above pair
S2QTL10LCH	18167	REAL	36	Coherence spectra for the above pair
S2QTL10LPH	18203	REAL	36	Phase spectra for the above pair
***** MET Station 2 100 Hz data high frequency spectra *****				
S2HF100FBM	18239	REAL	36	Frequency bin assignments
S2LYA10HPS	18275	REAL	36	Stn 2 Lyman-alpha hygrometer power spectra
S2TL100HPS	18311	REAL	36	Stn 2 Lyman-alpha wire power spectra
S2TS100HPS	18347	REAL	36	Stn 2 Sonics wire power spectra
S2RAMPH	18383	REAL	36	Filler data
S2QTL10HCO	18419	REAL	36	Lyman-alpha hygrometer X Lyman alpha wire co-spectra
S2QTL10HQD	18455	REAL	36	Quadrature spectra of the above pair
S2QTL10HNC	18491	REAL	36	Normalized Co-spectra of the above pair
S2QTL10HMQ	18527	REAL	36	Normalized quadrature spectra of the above pair
S2QTL10HCH	18563	REAL	36	Coherence spectra of the above pair

Table A-2

Dictionary of ANSWERS File Data

VAR NAME	VAR POSITION	VAR TYPE	VAR SIZE	Meaning
S20TL10NPH	18599	REAL	36	Phase spectra of Lyman alpha hygrometer X Lyman alpha wire
***** MET Station 1 25 Hz data low frequency spectra *****				
MTFF3FLAG	18635	FLAG	1	Station 1 25 Hz data FFT entry flag
S1LF25FBN	18636	REAL	36	Low frequency bin assignments
S1LYA25LPS	18672	REAL	36	Stn 1 Lyman alpha hygrometer power spectra
S1TL25LPS	18708	REAL	36	Stn 1 Lyman alpha wire power spectra
S1TS25LPS	18744	REAL	36	Stn 1 Sonics wire power spectra
S1U25LPS	18780	REAL	36	Stn 1 Sonics u power spectra
S1V25LPS	18816	REAL	36	Stn 1 Sonics v power spectra
S1W25LPS	18852	REAL	36	Stn 1 Sonics w power spectra
S10TL25LCO	18888	REAL	36	Lyman-alpha hygrometer X Lyman alpha wire Co-spectra
S10TL25LQO	18924	REAL	36	Quadrature spectra of the above pair
S10TL25LNC	18960	REAL	36	Normalized co-spectra of the above pair
S10TL25LCH	18996	REAL	36	Normalized quadrature spectra of the above pair
S10TL25LPH	19032	REAL	36	Coherence spectra of the above pair
S10TL25LPH	19068	REAL	36	Phase spectra of the above pair
S10W25LCO	19104	REAL	36	Lyman-alpha hygrometer X Sonics u co-spectra
S10W25LQO	19140	REAL	36	
S10W25LNC	19176	REAL	36	
S10W25LNG	19212	REAL	36	
S10W25LCH	19248	REAL	36	
S10W25LPH	19284	REAL	36	
S1TSW25LCO	19320	REAL	36	Stn 1 Sonics w X Sonics wire co-spectra
S1TSW25LQO	19356	REAL	36	
S1TSW25LNC	19392	REAL	36	
S1TSW25LNG	19428	REAL	36	
S1TSW25LCH	19464	REAL	36	
S1TSW25LPH	19500	REAL	36	Stn 1 Sonics u X Sonics v Co-spectra
S1UV25LCO	19536	REAL	36	
S1UV25LQO	19572	REAL	36	
S1UV25LNC	19608	REAL	36	
S1UV25LNG	19644	REAL	36	
S1UV25LCH	19680	REAL	36	
S1UM25LCO	19716	REAL	36	Stn 1 Sonics u X Sonics w Co-spectra
S1UM25LQO	19752	REAL	36	
S1UM25LNC	19788	REAL	36	
S1UM25LNG	19824	REAL	36	
S1UM25LCH	19860	REAL	36	
S1UM25LPH	19896	REAL	36	
S1VW25LCO	19932	REAL	36	Stn 1 Sonics v X Sonics w co-spectra
S1VW25LQO	19968	REAL	36	
S1VW25LNC	20004	REAL	36	
S1VW25LNG	20040	REAL	36	
S1VW25LCH	20076	REAL	36	
S1VW25LPH	20112	REAL	36	
	20148	REAL	36	

Table A-2

Dictionary of ANSWERS File Data

VAR NAME	VAR POSITION	VAR TYPE	VAR SIZE	Meaning
***** MET Station 1 25 Hz data high frequency spectra *****				
S1NF25FBN	20184	REAL	36	Stn 1 25 Hz data lf FFT frequency bin assignments
S1LYA25HPS	20220	REAL	36	Stn 1 Lyman-alpha hygrometer power spectra
S1TL25HPS	20256	REAL	36	Stn 1 Lyman-alpha wire power spectra
S1TS25HPS	20292	REAL	36	Stn 1 Sonics wire power spectra
S1U25HPS	20328	REAL	36	Stn 1 Sonics u power spectra
S1V25HPS	20364	REAL	36	Stn 1 Sonics v power spectra
S1W25HPS	20400	REAL	36	Stn 1 Sonics w power spectra
S1QTL25HCO	20436	REAL	36	Lyman-alpha hygrometer X Lyman-alpha wire Co-spectra
S1QTL25HQD	20472	REAL	36	
S1QTL25HNC	20508	REAL	36	
S1QTL25HNQ	20544	REAL	36	
S1QTL25HCH	20580	REAL	36	
S1QTL25HPH	20616	REAL	36	
S1QW25HCO	20652	REAL	36	
S1QW25HQD	20688	REAL	36	
S1QW25HNC	20724	REAL	36	
S1QW25HNQ	20760	REAL	36	
S1QW25HCH	20796	REAL	36	
S1QW25HPH	20832	REAL	36	
S1TSW25HCO	20868	REAL	36	Sonics wire X sonics w Co-spectra
S1TSW25HQD	20904	REAL	36	
S1TSW25HNC	20940	REAL	36	
S1TSW25HNQ	20976	REAL	36	
S1TSW25HCH	21012	REAL	36	
S1TSW25HPH	21048	REAL	36	
S1UV25HCO	21084	REAL	36	Sonics u X Sonics v co-spectra
S1UV25HQD	21120	REAL	36	
S1UV25HNC	21156	REAL	36	
S1UV25HNQ	21192	REAL	36	
S1UV25HCH	21228	REAL	36	
S1UV25HPH	21264	REAL	36	
S1UW25HCO	21300	REAL	36	Sonics u X sonics w co-spectra
S1UW25HQD	21336	REAL	36	
S1UW25HNC	21372	REAL	36	
S1UW25HNQ	21408	REAL	36	
S1UW25HCH	21444	REAL	36	
S1UW25HPH	21480	REAL	36	
S1VW25HCO	21516	REAL	36	Sonics v X Sonics w co-spectra
S1VW25HQD	21552	REAL	36	
S1VW25HNC	21588	REAL	36	
S1VW25HNQ	21624	REAL	36	
S1VW25HCH	21660	REAL	36	
S1VW25HPH	21696	REAL	36	
***** MET Station 2 25 Hz data low frequency spectra *****				
MTFF14FLAG	21732	FLAG	1	MET Station 2 25 Hz data FFT entry flag
S2LF25FBN	21733	REAL	36	Low frequency bin assignments

Table A-2

Dictionary of ANSMERS File Data

VAR NAME	VAR POSITION	VAR TYPE	VAR SIZE	Meaning
S2LYA25LPS	21769	REAL	36	Lyman-alpha hygrometer power spectra
S2TL25LPS	21805	REAL	36	Lyman-alpha wire power spectra
S2TS25LPS	21841	REAL	36	Sonics wire power spectra
S2U25LPS	21877	REAL	36	Stn 2 Sonics u low frequency power spectra
S2V25LPS	21913	REAL	36	Sonics v power spectra
S2W25LPS	21949	REAL	36	sonics w power spectra
S20TL25LCO	21985	REAL	36	Lyman-alpha hygrometer X Lyman-alpha wire co-spectra
S20TL25LQD	22021	REAL	36	
S20TL25LNC	22057	REAL	36	
S20TL25LNO	22093	REAL	36	
S20TL25LCH	22129	REAL	36	
S20TL25LPH	22165	REAL	36	
S20W25LCO	22201	REAL	36	
S20W25LQD	22237	REAL	36	
S20W25LNC	22273	REAL	36	
S20W25LNO	22309	REAL	36	
S20W25LCH	22345	REAL	36	
S20W25LPH	22381	REAL	36	
S2TSW25LCO	22417	REAL	36	Sonics wire X Sonics w co-spectra
S2TSW25LQD	22453	REAL	36	
S2TSW25LNC	22489	REAL	36	
S2TSW25LNO	22525	REAL	36	
S2TSW25LCH	22561	REAL	36	
S2TSW25LPH	22597	REAL	36	
S2UW25LCO	22633	REAL	36	Sonics u X sonics v co-spectra
S2UW25LQD	22669	REAL	36	
S2UW25LNC	22705	REAL	36	
S2UW25LNO	22741	REAL	36	
S2UW25LCH	22777	REAL	36	
S2UW25LPH	22813	REAL	36	
S2W25LCO	22849	REAL	36	Sonics u X sonics w co-spectra
S2W25LQD	22885	REAL	36	
S2W25LNC	22921	REAL	36	
S2W25LNO	22957	REAL	36	
S2W25LCH	22993	REAL	36	
S2W25LPH	23029	REAL	36	
S2W25LQD	23065	REAL	36	Sonics v X sonics w co-spectra
S2W25LNC	23101	REAL	36	
S2W25LNO	23137	REAL	36	
S2W25LCH	23173	REAL	36	
S2W25LPH	23209	REAL	36	
S2W25LQD	23245	REAL	36	
***** MET Station 2 25 Hz data high frequency spectra *****				
S2WF25FBN	23281	REAL	36	Frequency bin assignments
S2LYA25HPS	23317	REAL	36	Lyman-alpha hygrometer power spectra
S2TL25HPS	23353	REAL	36	Lyman-alpha wire power spectra
S2TS25HPS	23389	REAL	36	Sonics wire power spectra
S2U25HPS	23425	REAL	36	Sonics u power spectra
S2V25HPS	23461	REAL	36	Sonics v power spectra

Table A-2

Dictionary of ANSWERS File Data

VAR NAME	VAR POSITION	VAR TYPE	VAR SIZE	Meaning
S2W25HPS	23497	REAL	36	Sonics w power spectra Lyman-alpha hygrometer X Lyman-alpha wire co-spectra
S2QTL25HCO	23533	REAL	36	
S2QTL25HQD	23569	REAL	36	
S2QTL25HNC	23605	REAL	36	
S2QTL25HNQ	23641	REAL	36	Stn 2 Lyman-alpha hygrometer X Sonics w hf co-spectra
S2QTL25HCH	23677	REAL	36	
S2QTL25HPH	23713	REAL	36	
S2QW25HCO	23749	REAL	36	
S2QW25HQD	23785	REAL	36	Sonics wire X Sonics w co-spectra
S2QW25HNC	23821	REAL	36	
S2QW25HNQ	23857	REAL	36	
S2QW25HCH	23893	REAL	36	
S2QW25HPH	23929	REAL	36	Sonics u X sonics v co-spectra
S2TSW25HCO	23965	REAL	36	
S2TSW25HQD	24001	REAL	36	
S2TSW25HNC	24037	REAL	36	
S2TSW25HNQ	24073	REAL	36	Sonics u X sonics w co-spectra
S2TSW25HCH	24109	REAL	36	
S2TSW25HPH	24145	REAL	36	
S2UV25HCO	24181	REAL	36	
S2UV25HQD	24217	REAL	36	Sonics u X sonics w co-spectra
S2UV25HNC	24253	REAL	36	
S2UV25HNQ	24289	REAL	36	
S2UV25HCH	24325	REAL	36	
S2UV25HPH	24361	REAL	36	Sonics v X sonics W co-spectra
S2UM25HCO	24397	REAL	36	
S2UM25HQD	24433	REAL	36	
S2UM25HNC	24469	REAL	36	
S2UM25HNQ	24505	REAL	36	Antenna 1 probability density function
S2UM25HCH	24541	REAL	36	
S2UM25HPH	24577	REAL	36	
S2VM25HCO	24613	REAL	36	
S2VM25HQD	24649	REAL	36	Antenna 2 probability density function
S2VM25HNC	24685	REAL	36	
S2VM25HNQ	24721	REAL	36	
S2VM25HCH	24757	REAL	36	
S2VM25HPH	24793	REAL	36	Antenna 3 probability density function
				Antenna 4 probability density function
				Phase difference pair 1 probability density function
				Phase difference pair 2 probability density function
				Phase difference pair 3 probability density function
				Phase difference pair 4 probability density function
				Phase difference pair 5 probability density function
				Phase difference pair 6 probability density function

***** MIL data probability densities *****

I1PDF	24829	REAL	50	Antenna 1 probability density function
I2PDF	24879	REAL	50	Antenna 2 probability density function
I3PDF	24929	REAL	50	Antenna 3 probability density function
I4PDF	24979	REAL	50	Antenna 4 probability density function
P012PDF	25029	REAL	50	Phase difference pair 1 probability density function
P013PDF	25079	REAL	50	Phase difference pair 2 probability density function
P014PDF	25129	REAL	50	Phase difference pair 3 probability density function
P023PDF	25179	REAL	50	Phase difference pair 4 probability density function
P024PDF	25229	REAL	50	Phase difference pair 5 probability density function
P034PDF	25279	REAL	50	Phase difference pair 6 probability density function

Table A-2

Dictionary of ANSWERS File Data

VAR NAME	VAR POSITION	VAR TYPE	VAR SIZE	Meaning
***** MET data PDF limits *****				
Q1JPDFMIN	25329	REAL	1	Lower limit of Stn 1 JPDF along humidity axis
QJPDFMAX	25330	REAL	1	Upper limit of Stn 1 JPDF along humidity axis
TL1JPDFMIN	25331	REAL	1	Lower limit of Stn 1 JPDF along Temperature fluctuations axis
BOOMANGLE1	25332	REAL	1	Stn1 Boom angle encoder output in degrees
TL1JPDFMAX	25333	REAL	1	Upper limit of Stn 1 JPDF along Temperature fluctuations axis
BOOMANGLE2	25334	REAL	1	Stn2 Boom angle encoder output in degrees
VANE1PDFMIN	25335	REAL	1	Lower limit of Stn 1 Vane angle PDF
VANE1PDFMAX	25336	REAL	1	Upper limit of Stn 1 Vane angle PDF

Table A-2

Dictionary of ANSWERS File Data

VAR NAME	VAR POSITION	VAR TYPE	VAR SIZE	Meaning
***** MET data probability densities *****				
SOLARPDFMIN	25337	REAL	1	Lower limit of Solar irradiance PDF
SOLARPDFMAX	25338	REAL	1	Upper limit of Solar irradiance PDF
Q2JPDFMIN	25339	REAL	1	Lower limit of Stn 2 JPDF along humidity axis
Q2JPDFMAX	25340	REAL	1	Upper limit of Stn 2 JPDF along humidity axis
TL2JPDFMIN	25341	REAL	1	Lower limit of Stn 2 JPDF along Temperature fluctuations axis
FREE4	25342	FREE	1	free space
TL2JPDFMAX	25343	REAL	1	Upper limit of Stn 2 JPDF along Temperature fluctuations axis
FREE5	25344	FREE	1	free space
VANE2PDFMIN	25345	REAL	1	Lower limit of Stn 2 Vane angle PDF
VANE2PDFMAX	25346	REAL	1	Upper limit of Stn 2 Vane angle PDF
***** MET data probability densities *****				
VANE1PDF	25347	REAL	50	Stn 1 Vane angle PDF
VANE2PDF	25397	REAL	50	Stn 2 Vane angle PDF
SOLARPDF	25447	REAL	50	Solar irradiance PDF
FREE6	25497	FREE	2	free space
Q1TLJPDF	25499	REAL	2500	Stn 1 JPDF
Q2TLJPDF	27999	REAL	2500	Stn 2 JPDF

APPENDIX B

EXAMPLE OF ACQUIRING DATA THE SIMPLE WAY

Figure B-1 is the FORTRAN-V ('77+) source listing of a demonstration program which reads all clear-air data and retrieves the solar pyranometer output, and from each station; the optical and rf refractive-index structure parameters, and the temperature structure parameter calculated from the optical measurements.

Figure B-2 is a print of the contents of the local file, NEWFIL, created by READATA. The first record contains the number of items requested, and the number of records found that satisfy selection criteria.

As annotated in the source listing, we collect records for all clear air tapes for which the rf refractive index structure parameter lies between 3.12×10^{-14} and 3.16×10^{-11} .

PROGRAM DEMO 74/B35 OPT=0,ROUND=A/ S/ M/D,-DS FTN 5.14628 86/07/01. 17.38.28 PAGE 1
DO=LONG/-OT,ARG=COMMON/-FIXED,CS= USER/-FIXED,DB=1B/-SB/-SL/ ER/-ID/-PMD/-ST,-AL,PL=5000
FTNS,1=DEMO,L=00,L0,B=0.

```

1 PROGRAM DEMO (ANSWERS,NEWFIL,INPUT,OUTPUT,
2 TAPE1=ANSWERS,TAPE2=NEWFIL,TAPE3=INPUT,TAPE4=OUTPUT)
3
4
5
6
7
8
9
10
11
12
13
14
15
16
17
18
19
20
21
22
23
24
25
26
27
28
29
30
31
32
33
34
35
36
37
38
39
40
41
42
43
44
45
46
47
48
49
50
51
52
53
54
55

```

WRITTEN BY MARK WICKERS JUNE 1986

DEMO OF READING THE FOLLOWING VARIABLES
SOLAV, CN2RAD1, CN21, CT21, CN2RAD2, CN22, CT22
FROM THE ANSWERS FILE USING THE SUBROUTINE READATA
FORM TAPES TAKEN DURING CLEAR WEATHER AND WITH CN2RAD BETWEEN
-13 AND -10.

THE RESULTANT DATA IS STORED IN A STANDARD FORTRAN SEQUENTIAL
FORMATTED FILE.

CHARACTER*10 VARRAY(7)
DIMENSION IWEAT(8),ISESS(8),ITAPE(100),IZOVR(8),IFREQ(8),
ICN2RAD(8),ISTAT(8)

DATA IWEAT/8*0/
DATA ISESS/8*0/
DATA ITAPE/100*0/
DATA IZOVR/8*0/
DATA IFREQ/8*0/
DATA ICN2RAD/8*0/
DATA ISTAT/8*0/
DATA VARRAY/7*0/
/

WHEN IWEAT(1) = 1 THIS SPECIFIES FOR CLEAR AIR TAPE ONLY
IWEAT(1) = 1

WHEN ICN2RAD(1) = 3 THEN -11 < CN2RAD <= -10
= 4 THEN -12 < CN2RAD <= -11
= 5 THEN -13 < CN2RAD <= -12

ICN2RAD(1) = 3
ICN2RAD(2) = 4
ICN2RAD(3) = 5

VARRAY IS A CHARACTER*10 ARRAY OF THE VARIABLES DESIRED FROM THESE TAPES

VARRAY(1) = 'SOLAV'
VARRAY(2) = 'CN2RAD1'
VARRAY(3) = 'CN21'
VARRAY(4) = 'CT21'
VARRAY(5) = 'CN2RAD2'
VARRAY(6) = 'CN22'
VARRAY(7) = 'CT22'

NUMVAR = 7

Figure B-1. FORTRAN-77 compiler listing of a program which accesses the data by method I, II.8.1.

```

56 C THE CODE FOR A FORMATTED SEQUENTIAL FORTRAN FILE IS : 2
57 C
58 C IFILE = 2
59 C
60 C CALLING READATA WILL GET ALL THE VARIABLES REQUESTED FOR CLEAR AIR
61 C TAPES AND CN2RAD BETWEEN -13 AND -10. THIS DATA WILL BE IN A LOCAL
62 C FILE WITH DEFAULT NAME = "NEWFIL"
63 C
64 C CALL READATA(1,2,IFILE,IWEAT,ISESS,I2OVR,IFREQ,ITAPE,ICN2RAD,
65 C ,
66 C ISTAT,VARRAY,NUMVAR,NUMREC)
67 C
68 C NUMREC = THE NUMBER OF RECORDS FOUND TO FIT THE DESCRIPTIONS GIVEN
69 C
70 C PRINT *, 'THERE ARE NOW ', NUMREC, ' RECORDS OF DATA IN NEWFIL.'
71 C
72 C END

```

VARIABLE MAP--(LO=A/R)				REFERENCES--				A=ARGLIST, C=CTRL OF DO, I=DATA INIT, R=READ, S=STORE, U=I/O UNIT, W=WRITE			
NAME	ADDRESS	BLOCK	PROPERTIES	TYPE	SIZE	REFERENCES					
ICN2RAD	321B			INTEGER	8	17	25/1	38/S	39/S	40/S	65/A
IFILE	342B			INTEGER	8	17	58/S				
IFREQ	311B			INTEGER	8	17	24/1	65/A			
ISESS	125B			INTEGER	8	17	21/1	65/A			
ISTAT	331B			INTEGER	8	17	26/1	65/A			
ITAPE	135B			INTEGER	100	17	22/1	65/A			
IWEAT	115B			INTEGER	8	17	20/1	32/S		65/A	
I2OVR	301B			INTEGER	8	17	23/1	65/A			
NUMREC	343B			INTEGER	8	17	70/W				
NUMVAR	341B			INTEGER	7	16	53/S	45/S	46/S	47/S	48/S
VARRAY	106B			CHAR*10	7	16	27/1	45/S	46/S	47/S	48/S
										49/S	50/S
											51/S

PROCEDURES--(LO=A/R)

NAME	TYPE	ARGS	CLASS	REFERENCES
READATA		13	SUBROUTINE	65

ENTRY POINTS--(LO=A/R)

NAME	ADDRESS	ARGS	REFERENCES
DEMO	00B	0	1/D

STATISTICS--

PROGRAM-UNIT LENGTH	344B = 228
CM STORAGE USED	62700B = 26048
COMPILE TIME	0.059 SECONDS
15.39.33.UCLP. AA., CLNP04.	0.320KLNS.

Figure B-1. (continued).

21.7
568.653676313 1.981266777151E-13 7.625409718628E-13 1.100256884657 1.073748649244E-13 1.000421704815E-14 .01446906464129
487.7780495099 4.789151669655E-13 8.810637317026E-14 .1275231160092 3.107610028984E-13 8.134659059509E-14 .1170809946659
795.1361851828 2.500870629163E-13 7.934106647018E-13 1.094355956164 2.328550933107E-13 4.044838710665E-13 .5576247132043
583.8527099459 4.077980323238E-14 6.277723985742E-13 .873738008473 1.955784412914E-13 2.928681213431E-13 .4073678694335
556.5829205906 1.110956537393E-13 7.625409718628E-13 1.100256884657 1.493844174923E-13 1.000421704815E-14 .01446906464129
948.7966183757 3.689655191808E-13 3.622051963719E-13 .5281561353543 8.463934776334E-14 3.942946427645E-13 .5747284269753
891.0552315218 1.136287212214E-13 3.35166936478E-13 .4892824792885 6.1269274379E-14 3.652892633779E-13 .5325656897777
945.0039368762 7.568347958359E-14 3.473472785727E-13 .5078476296842 1.16307008665E-13 3.8013266445E-13 .5543020722239
58.08914986048 2.54321590299E-14 1.074007945658E-15 .001495129189284 4.415921761349E-15 1.002733800878E-15 .001396135924215
466.2156546448 8.204228522556E-15 1.402810272404E-13 .2000429483011 2.05360031435E-14 1.621190136574E-13 .2313015374461
411.1090306182 2.448001333632E-13 1.105312736357E-13 .1517077513601 1.030183189992E-12 1.083623339135E-13 .1481904353987
947.5855920437 1.798036798394E-13 2.436920478168E-13 .3387739176301 2.003246189888E-14 2.534731907751E-13 .3524411661016
342.04977348818 1.893325490843E-13 4.157459857362E-14 .05979025618695 5.413847476576E-14 4.104635367018E-14 .05893235992261
177.3172492521 3.58633753564E-14 1.615534297024E-14 .02305574355413 2.117754560571E-14 1.590193967862E-14 .02268850440328
16.96674315316 3.515305198962E-14 7.846634614255E-15 .01055662753274 6.397482412701E-14 5.601159248757E-15 .007523574164094
6.761501398746 3.182020872322E-14 9.862687798659E-15 .01315522705729 2.710572373872E-14 7.518432936087E-15 .01002443043758
886.8706876552 2.604384791305E-13 3.030065296525E-13 .4041769721555 1.347917032046E-13 2.046591992324E-13 .2736436687276
598.7899310071 7.412085363515E-13 5.323352219108E-14 .06895590503932 3.055973804003E-12 6.408696583549E-14 .08277614893901
347.1288244368 3.610881151686E-13 4.901658103776E-14 .06140081173035 1.36542538402E-13 3.287078628991E-14 .04120788691427
532.4459867559 7.467847459004E-13 1.869820756110E-13 .2365993935846 6.246449731907E-13 1.191896783844E-13 .1508867429844
393.1390918195 5.119346669296E-13 1.544316098556E-13 .1953791522891 9.254701393468E-13 9.662626257808E-14 .1233486930921

Figure B-2. Printer image of the contents of the file NEWFIL created by READATA at line 65 of the program in Figure B-1.

APPENDIX C

EXAMPLE OF ACQUIRING DATA BY METHOD II

Figure C-1 and C-2 is the source listing of program QRATIO and its output which we used to determine how well we have calibrated the Lyman- α . Figure C-3 is a program which we used to see how closely the intensity PDF's match the theoretical distribution of intensity. Figure C-4 is a plot from the program of Fig. C-3.

```

1  PROGRAM ORATIO(ANS,INPUT,OUTPUT,TAPE1=ANS,TAPE5=INPUT,
2  . TAPE6=OUTPUT)
3
4  CHARACTER*10 ITEMS(5)
5  REAL RECORD(500)
6  INTEGER WEAT(8),CNZR(8),SESS(8),ZOV(8),FREQ(8),TAPE(100),ISTA(8)
7  INTEGER IDARRAY(300)
8  INTEGER LOCATN(5),MASTER(801),NSIZES(5)
9  COMMON/DESCRIP/HEADER(20)
10 COMMON/DESCRIP/INDEX(50),NSHIFT(50),MASKV(50),SYMBOL(50)
11 COMMON/DESCRIP/IDCTRY(3000)
12 DATA WEAT,SESS,ZOV,FREQ,TAPE,ISTA,MWEA,NSES,NZOR,NFRE,NTAP,NCNZ,
13 . CNZR,NISTA /155*0/
14
15 CALL OPENDB(1,MASTER,601,HEADER,3220)
16 WEAT(1) = 1
17 MWEA = 1
18 CALL IDS(WEAT,MWEA,SESS,NSES,ZOV,NZOR,FREQ,NFRE,TAPE,NTAP,CNZR,
19 . NCNZ,ISTA,NISTA,MASTER,601, IDARRAY,NMID)
20 PRINT *, 'THE NO. OF CLEAR AIR TAPE ENTRIES IS ',NMID
21 DO 100 I=1,5
22   NSIZES(I) = 0
23   LOCATN(I) = 0
24   ITEMS(I) = ' '
25   ITEMS(1) = 'Q1AV'
26   ITEMS(2) = 'RHOC1'
27   ITEMS(3) = 'Q2AV'
28   ITEMS(4) = 'RHOC2'
29   ITEMS(5) = 'RUMID'
30 NITEMS=5
31 CALL GETVAR(ITEMS,NITEMS,LOCATN,NSIZES)
32 CALL GETID(1,MASTER,601, ID)
33
34 C      LOOP THRU NMID RECORDS OF VALUES
35
36 DO 300 IDID = 1,NMID
37   CALL READDB(1,RECORD,500, IDARRAY(IDID))
38   CALL GETVAL(RECORD,500,LOCATN(1),NSIZES(1), Q1AV)
39   CALL GETVAL(RECORD,500,LOCATN(2),NSIZES(2), RHOC1)
40   CALL GETVAL(RECORD,500,LOCATN(3),NSIZES(3), Q2AV)
41   CALL GETVAL(RECORD,500,LOCATN(4),NSIZES(4), RHOC2)
42   CALL GETVAL(RECORD,500,LOCATN(5),NSIZES(5), IDRUN)
43   RATIO1 = RHOC1/Q1AV
44   RATIO2 = RHOC2/Q2AV
45   WRITE(6,998) IDRUN
46   WRITE(6,999) 1,RHOC1,Q1AV,RATIO1
47   WRITE(6,999) 2,RHOC2,Q2AV,RATIO2
48 CONTINUE
49 FORMAT(' FROM TAPE ',A10)
50 FORMAT(' FROM STATION ',I1,' Q-PSYCH,Q-LYMAN A, PSYC/LYA = ',
51 . 3F10.5)
52 CALL CLOSEDB(1)
53 END

```

Figure C-1. FORTRAN-'77 source listing of a program to validate the MET stations Lyman- α hygrometer data.

THE NO. OF CLEAR AIR TAPE ENTRIES IS 21
 ALL VARIABLES REQUESTED WERE FOUND

FROM TAPE *S4 T9			
FROM STATION 1 Q-PSYCH,Q-LYMAN A, PSYC/LYA =	11.91510	12.74966	.93454
FROM STATION 2 Q-PSYCH,Q-LYMAN A, PSYC/LYA =	11.53722	12.94938	.89095
FROM TAPE *S4 T25			
FROM STATION 1 Q-PSYCH,Q-LYMAN A, PSYC/LYA =	9.91492	9.79565	1.01218
FROM STATION 2 Q-PSYCH,Q-LYMAN A, PSYC/LYA =	9.61510	9.76911	.98424
FROM TAPE *S4 T3			
FROM STATION 1 Q-PSYCH,Q-LYMAN A, PSYC/LYA =	10.08415	10.10029	.99840
FROM STATION 2 Q-PSYCH,Q-LYMAN A, PSYC/LYA =	9.82749	10.19999	.96348
FROM TAPE *S4 T4			
FROM STATION 1 Q-PSYCH,Q-LYMAN A, PSYC/LYA =	10.43429	10.40422	1.00289
FROM STATION 2 Q-PSYCH,Q-LYMAN A, PSYC/LYA =	10.04083	10.69850	.93853
FROM TAPE *S4 T9			
FROM STATION 1 Q-PSYCH,Q-LYMAN A, PSYC/LYA =	11.91510	12.39897	.96097
FROM STATION 2 Q-PSYCH,Q-LYMAN A, PSYC/LYA =	11.53722	12.74030	.90557
FROM TAPE *S4 T16			
FROM STATION 1 Q-PSYCH,Q-LYMAN A, PSYC/LYA =	13.22113	13.21760	1.00027
FROM STATION 2 Q-PSYCH,Q-LYMAN A, PSYC/LYA =	12.71640	13.17422	.96525
FROM TAPE *S4 T16			
FROM STATION 1 Q-PSYCH,Q-LYMAN A, PSYC/LYA =	12.55008	12.54014	1.00079
FROM STATION 2 Q-PSYCH,Q-LYMAN A, PSYC/LYA =	12.19556	12.67743	.96199
FROM TAPE *S4 T16			
FROM STATION 1 Q-PSYCH,Q-LYMAN A, PSYC/LYA =	12.51995	12.43589	1.00676
FROM STATION 2 Q-PSYCH,Q-LYMAN A, PSYC/LYA =	12.41343	12.82425	.96797
FROM TAPE *S4 T18			
FROM STATION 1 Q-PSYCH,Q-LYMAN A, PSYC/LYA =	12.89936	12.91992	.99841
FROM STATION 2 Q-PSYCH,Q-LYMAN A, PSYC/LYA =	12.56615	13.05664	.96243
FROM TAPE *S4 T22			
FROM STATION 1 Q-PSYCH,Q-LYMAN A, PSYC/LYA =	10.27393	10.26783	1.00059
FROM STATION 2 Q-PSYCH,Q-LYMAN A, PSYC/LYA =	9.98448	10.29055	.97026
FROM TAPE *S4 T23			
FROM STATION 1 Q-PSYCH,Q-LYMAN A, PSYC/LYA =	12.07097	12.07119	.99998
FROM STATION 2 Q-PSYCH,Q-LYMAN A, PSYC/LYA =	11.63918	11.88928	.97896
FROM TAPE *S4 T23			
FROM STATION 1 Q-PSYCH,Q-LYMAN A, PSYC/LYA =	12.14681	12.10343	1.00358
FROM STATION 2 Q-PSYCH,Q-LYMAN A, PSYC/LYA =	11.86800	12.07404	.98294
FROM TAPE *S4 T26			
FROM STATION 1 Q-PSYCH,Q-LYMAN A, PSYC/LYA =	10.28450	10.28912	.99955
FROM STATION 2 Q-PSYCH,Q-LYMAN A, PSYC/LYA =	9.75101	10.29356	.94729
FROM TAPE *S4 T26			
FROM STATION 1 Q-PSYCH,Q-LYMAN A, PSYC/LYA =	10.21738	10.31783	.99026
FROM STATION 2 Q-PSYCH,Q-LYMAN A, PSYC/LYA =	9.90139	10.54962	.93855
FROM TAPE *S4 T46			
FROM STATION 1 Q-PSYCH,Q-LYMAN A, PSYC/LYA =	11.83544	11.85860	.99805
FROM STATION 2 Q-PSYCH,Q-LYMAN A, PSYC/LYA =	11.60790	11.87200	.97775
FROM TAPE *S4 T46			
FROM STATION 1 Q-PSYCH,Q-LYMAN A, PSYC/LYA =	12.20823	12.28132	.99405
FROM STATION 2 Q-PSYCH,Q-LYMAN A, PSYC/LYA =	11.92418	12.26805	.97197
FROM TAPE *S4 T47			
FROM STATION 1 Q-PSYCH,Q-LYMAN A, PSYC/LYA =	9.58335	9.59166	.99913
FROM STATION 2 Q-PSYCH,Q-LYMAN A, PSYC/LYA =	9.30255	9.57059	.97199
FROM TAPE *S4 T31			
FROM STATION 1 Q-PSYCH,Q-LYMAN A, PSYC/LYA =	17.14909	17.12146	1.00161
FROM STATION 2 Q-PSYCH,Q-LYMAN A, PSYC/LYA =	17.14756	17.22267	.99564
FROM TAPE *S4 T59			
FROM STATION 1 Q-PSYCH,Q-LYMAN A, PSYC/LYA =	9.88226	9.89075	.99914
FROM STATION 2 Q-PSYCH,Q-LYMAN A, PSYC/LYA =	9.61503	9.89534	.97167

Figure C-2. Copy of printer output from the program listing of Figure C-1.

PROGRAM PLT 74/835 OPT=0, ROUND= A/ S/ M/-D.-DS FTN 5.1+628 86/07/22. 16.58.02 PAGE 1
DO=LONG/-OT, ARG=COMMON/-FIXED, CS= USER/-FIXED, DB=TB/-SB/-SL/ ER/-ID/-PMD/-ST, -AL, PL=5000
FINS, I=PLT1, L=00, LO, B=0.

```

1 PROGRAM PLT(ANSWERS, INPUT, OUTPUT, TAPE1=ANSWERS,
2   TAPE5=INPUT, TAPE6=OUTPUT)
3
4   INTEGER SESN, TPE
5
6   SESN = 4
7   TPE = 25
8   ISTAT = 0
9   CALL PLTPDF(1, SESN, TPE, ISTAT)
10  END

```

---VARIABLE MAP---(LO=A/R)
---NAME---ADDRESS---BLOCK---PROPERTIES---TYPE---SIZE---REFERENCES---
A=ARGLIST, C=CTRL OF DO, I=DATA INIT,
R=READ, S=STORE, U=I/O UNIT, W=WRITE

NAME	ADDRESS	BLOCK	PROPERTIES	TYPE	SIZE	REFERENCES
ISTAT	278			INTEGER	8/S	9/A
SESN	258			INTEGER	4	6/S
TPE	268			INTEGER	4	7/S

---PROCEDURES---(LO=A/R)
---NAME---TYPE---ARGS---CLASS---REFERENCES---
D=DEF LINE OF STMT FUNC
A=ACTUAL ARGUMENT

NAME	TYPE	ARGS	CLASS	REFERENCES
PLTPDF	4		SUBROUTINE	9

---ENTRY POINTS---(LO=A/R)
---NAME---ADDRESS---ARGS---REFERENCES---
D=DEFINITION, R=RETURN

NAME	ADDRESS	ARGS	REFERENCES
PLT	0B	0	1/D

---STATISTICS---

PROGRAM-UNIT LENGTH	308	= 24
CM STORAGE USED	627808	= 26048
COMPILE TIME	0.019	SECONDS

Figure C-3. FORTRAN-'77 source listing of a program to validate the mm-wave probability density functions.

```

1 C
2 C
3 SUBROUTINE PLTPOF (LUNIT,SESN,TPE,ISTAT)
4 C
5 C WRITTEN BY MARK WICKERS JULY 1 1986
6 C
7 C THIS SUBROUTINE WILL PLOT THE INTENSITY POFs VS THE GAUSSIAN
8 C CURVE.
9 C
10 C
11 C VARIABLES NEEDED TO ACCESS THE DATA BASE
12 C
13 CHARACTER*10 VARRAY(10)
14 INTEGER LOCATN(10), NSIZES(10), RECID(300), SESN, TPE
15 REAL DATA(30499)
16 C
17 C VARIABLES NEEDED TO GRAPH THE POFs
18 C
19 C HORLINS = NUMBER OF LINES IN THE HEADER OF GRAPH
20 C HORSZ = SIZE OF THE LETTERS IN THE HEADER
21 C IMARK = IS NEGATIVE TO NOT HAVE POINTS CONNECTED
22 C
23 CHARACTER*1 CHAR
24 CHARACTER*81 XNAM,YNAM
25 DIMENSION PTITL(40)
26 DIMENSION IPAK(400)
27 INTEGER NROWS(20),HORLINS
28 REAL X(2),Y(2),G(50),SCALE(50),LN(50)
29 C
30 C VARIABLES DESIRED FROM THE DATA BASE
31 C
32 REAL NBIN
33 REAL BMIN(4),BMAX(4),IAV(4),IVAR(4)
34 REAL IPOF(50,4)
35 REAL TNAME,TIME1(10),TIME2(10)
36 DIMENSION VANIPOF(50)
37 C
38 C VARRAY CONTAINS THE VARIABLES WE DESIRE TO EXTRACT FROM THE
39 C DATA BASE. NITEMS EQUALS THE NUMBER OF VARIABLES IN VARRAY.
40 C
41 DATA VARRAY/'NBININTEN','BINMININT','BINMAXINT',
42 * 'INTNSTYAV','INTNSTYVAR','IIPDF','I2PDF','I3PDF',
43 * 'I4PDF','TNAME','TIME1','TIME2','VANEIPOFNM','VANEIPOFAK',
44 * 'VANE2PDFNM','VANE2PDFAK'/'
45 C
46 DATA NITEMS/16/
47 DATA LOCATN/10*0/,NSIZES/10*0/,RECID/300*0/
48 C
49 C ACCESSING THE DATA BASE
50 C
51 C FIRST OPEN THE DATA BASE
52 C
53 CALL OPEND8(LUNIT)
54 C
55 C RETRIEVE THE DATA BASE RECORD IDENTIFIER THAT IS SPECIFIED BY SESN

```

Figure C-3. (continued).

```

56 C TPE AND ISTAT. IN THIS SPECIAL CASE THERE WILL BE ONLY ONE RECORD
57 C IDENTIFIER RETURNED. USUALLY RECID WILL BE RETURNED AS AN ARRAY
58 C OF IDENTIFIERS AND NUMID EQUAL TO THE NUMBER OF IDENTIFIERS FOUND
59 C AND STORED IN RECID.
60
61 CALL IDS(0.0,SESN,1.0,0.0,0.0,TPE,1.0,0.0,ISTAT,1, RECID,NUMID)
62
63 NOW THAT WE KNOW WHAT RECORD IN THE DATA BASE CONTAINS THE DATA
64 C FOR OUR VARIABLES IN VARRAY, WE MUST EXTRACT THIS DATA BY FIRST
65 C GETTING ALL THE VARIABLES' LOCATIONS AND SIZES WITHIN THIS RECORD.
66 C WE LOOK UP THIS INFORMATION IN THE DICTIONARY BY CALLING SUBROUTINE
67 C GETVAR.
68
69 CALL GETVAR(VARRAY,NITEMS, LOCATN,NSIZES)
70
71 THE TOTAL SIZE OF EACH DATA BASE RECORD IS 38499 WORDS. HOWEVER,
72 C WE NEED ONLY THE PORTION OF THE RECORD THAT INCLUDES THE LAST
73 C VARIABLE IN OUR VARRAY (BY LAST VARIABLE WE MEAN THE VARIABLE WITH
74 C THE FARTHEST LOCATION FROM THE BEGINNING OF THE RECORD). ALSO, IT
75 C IS FASTER TO READ A MULTIPLE OF 64 WORDS FROM THE RECORD. TO FIND
76 C OUT THE MOST EFFICIENT SIZE DATA BLOCK TO READ FROM THE DATA BASE
77 C RECORD, WE CALL SUBROUTINE INSRTR (INSRTR = INTEGER FUNCTION WHAT
78 C SIZE RECORD TO READ).
79
80 IRECL = INSRTR(NITEMS,NSIZES,LOCATN)
81
82 NOW WE READ THE MOST EFFICIENT SIZE OF THE DATA BASE RECORD INTO
83 C LOCAL MEMORY BY CALLING SUBROUTINE READDB.
84
85 CALL READDB(LUNIT,DATA,IRECL,RECID(1))
86
87 FROM THIS RECORD OF DATA WE HAVE TO EXTRACT THE VALUES OF OUR
88 C VARIABLES VIA THE INFORMATION OBTAINED FROM THE DICTIONARY.
89
90 CALL GETVAL(DATA,IRECL,LOCATN(1),NSIZES(1), NBIN)
91 CALL GETVAL(DATA,IRECL,LOCATN(2),NSIZES(2), BMIN)
92 CALL GETVAL(DATA,IRECL,LOCATN(3),NSIZES(3), BMAX)
93 CALL GETVAL(DATA,IRECL,LOCATN(4),NSIZES(4), IAV)
94 CALL GETVAL(DATA,IRECL,LOCATN(5),NSIZES(5), IVAR)
95 CALL GETVAL(DATA,IRECL,LOCATN(6),NSIZES(6), IPDF(1,1))
96 CALL GETVAL(DATA,IRECL,LOCATN(7),NSIZES(7), IPDF(1,2))
97 CALL GETVAL(DATA,IRECL,LOCATN(8),NSIZES(8), IPDF(1,3))
98 CALL GETVAL(DATA,IRECL,LOCATN(9),NSIZES(9), IPDF(1,4))
99 CALL GETVAL(DATA,IRECL,LOCATN(10),NSIZES(10), TNAME)
100 CALL GETVAL(DATA,IRECL,LOCATN(11),NSIZES(11), TIME1)
101 CALL GETVAL(DATA,IRECL,LOCATN(12),NSIZES(12), TIME2)
102 CALL GETVAL(DATA,IRECL,LOCATN(13),NSIZES(13), VANIMM)
103 CALL GETVAL(DATA,IRECL,LOCATN(14),NSIZES(14), VANIMX)
104 CALL GETVAL(DATA,IRECL,LOCATN(15),NSIZES(15), VAN2MM)
105 CALL GETVAL(DATA,IRECL,LOCATN(16),NSIZES(16), VAN2MX)
106
107 C CLOSE DATA BASE
108
109 CALL CLOSED8(LUNIT)
110
111 C USE THE DATA OBTAINED FROM THE DATA BASE TO PLOT THE PDFS
112

```

Figure C-3. (continued).

```

113 ENCODE(4B,10,PTITL) TNAME, TIME1(1), TIME2(1)
114 FORMAT('PDF TAPEID ',A10,' T1 = ',F7.2,' T2 = ',F7.2,' $')
115
116 C OPEN DISPLA VERSION 9.0 GRAPHICS
117 CALL COMPRS
118
119 DO 1000 IP = 1.4
120
121 SUM = 0.0
122 DO 3 I=1,50
123 SUM = SUM + IPDF(I,IP)
124
125 XMIN = BMIN(IP)
126 XMAX = BMAX(IP)
127 YMIN = 0.0
128 YLENGTH = 10.0
129 YLENGTH = 7.0
130
131 C CALCULATE THE INCREMENTS FOR THE X AXIS
132 DELTA = (BMAX(IP) - BMIN(IP))/NBIN
133 SUM = SUM * DELTA
134 PRINT *, 'INTEGRATION UNDER PDF', IP, ' IS = ', SUM
135
136 C THE PDF NEEDS TO BE NORMALIZED. THIS IS DONE BY CALCULATING A
137 C ROUGH AREA UNDER ITS CURVE AND DIVIDING ONE BY THIS SUM. THEN
138 C ALL PDF VALUES ARE MULTIPLIED BY THIS NORMALIZING FACTER.
139
140 RNORM = 1/SUM
141 DO 40 I=1,50
142 IPDF(I,IP) = IPDF(I,IP) * RNORM
143 TMEAN = 0.0
144
145 DO 50 J=1,50
146 SCALE(J) = BMIN(IP) + (DELTA*(FLOAT(J) - 0.5))
147 TMEAN = TMEAN + (SCALE(J) * IPDF(J,IP))
148 CONTINUE
149
150 TMEAN = TMEAN * DELTA
151 PRINT *, 'TMEAN = ', TMEAN
152
153 C CALCULATE THE GAUSSIAN CURVE
154 C
155 C = (2*3.1415927*IVAR(IP))**(-0.5)
156 DO 100 J=1,50
157 POWER = -(((SCALE(J)+((1/2)*DELTA))-1)**2)/(2*IVAR(IP))
158 G(J) = C*EXP(POWER)
159
160 C CALCULATE THE LOGNORMAL CURVE
161 C
162 C
163
164
165
166
167
168
169

```

Figure C-3. (continued).

```

170 C
171 C1 = SORT(2*J, 1415927+IVAR(IP))
172 DO 150 J=1,50
173 C2=C1*(SCALE(J) + (1/2)*DELTA)
174 C3=(LOG(SCALE(J) + 1/2*DELTA)+IVAR(IP)/2)**2
175 LN(J) = EXP(C3)/C2
176 CONTINUE
177
178
179 C
180 C
181 C
182
183
184
185
186
187
188
189
190
191
192
193
194
195
196
197
198
199
200
201
202
203
204
205
206
207
208
209
210
211
212
213
214
215
216
217
218
219
220
221
222
223
224
225
226

```

C1 = SORT(2*J, 1415927+IVAR(IP))
 DO 150 J=1,50
 C2=C1*(SCALE(J) + (1/2)*DELTA)
 C3=(LOG(SCALE(J) + 1/2*DELTA)+IVAR(IP)/2)**2
 LN(J) = EXP(C3)/C2
 CONTINUE

 CALCULATE YMAX FROM THE GAUSSIAN CURVE

 YMAX = 0.0
 DO 200 I=1,50
 IF (G(I).GT.YMAX) YMAX=G(I)
 IF (IPDF(I,IP).GT.YMAX) YMAX=IPDF(I,IP)
 IF (LN(I).GT.YMAX) YMAX=LN(I)
 CONTINUE

 HORLINS = 1
 HORSZ = 1.2
 IMARK = -1

 CALL HEIGHT(.25)

 IF (IP.EQ.1) CHAR = '1'
 IF (IP.EQ.2) CHAR = '2'
 IF (IP.EQ.3) CHAR = '3'
 IF (IP.EQ.4) CHAR = '4'
 XNAM = 'NORMALIZED INTENSITY FOR ANTENNA '//CHAR//'
 YNAM = 'INTENSITY PDF\$'
 CALL PAGE(14,11,1)

 LENG = LINEST(IPAK,400,10)
 CALL LINES('GAUSSIANS',IPAK,1)
 CALL LINES('LOGNORMAL\$',IPAK,2)

 CALL AREA2D(XLENGTH,YLENGTH)
 CALL PHYSOR(1,25,1,25)
 CALL RESET('MARKER')
 CALL XNAME(XNAM,100)
 CALL YNAME(YNAM,100)
 CALL HEADIN(PTITL,100,HORSZ,HORLINS)
 CALL PSCALE(YMAX,YMIN,YSTEP,NTIKX,XLENGTH)
 CALL PSCALE(XMAX,XMIN,XSTEP,NTIKY,YLENGTH)
 CALL GRAF(XMIN,XSTEP,XMAX,YMIN,YSTEP,YMAX)

 Y(1) = 0.0
 DO 500 J=1,50
 X(1) = X(2) = SCALE(J)
 Y(2) = IPDF(J,IP)
 CALL CURVE(X,Y,2,0)

Figure C-3. (continued).

SUBROUTINE PLIPDF	74/835	OPT=0,ROUND= A/ S/ M/-D,-DS	FTN 5.1+628	86/07/22. 16.58.02	PAGE 5
-------------------	--------	-----------------------------	-------------	--------------------	--------


```

227
228
229
230
231
232
233
234
235
236
237
238
239
240
241
242
243

```

```

550
DO 550 I=1,50
  SCALE(I) = SCALE(1) + ((1/2) * DELTA)
  CALL MARKER(0)
  CALL CURVE(SCALE,G,49,-1)
  CALL MARKER(2)
  CALL CURVE(SCALE,LN,49,-1)
  CALL LEGEND(IPAK,2,9,0,2,0)

1000 CALL ENDPL(0)
      CONTINUE
      CALL DONEPL
      END

```

Figure C-3. (continued).

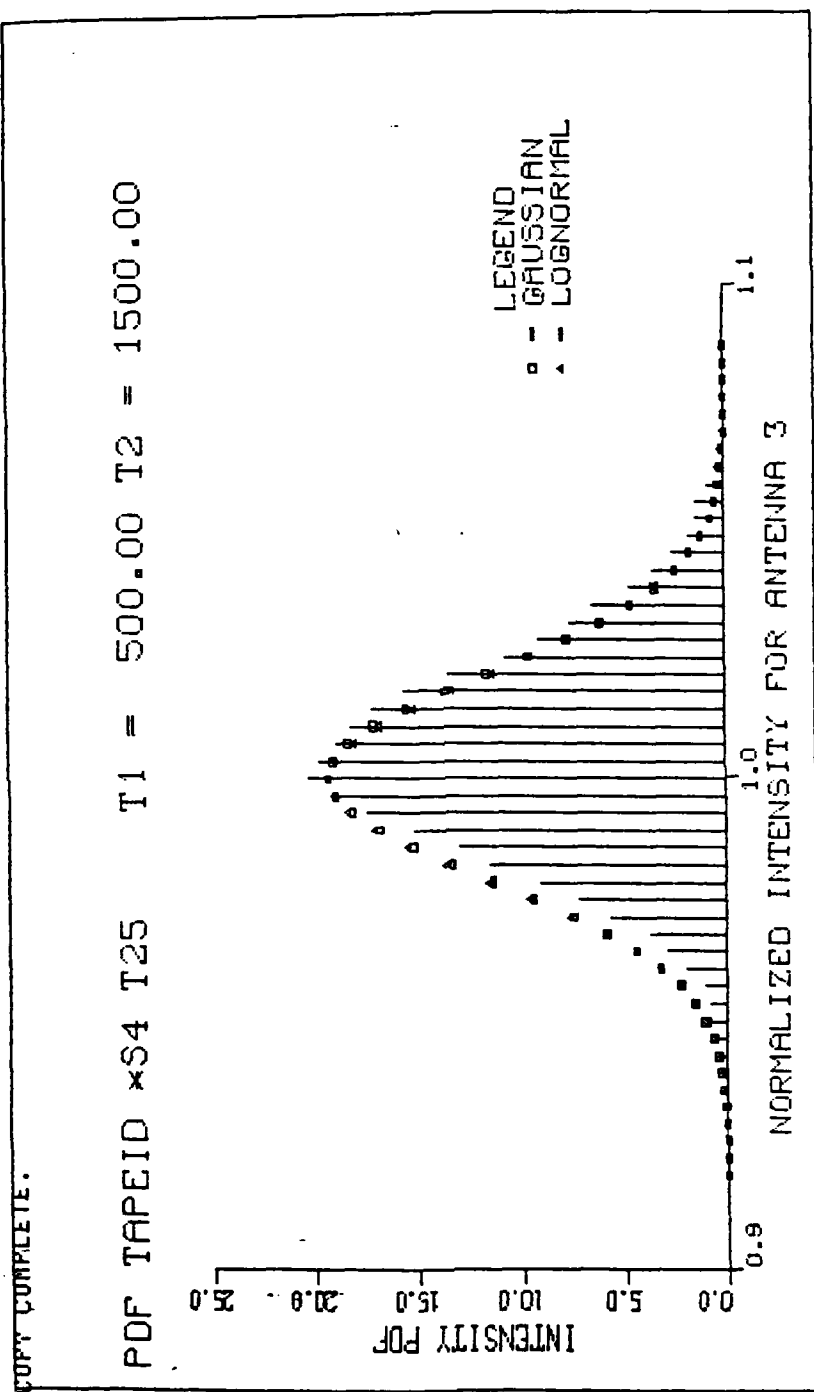


Figure C-4. One of the plots output from the program of Figure C-3.

III. LIST OF PUBLICATIONS ON THE NOAA/GIT RESEARCH PROJECT

1. McMillan, R.W., R.A. Bohlander, and G.R. Ochs (1981): Instrumentation for millimeter wave turbulence measurements. Atmospheric Effects on Electro-Optical, Infrared, and Millimeter Wave on Systems Performance, August 27-78, 1981, San Diego, CA SPIE, vol, 305, 253-260. (Georgia Institute of Technology, ARO Contract Number 55-81).
2. Kohsiek, W. (1982): Optical and in situ measuring of structure parameters relevant to temperature and humidity, and their application to the measuring of sensible and latent heat flux. NOAA Tech. Memo ERL WPL-96.
3. McMillan, R.W., R.A. Bohlander, D.G. Bauerle, G.R. Ochs, R.J. Hill, S.F. Clifford, and J. Nemanich (1982): Millimeter wave atmospheric turbulence measurements: Preliminary results. SPIE, vol. 337, 88-95 Millimeter Wave Technology, 6-7 May 1982, Arlington, Virginia, (U.S. Army Contract DAAG29-18-K-0173). Georgia Institute of Technology, ARO Contract DAAG29-81-K-0173.
4. Kohsiek, W. (1982): Measuring of CT-squared, CQ-squared and CTQ-squared in the unstable surface layer and their relations to the vertical fluxes of heat and moisture. Boundary Layer Meteorol., vol. 24, 89-107.
5. McMillan, R.W., R.A. Bohlander, G.R. Ochs, R.J. Hill, and S.F. Clifford (1983): Millimeter wave atmospheric turbulence measurements: Preliminary results and instrumentation for future measurements. Optical Engineering, vol. 22, no. 1, 032-039. Georgia Institute of Technology, (ARO Contracts DAAG29-81-K-0173 and DAAG29-77-C-0026).
6. Priestley, J.T. and W.D. Cartwright (1982): Frequency response measurements on Lyman-alpha humidimeters. NOAA Tech. Memo ERL WPL-92.
7. Priestley, J.T., and R.J. Hill (1985): Measuring high-frequency humidity, temperature, and radio refractive index in the surface layer. J. Atmos. Oceanic Tech., vol. 2, no. 2, 233-251.
8. Hill, R.J., R.S. Lawrence and J.T. Priestley (1982): Theoretical and calculational aspects of the radio refractive index of water vapor. Radio Sci., vol. 17, no. 5, 1251-1257.
9. Lataitis, R.J. (1982): Statistics of electromagnetic wave propagation through a turbulent atmosphere. Master's Thesis, Univ. of Colorado.
10. Hill, R.J. and G.R. Ochs (1983): Surface-layer micrometeorology by optical scintillation techniques. Digest of the Topical Meeting on Optical Techniques for Remote Probing of the Atmosphere. January 10-12, 1983, Lake Tahoe, NV., OSA, TuC16-1 thru TuC16-4.
11. Bohlander, R.A., R.W. McMillan, V.T. Brady, G.F. Kirkman, M.J. Sinclair, J.W. Larsen, M.L. Blyler, R.P. Lilly, D.O. Gallentine, S.F. Clifford, J.T. Priestley, R.J. Hill, R.E. Cupp, N.L. Abshire, R.B. Fritz, W. Cartwright, G.R. Ochs, R.J. Lataitis, J.J. Wilson, and G.M. Walford (1983):

Observations of amplitude and angle of arrival scintillation in millimeter wave propagation caused by turbulence in clear air near the ground. Proc. of 8th Int'l Conf. on Infrared and Millimeter Waves, 12-17 December 1983, Miami Beach, FL, TH6.4.

12. McMillan, R.W., R.A. Bohlander, D.M. Guillory, R.H. Platt, J.M. Cotton, Jr., S.F. Clifford, J.T. Priestley, and R. J. Hill (1984): Millimeter wave atmospheric turbulence measurements. Presented at the Annual Review Conference on Atmospheric Transmission Models, at Air Force Geophysics Laboratory, Hanscom AFB, MA, May, 1984.
13. Bohlander, R.A., R.W. McMillan, D.M. Guillory, R.H. Platt, S.F. Clifford, J.T. Priestley, R.J. Hill, R. Olsen, and B. Rischel (1984): Millimeter wave transmission fluctuations due to snow. Proc. of the SNOW Symposium IV, Hanover, NH, August 1984. Engineering Laboratory in Hanover, NH, August 1984.
14. McMillan, R.W., R.A. Bohlander, D.M. Guillory, R.H. Platt, J.M. Cotton, Jr., S.F. Clifford, J.T. Priestley, and R.J. Hill (1984): Millimeter wave atmospheric turbulence measurements. Proc. 9th Intl. Conf. on Infrared and Millimeter Waves, Osaka (Takarazuka), Japan, October 1984, 463-464.
15. McMillan, R.W., R.A. Bohlander, R.H. Platt, D.M. Guillory, J.T. Priestley, R.J. Hill, S.F. Clifford, R.E. Cupp, and J. Wilson (1985): Atmospheric turbulence measurement system. SPIE Tech. Symp. East '85, Arlington, VA 8-12 April 1985, Arlington, VA.
16. Bohlander, R.A., R.W. McMillan, D.M. Guillory, R.J. Hill, J.T. Priestley, S.F. Clifford, and R. Olsen (1986): Fluctuations in millimeter wave signals. Conference Digest of the tenth International conference on Infrared and Millimeter Waves, 9-13 December 1985, Lake Buena Vista, FL.
17. Clifford, S.F., and R.J. Lataitis (1985): Mutual coherence function for line-of-sight microwave propagation through atmospheric turbulence. Radio Sci., vol. 20, no. 2, 221-227.
18. Hill, R.J. (1985): Atmospheric refraction and absorption and their fluctuations for centimeter and millimeter waves. 10th Int'l Conference on Infrared and Millimeter Waves. 9-12 December, 1985, Kissimmee, FL.
19. Hill, R.J. (1986): Absorption by the tails of the oxygen microwave resonances at atmospheric pressures. (IEEE Trans on Antennas and Propagation).
20. Hill, R.J. (1986): Water-vapor-absorption line-shape comparison using the 22 GHz line: The Van Vleck-Weisskopf shape affirmed. Radio Sci., Vol. 21, 447-451.
21. Hill, R.J., W.P. Schoenfeld, J.P. Riley, J.T. Priestley, S.F. Clifford, S.P. Eckes, R.A. Bohlander, and R.W. McMillan (1985): Data analysis of the NOAA/GIT millimeter wave propagation experiment near Flatville, Illinois. NOAA Tech. Rep., ERL 429-WPL60.
22. Hill, R.J., J.T. Priestley, S.F. Clifford, W.P. Schoenfeld, R.W. McMillan and R.A. Bohlander (1986): Instrumentation, data validation and analysis,

- and results of the NOAA-GIT millimeter-wave propagation experiment. Proc. of U.R.S.I., July 28 - August 1, 1986, Durham, NH.
23. Schoenfeld, W.P. and R.J. Hill (1986): An algorithm for removal of extraneous large amplitude spikes from high-speed digital data.
 24. Schoenfeld, W.P., R.J. Hill, and J.T. Priestley (1986): Repairing of the mm-wave intensity and phase-differences data collected at Flatville, Illinois by applying software filters to the collected digital data.
 25. Schoenfeld, W.P., R.B. Fritz, R.J. Lataitis, J.T. Priestley, G.R. Ochs, and S.F. Clifford (1986): Retrieving rain rates from the optical rain gauges used at Flatville, Illinois on the NOAA/GIT mm-wave propagation experiment.
 26. Schoenfeld, W.P., R.J. Hill, M.T. Wickers, J.T. Priestley, S.F. Clifford, R.A. Bohlander, and R.W. McMillan (1986): The NOAA/GIT mm wave propagation experiment scientific data base user guide. NOAA Tech Memo ERL WPL.
 27. Clifford, S.F., R.J. Hill, and J.T. Priestley (1986): Phase and amplitude statistics for millimeter wave propagation in clear air. Proc. 1986 Int'l Workshop on Millimeter Waves, April 2-4, 1986, Rome, Italy.
 28. Clifford, S.F., R.J. Hill, J.T. Priestley, R.A. Bohlander, and R.W. McMillan (1986): The spectra of amplitude and phase difference fluctuations of millimeter waves propagating in clear air. Proc. of U.R.S.I., July 28-August 1, 1986, Durham, NH.
 29. Schwiesow, R.L., R.E. Cupp, and S.F. Clifford (1985): Phase difference power spectra in atmospheric propagation through rain at 10.6 micrometers. Appl. Opt., Vol. 24, 4516-4524.
 30. Fritz, R.B., R.J. Hill, W.P. Schoenfeld, and J.T. Priestley (1986): Evidence for oscillatory rain rate in a midwestern winter rain. (J. Atmos. Sci.)
 31. Patterson, E.M., R.A. Bohlander, R.W. McMillan, R.L. Mandock, R.J. Hill, J.T. Priestley, S.F. Clifford, B.E. Rishel, and R. Olsen (1986): Spectral density and distributions of intensity and phase of millimeter wave signals propagated through rain, fog, and snow. Proc. of U.R.S.I., July 28-August 1, 1986, Durham, NH.
 32. Patterson, E.M., R.L. Mandock, R.W. McMillan, R.A. Bohlander, R.J. Hill, J.T. Priestley, B.E. Rishel, and R. Olsen (1986): Correlation of the attenuation of millimeter wave signals with rain rate. Proc. of U.R.S.I., July 28-August 1, 1986, Durham, NH.
 33. Hill, R.J., S.F. Clifford, J.T. Priestley, R.A. Bohlander, and R.W. McMillan (1986): Millimeter-wave scintillation due to atmospheric surface-layer turbulence. Int'l Conf. on Optical and Millimeter Wave Propagation and Scattering in the Atmosphere. Florence, Italy, 27-30 May, 1986.
 34. Hill, R.J., R.A. Bohlander, J.T. Priestley, R.W. McMillan, and S.F. Clifford (1986): Millimeter-wave propagation experiment at Flatville, Illinois: Clear-air-turbulence-induced scintillation compared with micrometeorological measurements. (Int'l Journal of Infrared and Millimeter Waves).

IV. ACKNOWLEDGMENTS

Many people contributed to this experiment and we are grateful for their contributions.

Georgia Institute of Technology:

M.L. Blyler, R.A. Bohlander, V.T. Brady, J.M. Cotton, Jr., D.O. Gallentine, D.M. Guilory, G.F. Kirkman, J.W. Larsen, R.P. Lilly, R.L. Mandock, R.W. McMillan, A. McSweeney, J.M. Newton, E.M. Patterson, R.H. Platt, G.W. Rosenberg, O.A. Simpson, M.J. Sinclair.

NOAA-Wave Propagation Laboratory:

N.L. Abshire, W. Cartwright, S.F. Clifford, R.E. Cupp, T.J. Drey, S.P. Eckes, R.B. Fritz, R.J. Hill, R.J. Lataitis, G.R. Ochs, J.T. Priestley, D.S. Reynolds, J.P. Riley, W.P. Schoenfeld, B. Spaur, G.M. Walford, M. Wickers, J.J. Wilson.

Atmospheric Science Laboratory (White Sands)/New Mexico State University:

G. Alvarez, T. Chavez, A. Davis, R. Johnson, R. Okrasinski, R. Olsen, B.E. Rishel, J. Sculley, R. Valdez, K. Walker.

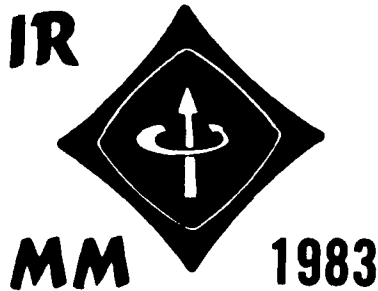
Aberdeen Proving Grounds:

D.G. Bauerle

Illinois Water Survey:

J. Vogel

V. APPENDICES



DECEMBER 12-17, 1983
DORAL HOTEL ON-THE-OCEAN
MIAMI BEACH, FLORIDA

CONFERENCE DIGEST

Richard J. Temkin
Editor

EIGHTH INTERNATIONAL CONFERENCE ON INFRARED AND MILLIMETER WAVES

Sponsored By
IEEE MICROWAVE THEORY AND TECHNIQUES SOCIETY
AND THE INTERNATIONAL UNION OF RADIO SCIENCE
WITH THE ASSISTANCE OF THE U.S. ARMY RESEARCH OFFICE

IEEE CATALOG NUMBER: 83CH1917-4

A Quasi-Optical Millimeter Wave Transmitter and Receiver Array for Measurements of Angular Scintillation

W6.4

R. A. Bohlander, V. T. Brady, A. McSweeney, G. P. Kirkman,
J. M. Newton, A. Davis, and O. A. Simpson*

Georgia Institute of Technology
Engineering Experiment Station
Atlanta, Georgia 30332

Abstract

This system, used to measure the effects of atmospheric turbulence at frequencies between 116 and 173 GHz, comprises a front-fed, off-axis parabola transmitting antenna located 1.4 km from a receiver array. The five antennas in the latter receive local oscillator power from a phase-locked klystron source via a low-loss lens beam waveguide distribution system.

Introduction

A key part in the Georgia Tech and National Oceanic and Atmospheric Administration study of millimeter wave atmospheric turbulence effects [1-3] has been the development of an appropriate antenna system. The equipment may be transported to sites of interest and has been used at a specially selected site [1] near Flatville, Illinois. The use of an array of receivers allows phase differences in the wavefront, and hence angle of arrival scintillation, to be measured. The method used is described elsewhere in these proceedings [1-2].

Transmitter

Three objectives met in the design of the transmitter antenna are: (1) it fills the receiver array for propagation distances of 1 km or more; (2) it avoids overfilling the receiver array and has minimal sidelobes; and (3) it gives far field conditions at the receiver. A picture of the design solution is shown in Fig. 1.

The primary antenna is an off-axis, rectangular (610 X 152 mm) section of a paraboloid reflector. As a result of the unequal height and width, the antenna pattern is spread out horizontally and is narrow vertically, efficiently filling the receiver array which is 1.5 m in vertical extent and 10 m in horizontal. The mirror was copy-turned from solid aluminum.

The primary is front fed by an E-plane corrugated rectangular horn, without obscuration. The corrugations have been included to minimize sidelobes in the feed pattern, and further reduction is effected by application of an absorbing foam to the periphery of the mirror.

As shown in Fig. 1, the antenna is mounted on a pedestal which goes through the floor of the surrounding van, down to a concrete pad which provides stability in pointing the antenna. The van and antenna have been sited on a berm such that the transmitter is at the same height above the plain as the receiver array (namely 3.5m).

Receiver Array

Each receiving antenna in the array comprises a conical corrugated horn feed, a 305 mm diameter polyethylene lens and a large, optical quality diagonal mirror for beam steering, as may be seen in Fig. 2. All are mounted on a large I-beam that rests on two pillars anchored to concrete ground pads for stability and isolation from the surrounding semi-trailer van.

The array may be termed non-redundant, since any combination of two antennas, gives a unique spacing for which the relative phases of the signals can be measured. The six intervals in the horizontal direction are 1.43, 2.86, 4.29, 5.71, 8.57 and 10 meters, intervals that are not only unique, but nearly uniformly distributed. Preliminary results [1] indicate transverse coherence lengths in the propagated radiation that are within the dimensions of the array. Thus the array size is well matched to the measurement requirement. One antenna shown in Fig. 2 is 1.43 m below the horizontal row of antennas. This allows differences in vertical and horizontal scintillation to be measured.

Lens Beam Waveguide LO Distribution

Provided that all receivers use the same LO, it is possible to measure meaningful phase differences. The mixers in the receivers are of the harmonic type so the LO frequencies are in the range 58 to 87 GHz. The LO sources are klystrons with available powers of a few hundred milliwatts. The waveguide size used for LO components throughout this range is WR-12.

The combination of the limited power available and the large array size over which the LO signal must be distributed makes it important to have high efficiency in the LO transmission medium. However, the losses in long runs of WR-12 waveguide may be shown to be too high.

*Present address: Emory University
Department of Physics Atlanta, Georgia 30322

Instead, a series of relay lenses, termed a lens beam waveguide [4], was chosen to distribute the LO signal, as illustrated in Fig. 3. Twenty-one lenses, 152 mm in diameter and made of high-density polyethylene were used, but the longest run between the klystron and a receiver involved fifteen. Corrugated conical horns couple the LO signal into and out of the beam waveguide and produce a beam with a Gaussian-shaped field profile [4].

The lenses have a curvature and spacing (737 mm) such that they are confocal [4]. The horn feeds were designed such that a beam waist occurs, for a frequency of 55 GHz, half way between the lenses as shown in Fig. 3. At a higher frequency, the feed pattern changes and the beam waist shifts, but at every odd numbered lens in a series, the beam returns to the size that couples efficiently to the output horns. Since all legs of the beam waveguide have an odd number of lenses, it works well over a wide frequency range.

The splitting of LO power between the paths to the various receivers is accomplished by stretched electroformed nickel meshes. Selections were made of meshes of different reflectance to balance the power to all receivers at crucial frequencies. It is calculated, from measured lens and mesh parameters that about ten percent of the klystron power launched into the beam waveguide is delivered to each receiver. Satisfactory mixer performance has been obtained with this system.

Conclusion

The first field tests, described elsewhere in these proceedings [1], have demonstrated the success of the designs presented in this paper. A notable achievement is the lens beam waveguide LO distribution system with its wide frequency range.

Acknowledgement: This work was supported by the U.S. Army Research Office under Contract DAAG29-81-R-0173. The assistance of our research collaborators at the National Oceanic and Atmospheric Administration is gratefully acknowledged.

References

- [1] R. A. Bohlander et al. and S. F. Clifford et al., these proceedings.
- [2] R. W. McMillan et al., these proceedings.
- [3] R.W.McMillan, R.A. Bohlander, G. R. Ochs, R. J. Hill, and S. F. Clifford, Optical Engineering 22, 32-39 (1983).
- [4] G. Goubau in *Millimetre and Submillimetre Waves*, P. A. Benson, ed., London: Iliffe Books (1969).

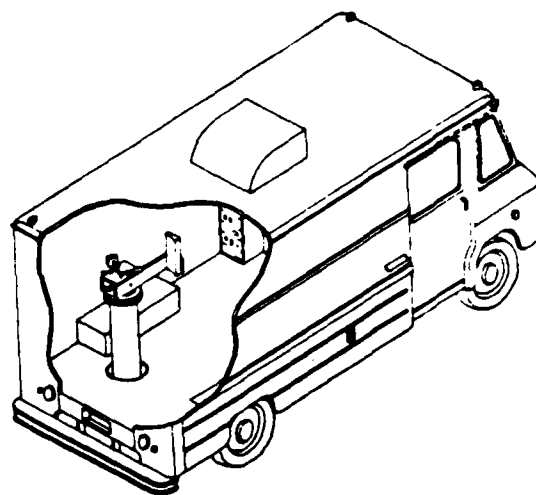


Fig. 1 Cutaway of transmitter van showing transmitting antenna mounted on a pedestal.

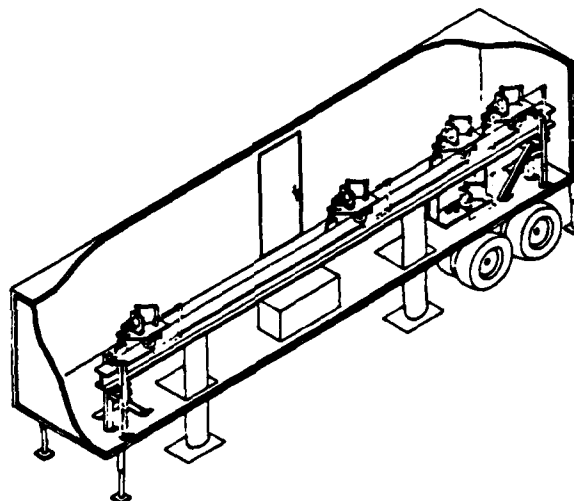


Fig. 2 Receiver array showing four antennas above the I-beam support and one below.

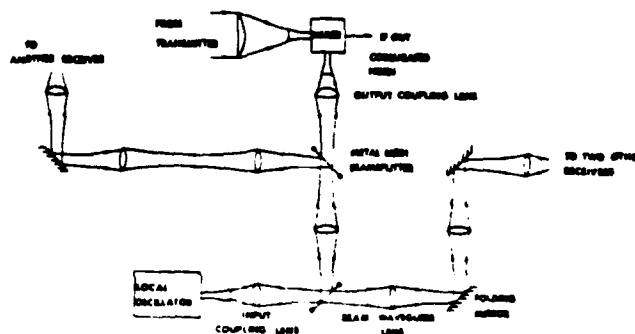


Fig. 3 A representative portion of the lens beam waveguide LO distribution system.

APPENDIX II

Radio Science, Volume 16, Number 1, pages 77-82, January-February 1981

Contribution of water vapor monomer resonances to fluctuations of refraction and absorption for submillimeter through centimeter wavelengths

R. J. Hill and S. F. Clifford

Wave Propagation Laboratory, Environmental Research Laboratories, National Oceanic and Atmospheric Administration, Boulder, Colorado 80303

(Received July 7, 1980; revised August 6, 1980; accepted August 6, 1980.)

Atmospheric fluctuations in temperature, humidity, and total pressure cause fluctuations in the absorption and refraction of electromagnetic waves. We consider only the absorption and refraction fluctuations caused by variations in the width and strength of water monomer resonances. We differentiate the absorption coefficient and refractive index with respect to temperature, humidity, and total pressure in order to obtain the coefficients that relate the fluctuations in absorption and refraction to these atmospheric parameters. The resulting coefficients as well as the absorption coefficient and the refractivity are calculated by summing over all water vapor infrared resonances and are displayed graphically. In the limit of low frequencies, these calculated coefficients are in good agreement with the formula for radio wave refractive index. The effects of turbulent fluctuations in total pressure are usually negligible.

INTRODUCTION

Fluctuations of the amplitude and phase of electromagnetic waves propagating through the atmosphere are caused, in part, by local fluctuations in absorption and refraction. We consider the absorption and refraction caused by the water vapor monomer and calculate the relationship between local fluctuations in absorption and refraction and the local fluctuations in temperature T , humidity Q , and total pressure P . Similar results have been determined for the microwave resonances of O_2 by *Liebe and Hopponen* [1977]. The combination of their results and ours gives a complete view of fluctuations in microwave resonance absorption and refraction caused by fluctuations in T , Q , and P . Our results are reported in detail here for frequencies less than 16 cm^{-1} (480 GHz) because of their interest to radio scientists, but our calculations are complete from radio wavelengths to nearly $5\text{ }\mu\text{m}$ and are reported by *Hill et al.* [1980a, b]. In a related study, *Zhevakin and Naumov* [1967a] calculate the derivatives of the real part of the refractive index with respect to temperature and water vapor partial pressure for frequencies in the range $1\text{ cm}^{-1} < \nu < 20\text{ cm}^{-1}$, where $\nu = 1/\lambda$ is inverse wavelength.

There are mechanisms other than the H_2O and

O_2 resonances that absorb electromagnetic waves. For instance, there is extinction by aerosols as well as the observed and as yet unexplained excess attenuation. We do not consider the absorption fluctuations caused by these mechanisms. For instance, consideration of aerosol or particulate contributions would necessitate considering fluctuations in particle concentration and particle size distribution. Fluctuations in T and Q cause fluctuations in aerosol extinction by varying the particle size distribution [*Nilsson* 1979]. The observed absorption (for, say, $\nu \leq 50\text{ cm}^{-1}$) is greater than that calculated from the sum of all molecular resonances. This excess absorption is greater than that from resonances only in the windows between the absorption resonances. Including the excess absorption in the present analysis would require accurate knowledge of its variation with T , Q , P , and ν . *Waters* [1976] describes the model of excess absorption proposed by *Gaut and Reifstein* which is proportional to humidity, frequency squared, and $T^{-2.1}$. Recent measurements have shown a quadratic rather than linear dependence on humidity at both microwave [*Hogg and Guiraud*, 1979] and higher frequencies (for $13.8\text{ cm}^{-1} \leq \nu \leq 50\text{ cm}^{-1}$ by *Bohlander* [1979] and at $\nu = 7.1\text{ cm}^{-1}$ by *Llewellyn-Jones et al.* [1978]). Recent measurements [*Bohlander*, 1979; *Rice and Ade*, 1979] have also shown a more gradual increase of excess absorption with frequency for $\nu > 7\text{ cm}^{-1}$ than

This paper is not subject to U.S. copyright. Published in 1981 by the American Geophysical Union.

that given by the Gaut and Reifenstein model. The observations by *Bohlander* [1979] in the temperature range 295 K < T < 355 K indicate a temperature dependence of excess absorption more nearly like T^{-4} for $13 \text{ cm}^{-1} < \nu < 20 \text{ cm}^{-1}$, increasing to T^{-6} for $20 \text{ cm}^{-1} < \nu < 35 \text{ cm}^{-1}$. For $\nu = 7.1 \text{ cm}^{-1}$, *Llewellyn-Jones et al.* [1978] found excess absorption to have a temperature dependence like T^{-6} for $T \geq 300 \text{ K}$ but a much more rapid decrease with increasing temperature for $T \leq 300 \text{ K}$. We conclude that the dependence of excess absorption on ν , T , Q , and P at microwave to submillimeter wavelengths is not sufficiently well known to include in the calculations that follow. As excess attenuation has a negligible impact on refraction, this problem does not affect our values of refraction or the contributions of fluctuations in T , Q , or P to refraction fluctuations. In fact, measurements by *Kemp et al.* [1978] of refraction by water vapor in the range $10 \text{ cm}^{-1} < \nu < 50 \text{ cm}^{-1}$ show good agreement with refraction calculated from the sum of water monomer lines using the Gross line shape.

THEORY

We write the refractivity of air as its value at optical frequencies N_{opt} plus the refraction N_a due to the infrared resonances of water vapor:

$$N = N_{\text{opt}} + N_a$$

where

$$N_{\text{opt}} = N_d + N_w$$

$$N_d = 103.29 P/T$$

$$N_w = -1.765 \times 10^{-18} Q$$

$$N_a = \sum N_{ai}$$

and where P is total atmospheric pressure in torr, T is temperature in degrees Kelvin, Q is water vapor concentration in molecules per cubic centimeter, and N_{ai} is the refraction of the i th water vapor resonance. The expressions for N_d and N_w are derived from formulae given by *Goody* [1965]. Since P is the total pressure (not the partial pressure of dry air), N_d contains contributions from H_2O as well as O_2 , N_2 , and A ; N_w is just a correction to account for the fact that at visible frequencies the refraction per molecule is less for H_2O than for O_2 or N_2 . The continuum refraction $N_d + N_w$

is caused by the ultraviolet resonances of O_2 , N_2 , and H_2O and is essentially independent of frequency for $\lambda \geq 10 \mu\text{m}$. We have neglected the near infrared resonances of O_2 and the refraction due to CO_2 ; their relatively small effect is discussed by *Zhevakin and Naumov* [1967a]. As noted previously, the microwave resonances of O_2 are discussed by *Liebe and Hopponen* [1977]. The real part of the refractive index n_r is related to refractivity by $N = (n_r - 1) \times 10^6$.

The absorption coefficient β of the water vapor monomer resonances is found by summing the contributions β_i of all lines:

$$\beta = \sum \beta_i$$

The imaginary part of the refractive index is related to β by $n_i = \beta/4\pi\nu$.

We use the Gross line shape so that the refraction and absorption of a single resonance with line frequency ν_i is given by

$$N_{ai} = \frac{S_i Q}{2\pi^2} \frac{\nu_i^2 - \nu^2}{(\nu_i^2 - \nu^2)^2 + 4\nu^2 \alpha_i^2} \times 10^6$$

$$\beta_i = \frac{S_i Q}{\pi} \frac{4\nu^2 \alpha_i}{(\nu_i^2 - \nu^2)^2 + 4\nu^2 \alpha_i^2}$$

where S_i is the line strength, and α_i is the line width. The line strength depends on T , and line width depends on T , P , and Q . The functional dependence that we use is given by *Hill et al.* [1980a].

We write T , Q , and P as the sum of their mean values $\langle T \rangle$, $\langle Q \rangle$, $\langle P \rangle$, and their fluctuations caused by turbulence δT , δQ , δP . For instance, $T = \langle T \rangle + \delta T$. We can now relate the fluctuations in n_r and n_i to those of T , Q , and P :

$$\delta n_r = A_T \frac{\delta T}{\langle T \rangle} + A_P \frac{\delta P}{\langle P \rangle} + A_Q \frac{\delta Q}{\langle Q \rangle} \quad (1)$$

$$\delta n_i = B_T \frac{\delta T}{\langle T \rangle} + B_P \frac{\delta P}{\langle P \rangle} + B_Q \frac{\delta Q}{\langle Q \rangle} \quad (2)$$

We call the coefficients A_T , A_P , A_Q , B_T , B_P , and B_Q the sensitivity coefficients, because they are measures of the change in the refraction and absorption caused by fractional fluctuations in T , Q , and P . This nomenclature is similar to that of *Liebe and Hopponen* [1977]. The dimensionless sensitivity coefficients are given by

$$A_T = \langle T \rangle \left(\frac{\partial N}{\partial T} \right)_{P,Q} \times 10^{-6}$$

$$A_P = \langle P \rangle \left(\frac{\partial N}{\partial P} \right)_{T,Q} \times 10^{-6}$$

$$A_Q = \langle Q \rangle \left(\frac{\partial N}{\partial Q} \right)_{T,P} \times 10^{-6}$$

$$B_T = (4\pi\nu)^{-1} \langle T \rangle \left(\frac{\partial \beta}{\partial T} \right)_{P,Q}$$

$$B_P = (4\pi\nu)^{-1} \langle P \rangle \left(\frac{\partial \beta}{\partial P} \right)_{T,Q}$$

$$B_Q = (4\pi\nu)^{-1} \langle Q \rangle \left(\frac{\partial \beta}{\partial Q} \right)_{T,P}$$

where the partial derivatives are to be evaluated at the mean values $\langle T \rangle$, $\langle Q \rangle$, and $\langle P \rangle$, and the subscripts denote the variables held fixed during the partial differentiation. The analytic form of the derivatives is given by Hill *et al.* [1980a, b] and need not be repeated here. For instance, for A_Q we differentiate the explicit Q dependence in N_w and N_{ai} as well as an implicit Q dependence in $\alpha_i(T, P, Q)$.

CALCULATED SENSITIVITY COEFFICIENTS

There are over 42,000 infrared water vapor resonances in the most recent Air Force Geophysics Laboratory (AFGL) line parameters compilation (we use the compilation discussed by Rothman [1978]). For the frequencies discussed here, namely, $\nu < 16 \text{ cm}^{-1}$, only the resonances within the rotational band at $\nu_i \leq 330 \text{ cm}^{-1}$ need be considered. The negligibility of the resonances in the vibrational-rotation bands, $\nu_i \geq 1000 \text{ cm}^{-1}$, is discussed by Zhevakin and Naumov [1967a]. Nevertheless, for each frequency ν at which we compute β , N_a , A_T , A_P , A_Q , B_T , B_P , and B_Q , we have performed the sum over all the resonances.

We calculate the sensitivity coefficients for the mean conditions $\langle T \rangle = 300 \text{ K}$, $\langle P \rangle = 760 \text{ torr}$, and 80% relative humidity, so $\langle Q \rangle = 6.82 \times 10^{17}$ molecules per cubic centimeter (or 28.2 mbar partial pressure of water vapor). The results are shown graphically for $\nu < 16 \text{ cm}^{-1}$ (480 GHz) in Figure 1. Separate graphs of N_a , A_T , and A_Q for $\nu < 3 \text{ cm}^{-1}$ are shown in Figure 2 so that the details at low frequencies are apparent. Similar graphs for

frequencies as high as 2060 cm^{-1} are given by Hill *et al.* [1980a, b].

The graphs of absorption coefficient show the water vapor resonances at $\nu < 16 \text{ cm}^{-1}$ and a broad underlying absorption from the wings of the very strong lines at $\nu > 16 \text{ cm}^{-1}$. The absorption coefficient is given in nepers per centimeter. To convert to decibels per kilometer, multiply our values by 4.34×10^5 . Of course, the microwave resonances of O_2 and the excess absorption are not shown. There are 43 water vapor resonances at $\nu < 16 \text{ cm}^{-1}$ and 5 at $\nu < 3 \text{ cm}^{-1}$. We have numerically resolved all these resonances, although only the seven strongest resonances are evident in the graphs.

The graphs of refractivity N_a show the usual effect of a resonance superposed on a decreasing background. The decreasing behavior of this background is dominated by the strong resonance at 556 GHz. A constant, i.e., nondispersive, behavior of this background is obvious at the lowest frequencies. This nondispersive value of N_a for $\nu \rightarrow 0$ is caused by the sum of all the strong resonances at $\nu > 16 \text{ cm}^{-1}$. As $\nu \rightarrow 0$, each line contributes a refraction:

$$N_{ai} \rightarrow (S_i Q / 2\pi^2 \nu_i^2) \times 10^6$$

The sum of all these contributions adds to the relatively Q insensitive refraction at optical frequencies to provide the relatively strong Q dependence at radio frequencies. We see that the strongest contributions come from the rotational band where S_i is largest and ν_i is smallest.

We graph the contribution of the resonances to A_T , namely, $A_T + N_a \times 10^{-6}$. To obtain A_T , one must add the continuum contribution $-N_a \times 10^{-6} = -2.62 \times 10^{-4}$ to the values graphed.

The pressure-broadened O_2 band near 60 GHz has a peak absorption about 1/20 as large as the prominent water vapor line at 183 GHz (6.1 cm^{-1}) for our $\langle T \rangle$, $\langle P \rangle$, and $\langle Q \rangle$. The results of Liebe and Hopponen [1977] show that the contribution of this O_2 band to refractivity and A_T is also smaller than that shown in Figure 1 for the 183-GHz water vapor line. The O_2 band near 119 GHz is much weaker than that at 60 GHz and has an even smaller effect on refractivity and A_T .

The graphs of A_Q show that the infrared resonances dominate the A_Q value, since the continuum contribution is only -1.2×10^{-6} for our $\langle T \rangle$, $\langle P \rangle$, $\langle Q \rangle$. Except for the change in scale, the A_Q graphs look like those of N_a . This is not surprising, because

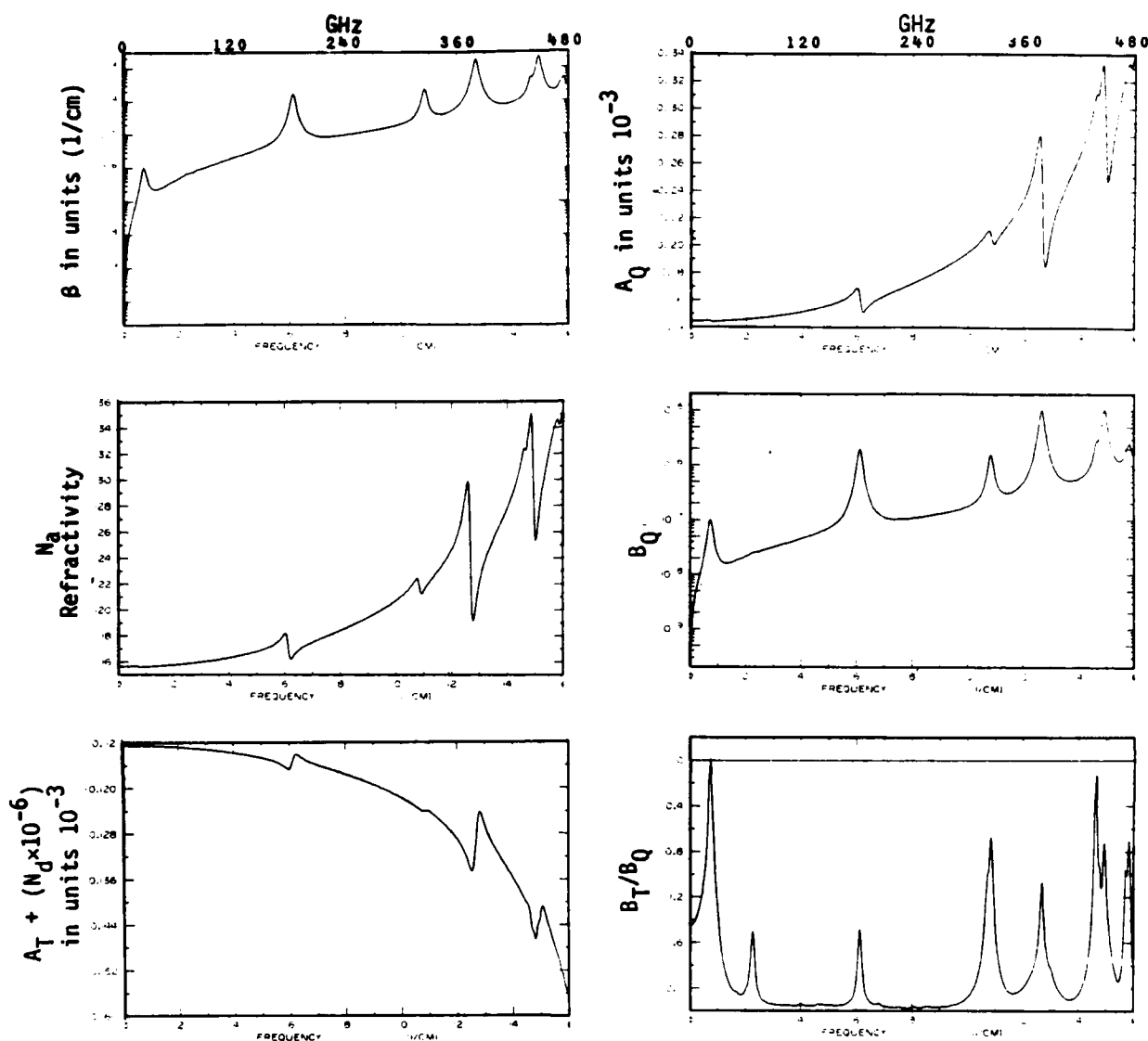


Fig. 1. Absorption coefficient, the refractivity N_a , and the sensitivity coefficients for $\nu < 16 \text{ cm}^{-1}$ and mean conditions: $T = 300 \text{ K}$, $P = 1 \text{ atm}$, 80% relative humidity, i.e., partial pressure of water vapor is 28.2 mbar.

neglecting the continuum and line width contributions to A_Q gives A_Q proportional to N_a .

The graphs for A_p are not shown here. They are given by Hill *et al.* [1980b]. The line contribution to A_p is localized to each line so that, unlike N_a , it has no 'background' value from strong resonances at $\nu > 16 \text{ cm}^{-1}$. This line contribution to A_p oscillates about zero, taking very small values between resonances, with peak values of only $\pm 6 \times 10^{-6}$ for $\nu < 16 \text{ cm}^{-1}$. This is to be compared with the

A_p value from the continuum of $N_a \times 10^{-6} = 2.62 \times 10^{-4}$ for our (T) , (P) , (Q) . Thus A_p is essentially the same for $\nu < 16 \text{ cm}^{-1}$ as it is for visible frequencies.

A test of our computations is to compare our values of refraction, A_T , A_p , and A_Q with known values at radio wavelengths. We compare our computed values at $\nu = 10^{-2} \text{ cm}^{-1}$, i.e., $\lambda = 1 \text{ m}$, with the radio refractive index given by Thayer [1974]. Our N_a and N_w both differ by 0.16% from

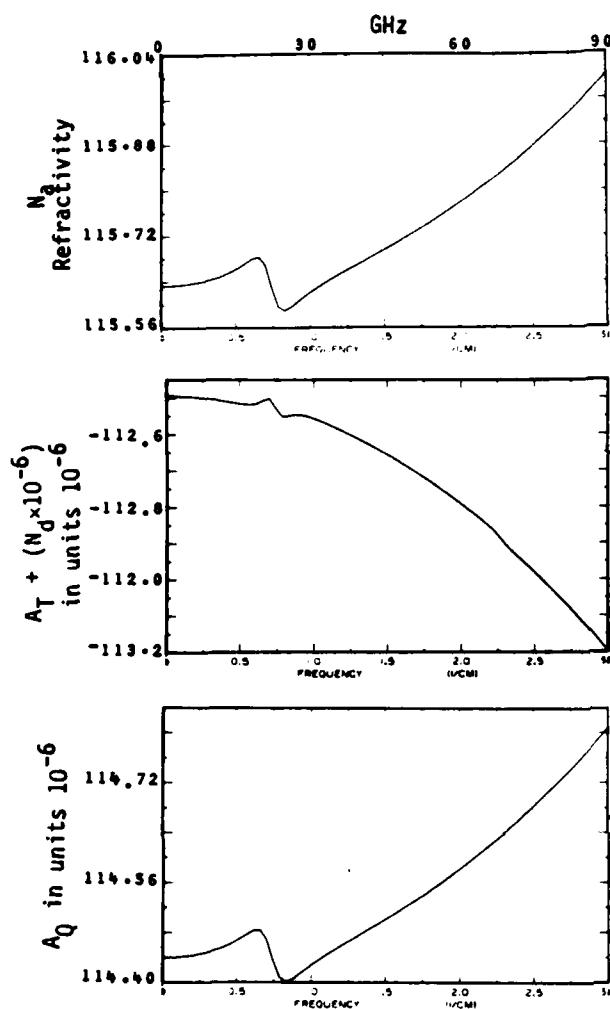


Fig. 2. Details of the refractivity N_d and A_T and A_Q for $\nu < 3 \text{ cm}^{-1}$.

those derived from Thayer's equation. Our N_d value is 2.5% smaller than that derived from Thayer's equation. Zhevakin and Naumov [1967b] calculated N_d by adding contributions of strong lines; their value differed from that at centimeter wavelengths by 2.7%. The contributions of the resonances to A_p is -7×10^{-12} , compared with the dry air contribution 2.61×10^{-4} ; so the 0.16% difference of our A_p from that obtained from Thayer's equation is caused by the different N_d values. The contribution of water vapor resonances to A_T is 5% smaller in absolute value than $|A_T + N_d \times 10^{-6}|$ calculated from Thayer's equation. However, we have not added contributions of infrared resonances of O_2

or CO_2 or other species to our evaluation of A_T or the value of N_d at radio frequencies. The contribution of all resonances to A_Q is 2.4% smaller than that obtained from Thayer's equation. We do not know whether or not the agreement between our calculated N_d and the known value at radio wavelengths implies that the strengths and resonance frequencies of strong rotational lines in the AFGL compilation are correct or if the agreement is fortuitous due to cancelling errors.

The graphs of B_Q appear to be similar to those of the absorption coefficient. This is because of the approximation $B_Q \approx \beta/4\pi\nu$, obtained by neglecting the Q dependence of the line width. We see that humidity fluctuations cause the strongest absorption fluctuations where absorption is strongest. Kanevskii [1972] considered the effect of absorption fluctuations on the amplitude of a plane wave for frequencies $10 \text{ cm}^{-1} < \nu < 14 \text{ cm}^{-1}$. He shows large effects on the amplitude variance at frequencies where resonances produce large absorption, and practical propagation paths would be very short. Otherwise the effect is small.

We show a graph of B_T/B_Q to illustrate the relative importance of temperature and humidity fluctuations to absorption fluctuations. Between lines, B_T/B_Q has a value of -2.1 with excursions to smaller absolute values at the resonances. The results of Liebe and Hopponen [1977] show that the pressure-broadened O_2 band dominates B_T near 60 GHz. Of course, B_T includes the effect of changes in O_2 concentration, because the ideal gas law shows that for fixed total pressure, water vapor concentration, and fixed ratio of O_2 concentration to those of N_2 and Ar, any temperature change causes an opposite change in O_2 concentration.

We do not show graphs of B_p here. Graphs of B_p/B_Q are given by Hill et al. [1980b]. These graphs show B_p/B_Q close to 0.8 between resonances with excursions to nearly -1.0 at the stronger resonances.

DISCUSSION

In atmospheric turbulence, a typical order of fractional fluctuations is

$$\frac{\delta P}{\langle P \rangle} \ll \frac{\delta T}{\langle T \rangle} \leq \frac{\delta Q}{\langle Q \rangle}$$

In view of the relative values of A_p and A_T and those of B_p and B_Q , we neglect the contributions

of total pressure fluctuations to both the real and imaginary parts of refractive index. In the case of very strong humidity fluctuations, $(\delta T / \langle T \rangle) \ll (\delta Q / \langle Q \rangle)$, one may neglect the temperature fluctuations relative to the humidity fluctuations for fluctuations in both real and imaginary parts of the refractive index, because $A_T / A_Q \approx -3$ for $\nu < 16 \text{ cm}^{-1}$, and the absolute value of B_T / B_Q does not exceed 2.2. One must be careful for the case of absorption fluctuations, because inclusion of excess absorption may significantly increase the magnitude of B_T / B_Q in the windows between absorption lines. At submillimeter and lower frequencies, say, $\nu < 50 \text{ cm}^{-1}$, no contribution by excess absorption is added to our calculated values of β , B_Q , B_T / B_Q , or B_P / B_Q for reasons discussed previously. Readers may use their favorite formula for excess absorption as a function of ν , T , Q , and P to add these contributions to the values in our graphs.

Neglecting pressure fluctuations, Hill *et al.* [1980a] give the relationship between structure parameters of both real and imaginary parts of the refractive index and structure parameters of temperature and humidity. They also consider the variance of log-amplitude to show that refraction fluctuations give much larger amplitude fluctuations than do absorption fluctuations for most cases of practical interest.

Acknowledgments. We thank Dr. Hans Liebe for his helpful discussions.

REFERENCES

- Bohlander, R. A. (1979), Spectroscopy of water vapour, Ph.D. thesis, Dep. of Phys., Univ. of London, England.
- Goody, R. M. (1965), *Atmospheric Radiation*, vol. 1, p. 389, Clarendon, Oxford, England.
- Hill, R. J., S. F. Clifford, and R. S. Lawrence (1980a), Refractive index and absorption fluctuations in the infrared caused by temperature, humidity, and pressure fluctuations, *J. Opt. Soc. Am.*, **70**, 1182-1205.
- Hill, R. J., S. F. Clifford, and R. S. Lawrence (1980b), Computed refraction and absorption fluctuations caused by temperature, humidity, and pressure fluctuations: Radio waves to $5 \text{ } \mu\text{m}$, *NOAA Tech. Mem., ERL-WPL 59*, 65 pp., Nat. Oceanic Atmos. Admin., Boulder, Colo.
- Hogg, D. C., and F. O. Guiraud (1979), Microwave measurements of the absolute values of absorption by water vapour in the atmosphere, *Nature*, **279**, 408-409.
- Kanevskii, M. B. (1972), The problem of the influence of absorption on amplitude fluctuations of submillimeter radio waves in the atmosphere, *Radiophys., Quantum Electron.*, **15**, 1486-1487.
- Kemp, A. J., J. R. Birch, and M. N. Afsar (1978), The refractive index of water vapour: A comparison of measurement and theory, *Infrared Phys.*, **18**, 827-833.
- Liebe, H. J., and J. D. Hopponen (1977), Variability of EHF air refractivity with respect to temperature, pressure, and frequency, *IEEE Trans. Antennas Propagat.*, **AP-25**, 336-345.
- Llewellyn-Jones, D. T., R. J. Knight, and H. A. Gebbie (1978), Absorption by water vapour at 7.1 cm^{-1} and its temperature dependence, *Nature*, **274**, 876-877.
- Nilsson, B. (1979), Meteorological influence on aerosol extinction in the $0.2\text{--}40 \text{ } \mu\text{m}$ wavelength range, *Appl. Opt.*, **18**, 3457-3473.
- Rothman, L. S. (1978), Update of the AFGL atmospheric absorption line parameters compilation, *Appl. Opt.*, **17**, 3517-3518.
- Rice, D. P., and P. A. R. Ade (1979), Absolute measurements of the atmospheric transparency at short millimetre wavelengths, *Infrared Phys.*, **19**, 575-584.
- Thayer, G. D. (1974), An improved equation for the radio refractive index of air, *Radio Sci.*, **9**, 803-807.
- Waters, J. W. (1976), Absorption and emission by atmospheric gases, *Methods of Experimental Physics*, vol. 12(B), edited by M. L. Meeks, pp. 142-176, Academic, New York.
- Zhevakin, S. A., and A. P. Naumov (1967a), Refraction of millimeter and submillimeter radiowaves in the lower atmosphere, *Radio Eng. Electron. Phys.*, **12**, 885-894.
- Zhevakin, S. A., and A. P. Naumov (1967b), The index of refraction of lower atmosphere for millimeter and submillimeter radiowaves. The rotational part of the dielectric permittivity of atmospheric water vapor at wavelengths greater than 10 micrometers , *Radio Eng. Electron. Phys.*, **12**, 1067-1076.

A laser rain gauge

By Ting-i Wang and Robert S. Lawrence

NOAA Research Labs, Boulder, CO 80303

Detection of the scintillations caused by raindrops falling through a laserbeam can serve as the basis of a rain gauge. The laser technique measures rainfall averaged over paths several hundred meters long. Because the measurements can be made on line without extensive data reduction, the technique appears promising for practical use.

Precise measurements of rainfall are nowhere near as simple as you might imagine. The problem is that rainfall is highly variable from point to point, and conventional rain gauges simply measure the amount of rain that falls at a single point. However, for agricultural and flood-control purposes, it is total rainfall over an area that is important. To measure that quantity, a dense network of conventional gauges is needed. We were able to perform such a measurement by observing the fluctuations in intensity of a laser beam passing through several hundred meters of rain-filled atmosphere near the ground.

We have shown that the scintillations produced by raindrops falling through a collimated laser beam can be used to measure the drop-size distribution and the rainfall rate,^{1,2} both averaged over the path. We have also shown that the variance of the scintillations measured by a linear detector at frequencies near one kilohertz is closely related to rain rate³ and is nearly independent of drop-size distribution. If only rain rate is desired, the variance-type optical rain gauge is simple to construct. It can use a diverging beam, thus eliminating the practical difficulties in maintaining adjustment and pointing of a collimated beam. Furthermore, it is less sensitive to the presence of updrafts and downdrafts along the beam and can thus be used over rough terrain. Here we describe the basic principle and the design of an optical rain gauge using the variance of the irradiance scintillations induced by raindrops.

For a plane wave incident on a raindrop, the scattered light can be approximated by two components; the light diffracted by the sharp boundary of the drop and the light refracted by passage through the drop.⁴ The refracted light is much weaker than the diffracted light because the wavelength of the incident wave is much shorter than the radius of the drop, and the refractive index is large (i.e., $k\Delta n \gg 1$, where k is the wavenumber, a is the radius of the drop, and $1 + \Delta n$ is the refractive

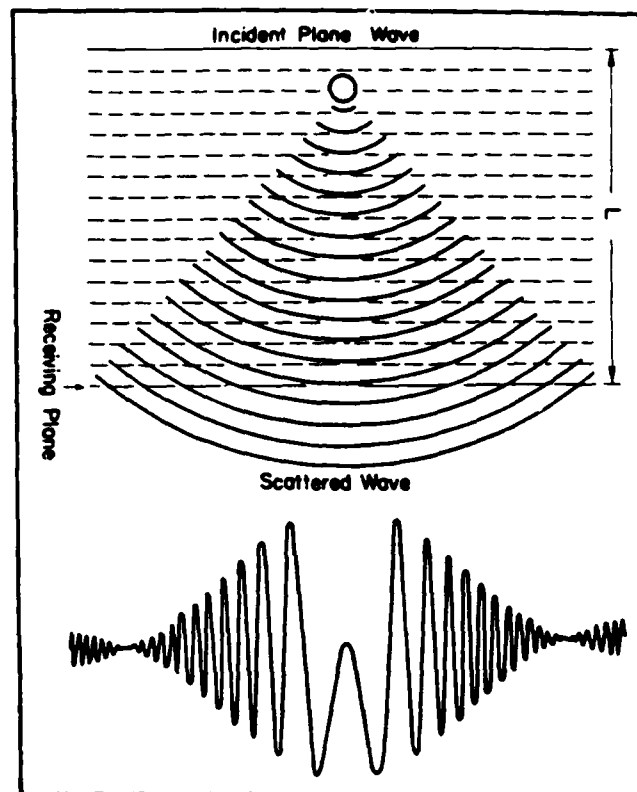


Fig 1 The interference pattern produced by a spherical raindrop. The fine fringes are caused by phase interference of the incident wave and scattered wave

index of water). Thus the total scattered light is approximately equal to the diffracted light.

The scattered field can be considered as a spherical wave emitted from the center of the raindrop because we are only interested in the far-field solution (i.e., where the drop radius is much less than the Fresnel-zone-size, $a \ll (\lambda x)^{1/2}$, where x is the distance between the drop and the receiver, and the transverse coordinate is much less than the longitudinal coordinate). The interference at the receiving plane, caused by the incident plane wave and the scattered spherical wave, gives the fine fringes shown in Fig. 1. The envelope of the interference pattern is the well-known Airy diffraction pattern of a sphere. Path-averaged rain rates can be obtained by observing the movement of these raindrop-induced interference patterns.

We have shown³ that, for a line detector extending in the horizontal direction, the variance of the irradiance scintillations is

$$\sigma^2 \sim h [1 - 0.0451h^{0.21} (f_1^2 + f_1 f_2 + f_2^2)] \quad (1)$$

where h is the path-averaged rain rate (milli-

Robert S. Lawrence and Ting-i Wang are both specialists in optical remote sensing at the National Oceanic and Atmospheric Administration's Wave Propagation Laboratory in Boulder. Lawrence received a master's degree in physics in 1950 from Yale University. Wang received a doctorate in electrical engineering in 1973 from Dartmouth

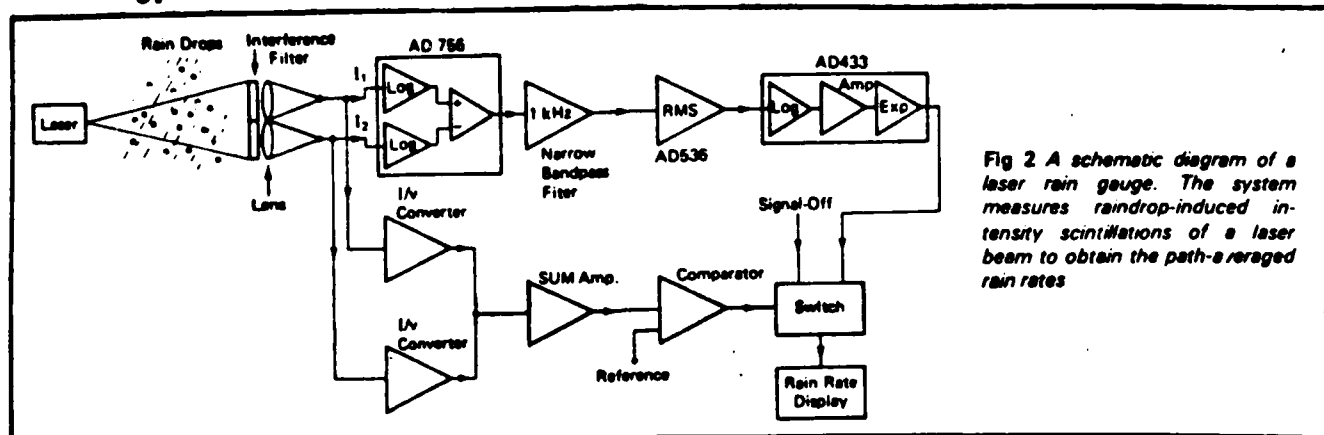


Fig 2 A schematic diagram of a laser rain gauge. The system measures raindrop-induced intensity scintillations of a laser beam to obtain the path-averaged rain rates

meters per hour), and f_1 and f_2 are the low and high cutoff frequencies (kHz) respectively. Obviously when f_1 and f_2 are small, the variance is proportional to the path-averaged rain rate. However, if the observed frequency is too low, contamination by turbulence-induced scintillations cannot always be ignored, particularly when the wind is strong. If the observed frequency is too high, the measurement is sensitive to drop-size distribution which usually varies with location and time. We found that a narrowband filter around 1 kHz is an optimum choice. In this case ($f_1 = f_2 = 1$ kHz), Eq. 1 becomes

$$\sigma^2 \sim h [1 - 0.135h^{0.21}] \quad (2)$$

For rain rates of 0.1 mm/hour to 100 mm/hour, we

can approximate Eq. 2 by

$$h \sim \sigma^{2.1} \quad (3)$$

Eq. 3 is derived based on the assumption of a plane wave such as from a collimated beam. It is not difficult to show that for a spherical wave (point source), the relationship between rain rate and the variance of the irradiance scintillations is

$$h \sim \sigma^{2.02} \quad (4)$$

For a diverging beam, the dependence will be between $\sigma^{2.02}$ and $\sigma^{2.1}$.

A schematic diagram of the system is shown in Fig. 2. The transmitter is a helium-neon laser. In front of the detector is a thin slot, 20 centimeters

JEC LASERS, INC.

INTRODUCING A NEW STANDARD OF RELIABILITY & PERFORMANCE
CW Nd:YAG LASERS FOR INDUSTRIAL, SCIENTIFIC & OEM USERS

FEATURES

- Up to 15 watts TEM₀₀, 100 watts multimode power
- Acoustic Q-switch option for giant pulse operation
- Single or twin Krypton lamp operation
- Low cost
- Computer remote control capability
- Improved laser head design for increased lamp life
- Ultra-stable regulated DC power supply, single or 3 phase operation
- Simple alignment & maintenance

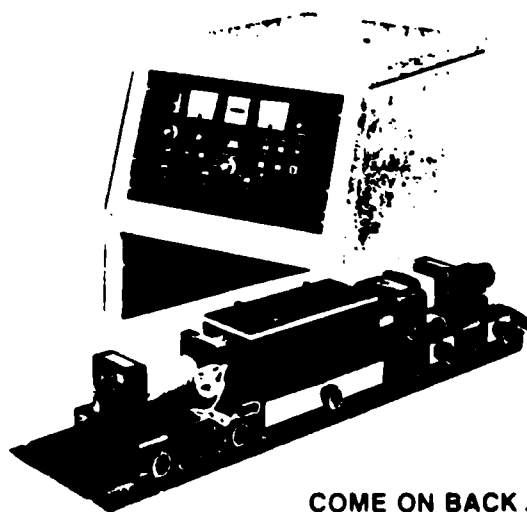


WE'VE CHANGED OUR NAME BUT OUR
DEDICATION REMAINS THE SAME

For more information call or
write Marketing Dept

JEC LASERS, INC.
253 CROOKS AVENUE
PATERSON, NEW JERSEY 07503
(201) 523-3500 Telex 226000 ETLX-UR

JEC Lasers Series 1000 continuous wave Nd YAG laser systems are pumped with either single or twin Krypton arc lamps. The proven modular construction and plug-in replacement module concept provides maximum performance with minimum maintenance. System reliability has been proven by demanding production line operation.



COME ON BACK...
TO QUALITY

Technology

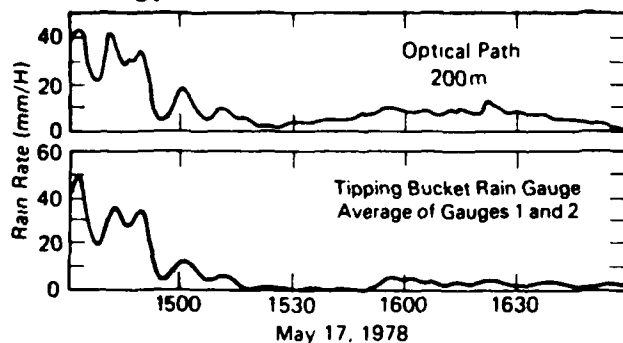


Fig 3 A comparison shows excellent agreement between the optically measured rain rate (upper diagram) and the average rain rate measured by two tipping-bucket rain gauges near the ends of the optical path (lower diagram)

long and 0.1 cm high, extending horizontally. A narrowband interference filter excludes background light. Two lenses focus the light on two p-i-n silicon detectors. Logarithmic amplifiers normalize the fluctuating signals with respect to unperturbed light intensity so that a change in transmitter intensity or a movement of the beam will not affect the measurements. The subtraction of the signals from the log amplifiers cancels the effect of noise common to both detectors (such as 120-hertz ripple due to imperfect filtering of the power supply), and makes the instrument less sensitive to vibrations and changes in the transmitted intensity. The output is fed into a narrow-bandpass electronic filter with center frequency 1 kHz and rejection ratio greater than 60 decibels between 1 kHz and 200 Hz.

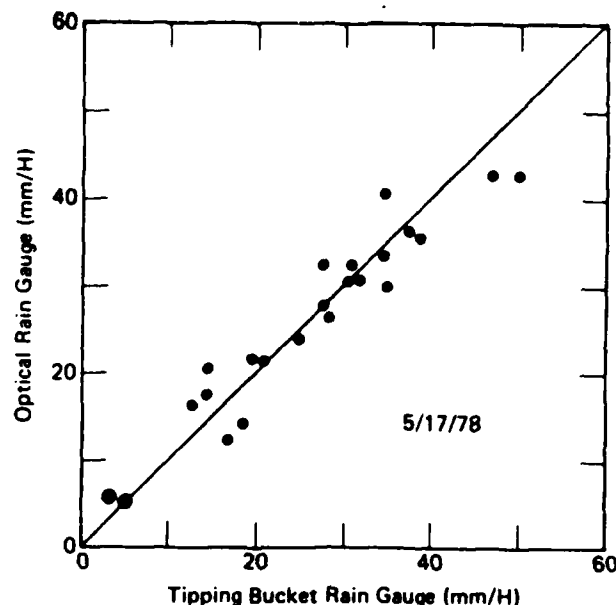



Fig 4 A linear-regression scatter diagram of the rain rates measured by the laser system and rain rates measured by the average of two conventional tipping-bucket rain gauges

The standard deviation of the filtered signals is calculated by an Analog Device root-mean-square integrated circuit (AD536) with a 10-second time constant. A log and antilog (exponential) integrated circuit (AD433) calculates the rain rates. To prevent false measurements due to low signals, the outputs of the photodetectors are amplified and clipped. When either signal is below the threshold, the comparator flips the switch so that a voltage indicating "signal off" is shown on the display.

A comparison of the rainfall rates measured by the optical technique and conventional tipping-bucket rain gauges is shown in Fig. 3. Because of the poor time resolution of the tipping-bucket rain gauges, we use a one-minute time constant on both records. Two tipping-bucket rain gauges were placed near the ends of the 200-m optical path. The average of the two rain gauges is shown in the lower diagram. The agreement between the optical measurements and the conventional rain-gauge measurements is excellent, with a correlation coefficient of 0.97. The linear regression of these two quantities is shown in Fig. 4. For rain rates above about 10 millimeters per hour, the results are plotted for a fixed one-minute time constant (shown by dots in Fig. 4). For low rain rates, the time resolution of the tipping-bucket rain gauge is insufficient to compare with the optical measurements. We decided to take the average of the optical data between tips of the tipping-bucket gauge and to plot this against the tipping-bucket gauge reading (shown by big dots in Fig. 4). The agreement is very good and might have been further improved by using more rain gauges along the path.

References

1. Ting-i Wang and S. F. Clifford *J Opt Soc Am* 65 977 (1975)
2. Ting-i Wang, G. Lerfeld, R. S. Lawrence and S. F. Clifford *Appl Opt* 16 2246 (1977)
3. Ting-i Wang, K. B. Earnshaw and R. S. Lawrence *Appl Opt* 17 384 (1978)
4. H. C. Van de Hulst *Light Scattering by Small Particles* Wiley, New York (1957)




MEMBER OF HUGHES AIRCRAFT COMPANY

KNOWN THE WORLD OVER FOR EXCELLENCE IN INFRARED COMPONENTS

- INFRARED DETECTORS
- CRYOGENICS
- AMPLIFIERS
- CCD READ-OUT TECHNOLOGY

FOR FURTHER INFORMATION,
Contact: Santa Barbara Research Center
75 Connor Drive, Goleta, California 93117
Attention: Howard Wurtz
Telephone (805) 968-3511
Telex 910 334 1884 HACSBAR



AD-A171 526

INVESTIGATION OF MILLIMETER WAVE PROPAGATION IN THE
ATMOSPHERE(U) NATIONAL OCEANIC AND ATMOSPHERIC
ADMINISTRATION BOULDER CO WA. S F CLIFFORD ET AL.

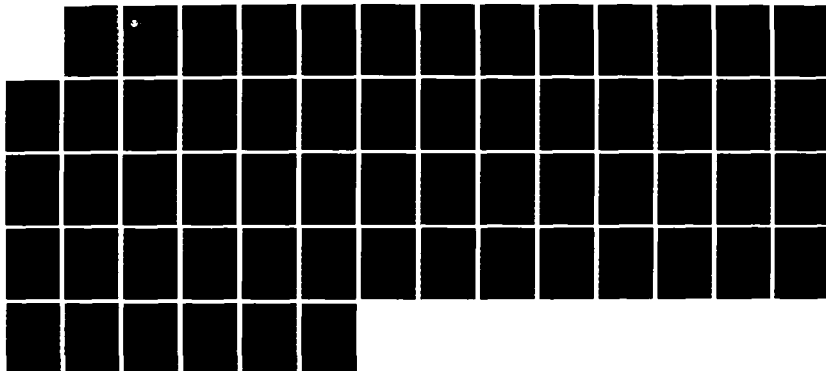
2/2

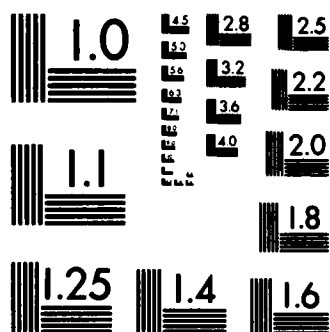
UNCLASSIFIED

18 JUL 86 ARO-18029. 18-05 ARO-55-81

F/G 20/14

NL





MICROCOPY RESOLUTION TEST CHART
NATIONAL BUREAU OF STANDARDS-1963-A

NOAA Technical Report ERL 429-WPL 60



Data Analysis of the NOAA-GIT Millimeter-Wave Propagation Experiment Near Flatville, Illinois

R. J. Hill, W. P. Schoenfeld,
J. P. Riley, J. T. Priestley,
S. F. Clifford, S. P. Eckes,
R. A. Bohlander, R. W. McMillan

Wave Propagation Laboratory
Boulder, Colorado

August 1985

U.S. DEPARTMENT OF COMMERCE
Malcolm Baldrige, Secretary

National Oceanic and Atmospheric Administration

Environmental Research Laboratories
Boulder, Colorado
Vernon E. Derr, Director

NOTICE

Mention of a commercial company or product does not constitute an endorsement by NOAA Environmental Research Laboratories. NOAA does not authorize any use of information from this publication for advertising or publicity purposes.

CONTENTS

	Page
ABSTRACT.....	1
1. INTRODUCTION.....	1
2. QUANTITIES COMPUTED FROM THE GIT MILLIMETER-WAVE DATA.....	2
2.1 Introduction.....	2
2.2 Phase-Difference Statistics.....	4
2.3 Intensity Statistics.....	5
2.4 Mixed Intensity and Phase-Difference Statistics.....	6
2.5 Second Moment of the Field: The Mutual Coherence Function.....	7
2.6 Fourth Moment of the Field.....	9
2.7 Extrema.....	13
2.8 Probability Distribution Functions.....	13
2.9 Fourier Transforms.....	13
2.10 Figures of Merit.....	14
3. QUANTITIES COMPUTED FROM THE NOAA MICROMETEOROLOGICAL DATA.....	15
3.1 Introduction.....	15
3.2 Conversion to Units.....	17
3.3 Averages, Variances, and Cross-Correlations.....	19
3.4 Turbulence Fluxes.....	20
3.5 Spatial Structure Parameters.....	22
3.6 Time-Lagged Structure Parameters.....	23
3.7 Extrema.....	24
3.8 Probability Distribution Functions.....	24
3.9 Fourier Transforms.....	25
3.10 Refraction and Absorption Structure Parameters.....	25
4. PROBLEMS WITHIN THE DATA.....	27
4.1 Introduction.....	27
4.2 Cures for Data Aquisition Errors.....	27
4.3 Cures for Millimeter-Wave Data Problems.....	28
4.4 Cures for Micrometeorological Data Problems.....	31
5. OVERVIEW OF THE DATA PROCESSING SOFTWARE.....	34
5.1 Introduction.....	34
5.2 FLATCOPY.....	36
5.3 METAPE.....	37
5.4 Stripchart Data Visualization.....	38
5.5 PED 2 PAR and MODPARM.....	40
5.6 MILD RV and METDRV.....	41
5.7 Graphing the 25.6 s Statistics.....	42
5.8 MILRDR and METRDR.....	43
5.9 MILFFT and METFFT.....	44
5.10 Using the Answer Files.....	45
5.11 Archiving of Disk Files.....	46

6.	REDUCED MILLIMETER-WAVE AND MICROMETEOROLOGICAL DATA.....	46
6.1	Introduction.....	46
6.2	Tabular Results.....	47
6.3	Graphical Results.....	50
7.	ACKNOWLEDGMENTS.....	54
8.	REFERENCES.....	54

Data Analysis of the NOAA-GIT Millimeter-Wave Propagation Experiment Near Flatville, Illinois

**R. J. Hill, W. P. Schoenfeld¹, J. P. Riley, J. T. Priestley,
S. F. Clifford, S. P. Eckes¹, R. A. Bohlander², R. W. McMillan²**

ABSTRACT. The authors discuss the quantities calculated from the millimeter-wave and micrometeorological data base. The data base was obtained from the millimeter-wave propagation experiment conducted near Flatville, Illinois, by the National Oceanic and Atmospheric Administration (NOAA) and Georgia Institute of Technology (GIT). The repair of data-base errors by digital computation is also discussed, and the overall structure of the data-processing programming is described.

1. INTRODUCTION

The millimeter-wave propagation experiment consisted of five data-taking sessions. The dates for these sessions, including on-site setup and takedown, were June 3 to July 15, 1983; October 30 to December 11, 1983; February 5 to March 9, 1984; May 29 to July 5, 1984; and January 29 to March 26, 1985. Figure 1 is a self-explanatory diagram of the experiment. Georgia Institute of Technology (GIT) was responsible for the millimeter-wave data, and the National Oceanic and Atmospheric Administration (NOAA) for the micrometeorological data. The methods of analysis for the clear-air portion of the micrometeorological data are described here; analyses of the meteorological data for fog, rain, and snow are not discussed. On the other hand, the methods of analysis for the millimeter-wave data given here are identical for clear air, fog, rain, or snow.

¹Cooperative Institute for Research in Environmental Sciences, University of Colorado and National Oceanic and Atmospheric Administration, Boulder, CO 80309.

²Engineering Experiment Station, Georgia Institute of Technology, Atlanta, GA 30332.

The philosophy underlying the data processing is as follows. We calculate all quantities of interest using as few computer programs as possible. For instance, we avoid programming that has the special purpose of calculating intensity covariance or the mutual coherence function. All such diverse statistics are calculated through one program, thereby reducing the complexity of the program library and reducing input/output costs. We use visual inspection of the data from computer-generated microfilm stripcharts that reveal full data time series. Quantities are also averaged into time intervals of 2.56 and 25.6 s and graphed to reveal trends and other problems. We examine graphs of power spectra and cross-spectra to detect noise in the data. Only by such means of data visualization can we be sure that the myriad errors within the data can be identified and avoided. This visualization of the data is thus essential to our data validation. Finally, the end product of the data analysis programs is what we call answer files that contain the statistics from statistically stationary periods on each data tape. Thus investigators are not limited in their interpretation of the data by any a priori decisions as to how the results are to be presented. For instance, the answer files may be interrogated to produce plots of the mutual coherence function for a variety of surface-layer stabilities, each stability case arising from different data runs. There remains great flexibility in graphing and tabulating the answer files for the purpose of making scientific discoveries. Investigators are then limited only by their insight and ingenuity.

2. QUANTITIES COMPUTED FROM THE GIT MILLIMETER-WAVE DATA

2.1 Introduction

The GIT millimeter-wave data consist of 28 channels taken at 100 Hz. (In this report "millimeter-wave" is abbreviated as mm-wave.) Figure 1 shows the arrangement of receiver antennas, housed in a trailer, as viewed from the transmitter; the antennas are designated by a number. There are six possible antenna pairs, each with a different spacing. The antenna pair numbers and their spacings are given in Table 1. For a few experiment runs, the fifth antenna, below antenna 2 (see Fig. 1), was used in place of antenna 4; the objective was observation of anisotropy or multipath effects.

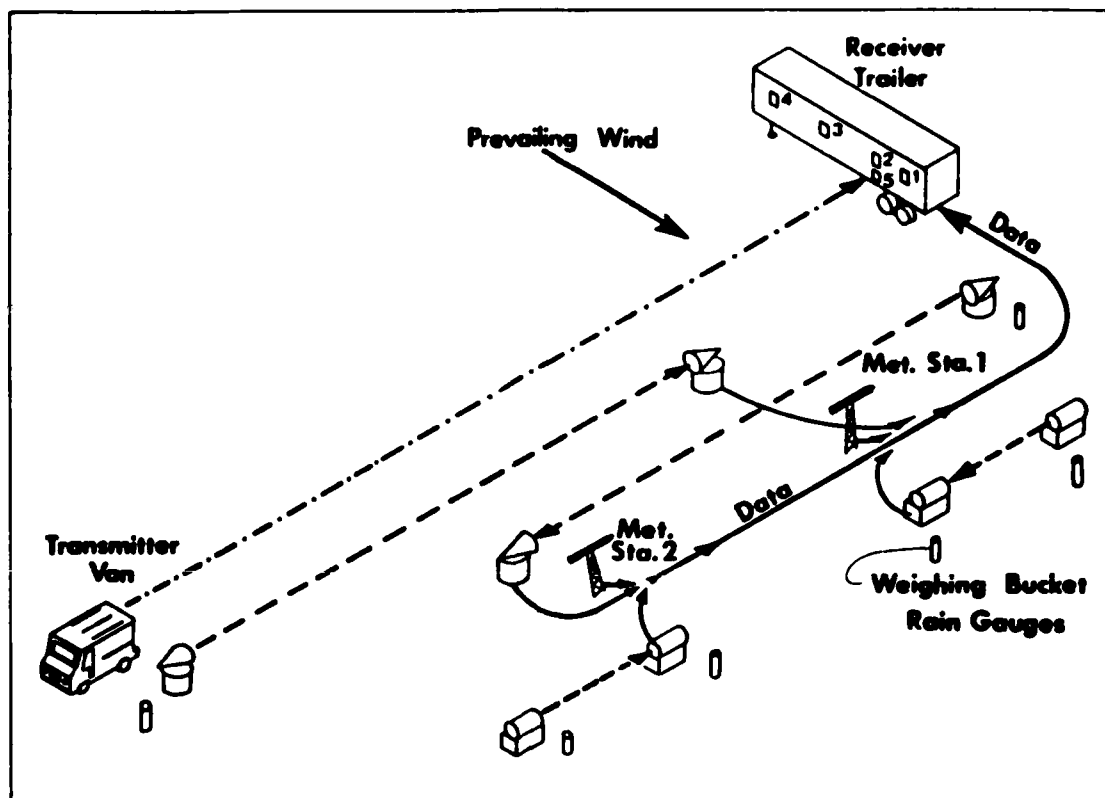


Figure 1.--The instrument positions at the experiment site. The dashed and dotted line denotes mm-wave propagation path (1.4 km); the long-dashed lines, the optical propagation paths (1 km each); and the short-dashed lines, the optical rain gauge paths (50 m each). Solid lines show the flow of micrometeorological data to the data acquisition system in the receiver trailer. Antennas are numbered 1 to 5 in the receiver trailer.

Table 1.--Antenna pairs

Pair number	Antenna pair	Spacing in meters
1	1 & 2	1.43
2	1 & 3	4.29
3	1 & 4	10.00
4	2 & 3	2.86
5	2 & 4	8.57
6	3 & 4	5.71

For each antenna pair, the GIT mm-wave data contain the square of the voltage from four phase shifts of 0° , 90° , 180° , and 270° . For the antenna pair formed by antennas i and j these are denoted by

$$(v_0)_{ij}^2, (v_{90})_{ij}^2, (v_{180})_{ij}^2, \text{ and } (v_{270})_{ij}^2. \quad (1)$$

The data also contain the intensity at each antenna, denoted by I_i for the i th antenna.

It is important to keep in mind that the intensities are measured in arbitrary units and that differences exist between the time-averaged (hereafter referred to as mean) intensities of different antennas. Thus any statistics calculated from the intensities must be normalized by the appropriate mean intensities. Because of hardware characteristics, the phase difference between antenna pairs has an arbitrary offset that is different for each pair. Thus any phase-difference statistics must be calculated from the phase difference with its mean value subtracted.

Drift in the mm-wave receivers causes the measured intensities and squared voltages in (1) to change slowly with time. Thus it is necessary to low-pass filter the mm-wave data; the filter frequency can be varied as needed. We redefine the phase difference as its value with its low-pass-filtered value subtracted. To excellent approximation, the mean phase difference is then zero. We redefine the intensity as its value divided by its low-pass-filtered value. Then, to excellent approximation, the mean intensity is unity. In the following we discuss various statistical quantities for which mean phase differences are subtracted and mean intensities are divided out. One must keep in mind that if the low-pass filtering is used, then a subsequent subtraction of the mean phase difference and scaling by the mean intensity has essentially no effect. However, if the low-pass filtering is not used, then the computer code continues to operate correctly by subtracting the nontrivial mean phase difference, and scaling by the nonunity mean intensities.

2.2 Phase-Difference Statistics

The phase difference for antenna pair i and j is computed using the following:

$$\beta_{ij} = \arctan \left[\frac{(v_{90})_{ij}^2 - (v_{270})_{ij}^2}{(v_0)_{ij}^2 - (v_{180})_{ij}^2} \right] . \quad (2)$$

The Fortran ATAN2 function is used in the computations. This gives β_{ij} in the range $-\pi$ to π . That range is extended to -2π to 2π by following the transition in the value of ATAN2 as the phase difference crosses $-\pi$ or π . It is possible to extend the range to $-\infty$ to ∞ by slightly more complicated programming; this has not been done since it is expected that the range from -2π to 2π will never be exceeded. In any case, we will be aware from microfilm stripcharts if this range is exceeded.

For each antenna pair we calculate mean phase difference $\langle \beta_{ij} \rangle$ and the mean of the squared phase difference $\langle (\beta_{ij})^2 \rangle$ from which we obtain the phase-difference variance

$$\langle (\beta_{ij} - \langle \beta_{ij} \rangle)^2 \rangle = \langle (\beta_{ij})^2 \rangle - \langle \beta_{ij} \rangle^2 . \quad (3)$$

These six variances produce the phase structure function, when graphed as a function of antenna spacing.

2.3 Intensity Statistics

For each antenna, we calculate the mean intensity $\langle I_i \rangle$ and the mean of the squared intensity $\langle I_i^2 \rangle$. From these we obtain the normalized intensity variance

$$\sigma_i^2 = \frac{\langle (I_i - \langle I_i \rangle)^2 \rangle}{\langle I_i \rangle^2} = \frac{\langle I_i^2 \rangle}{\langle I_i \rangle^2} - 1 . \quad (4)$$

For each of the antenna pairs i and j , we calculate the cross-product average $\langle I_i I_j \rangle$; this gives the normalized covariance

$$c_{ij} = \frac{\langle (I_i - \langle I_i \rangle)(I_j - \langle I_j \rangle) \rangle}{\sqrt{\langle (I_i - \langle I_i \rangle)^2 \rangle} \sqrt{\langle (I_j - \langle I_j \rangle)^2 \rangle}} \quad i \neq j \quad (5)$$

or

$$C_{ij} = \frac{\langle I_i I_j \rangle - \langle I_i \rangle \langle I_j \rangle}{\sigma_i \sigma_j \langle I_i \rangle \langle I_j \rangle}. \quad (6)$$

When graphed versus antenna spacing, the six C_{ij} are the normalized spatial covariance. On the basis of inertial-range theory and no absorption fluctuations, the minimum antenna separation of 1.43 m implies that the normalized covariance would be only about 0.1, and be very much smaller at larger separations. Thus the effects of absorption fluctuations might be seen in the large-spacing covariance values because the absorption fluctuations affect much larger spatial scales in the scintillation pattern than do refractive fluctuations.

2.4 Mixed Intensity and Phase-Difference Statistics

For each antenna pair, we calculate the intensity-phase-difference cross-correlations $\langle I_i \beta_{ij} \rangle$ and $\langle I_j \beta_{ij} \rangle$. These are used to obtain the quantity

$$\frac{1}{2} \left\langle \left(\frac{I_i}{\langle I_i \rangle} - \frac{I_j}{\langle I_j \rangle} \right) \beta_{ij} \right\rangle = \frac{1}{2} \left(\frac{\langle I_i \beta_{ij} \rangle}{\langle I_i \rangle} - \frac{\langle I_j \beta_{ij} \rangle}{\langle I_j \rangle} \right). \quad (7)$$

We define the log-amplitude by $\chi_i \equiv \ln(A_i / \langle A_i \rangle)$. Since

$$\langle I \rangle = \langle A^2 \rangle = \langle (A - \langle A \rangle)^2 \rangle + \langle A \rangle^2, \quad (8)$$

and for our case of weak scintillation the amplitude variance is much smaller than the square of the mean amplitude, then $\langle I \rangle \approx \langle A \rangle^2$. So the log-amplitude can be approximated by

$$\chi_i \approx \frac{1}{2} \ln(I_i / \langle I_i \rangle) \quad (9)$$

$$= \frac{1}{2} \ln \left(1 + \frac{I_i - \langle I_i \rangle}{\langle I_i \rangle} \right) \quad (10)$$

$$= \frac{1}{2} \left[\frac{I_i - \langle I_i \rangle}{\langle I_i \rangle} - \frac{1}{2} \left(\frac{I_i - \langle I_i \rangle}{\langle I_i \rangle} \right)^2 + \dots \right]. \quad (11)$$

Therefore, to first order in the smallness of intensity fluctuations relative to their mean, which is an excellent approximation, we have the quantity

$$\langle (\chi_1 - \chi_j) \beta_{1j} \rangle = \frac{1}{2} \left\langle \left(\frac{I_1}{\langle I_1 \rangle} - \frac{I_j}{\langle I_j \rangle} \right) \beta_{1j} \right\rangle . \quad (12)$$

2.5 Second Moment of the Field: The Mutual Coherence Function

Let U_i denote the electromagnetic field at the i th antenna, and let U_j^* denote the field's complex conjugate at antenna j . The second moment of the field, known as the mutual coherence function, MCF, is $\langle U_i U_j^* \rangle$. We do not calculate the case $i = j$ because $\langle U_i U_i^* \rangle = \langle I_i \rangle$ is the average intensity, which is already calculated as in Sec. 2.3. If we write the field as

$$U_i = A_i e^{i\phi_i} \quad (13)$$

where $A_i = \sqrt{I_i}$ is its amplitude and ϕ_i is its phase, then the MCF is

$$\langle U_i U_j^* \rangle = \langle A_i A_j e^{i(\phi_i - \phi_j)} \rangle \quad (14)$$

$$= \langle A_i A_j e^{i(\beta_{1j} - \langle \beta_{1j} \rangle)} \rangle . \quad (15)$$

Here the phase difference is

$$\phi_i - \phi_j = \beta_{1j} - \langle \beta_{1j} \rangle , \quad (16)$$

since β_{1j} from Eq. (2) is the phase difference to within an arbitrary offset, this offset being removed by subtracting $\langle \beta_{1j} \rangle$. The unnormalized MCF is not meaningful because the intensities are known only in arbitrary units. The normalized MCF is denoted by M_2 and is given by

$$M_2 = \frac{\langle U_i U_j^* \rangle}{\sqrt{\langle U_i U_i^* \rangle \langle U_j U_j^* \rangle}} \quad (17)$$

or

$$M_2 = \frac{\langle \sqrt{I_1 I_j} e^{i\beta_{1j}} \rangle}{\sqrt{\langle I_1 \rangle \langle I_j \rangle} e^{i\langle \beta_{1j} \rangle}} . \quad (18)$$

We use the relationship

$$e^{i\beta_{1j}} = \cos(\beta_{1j}) + i \sin(\beta_{1j}) . \quad (19)$$

We then average the real and imaginary parts of the numerator of M_2 ; namely, we calculate the averages of R_{1j} and J_{1j} where

$$R_{1j} \equiv \sqrt{I_1 I_j} \cos(\beta_{1j}) \quad (20)$$

$$J_{1j} \equiv \sqrt{I_1 I_j} \sin(\beta_{1j}) . \quad (21)$$

Note that we must take the sine and cosine of β_{1j} , which itself is an arc-tangent, rather than using identities for trigonometric functions of the arc-tangent because we must use a temporal filter on β_{1j} (see Sec. 4.3) but we must not filter the quantities in (1). The inverse of the denominator of M_2 can be written as $R_D - iJ_D$, where

$$R_D = \cos(\langle \beta_{1j} \rangle) / \sqrt{\langle I_1 \rangle \langle I_j \rangle} \quad (22)$$

$$J_D = \sin(\langle \beta_{1j} \rangle) / \sqrt{\langle I_1 \rangle \langle I_j \rangle} , \quad (23)$$

$$\text{so} \quad M_2 = (\langle R_{1j} \rangle + i \langle J_{1j} \rangle) (R_D - iJ_D) . \quad (24)$$

The normalization of the MCF is performed in real arithmetic; the real and imaginary parts of M_2 are determined from

$$\text{Re}(M_2) = \langle R_{ij} \rangle R_D + \langle J_{ij} \rangle J_D \quad (25)$$

$$\text{Im}(M_2) = \langle J_{ij} \rangle R_D - \langle R_{ij} \rangle J_D \quad (26)$$

The modulus and phase of M_2 are also calculated using

$$r = \{[\text{Re}(M_2)]^2 + [\text{Im}(M_2)]^2\}^{1/2} \quad (27)$$

$$\phi = \arctan[\text{Im}(M_2)/\text{Re}(M_2)] \quad (28)$$

such that

$$M_2 = r e^{i\phi} \quad (29)$$

2.6 Fourth Moment of the Field

Having four receiving antennas allows us to calculate the fourth moment of the field, which is given by

$$\langle U_i U_j^* U_n U_m^* \rangle.$$

If $i = j = n = m$ then $M_4 = \langle I_i^2 \rangle$, which is the mean of the squared intensity and has been calculated in Sec. 2.3. If, for instance, $i = j$ and $n = m$, then the fourth moment becomes $\langle I_i I_n \rangle$, which has also been calculated in Sec. 2.3. Thus, not all possible combinations of i, j, n , and m are of interest. In fact, certain choices of i, j, n , and m merely produce the complex conjugate fourth moment arising from a different choice of indexes or produces the same fourth moment because of multiplicative commutation. Thus we calculate only those fourth moments that are distinct from intensity products and are distinct under complex conjugation and multiplicative commutation. The sets of i, j, n, m that produce these distinct values of M_4 are given in Table 2.

Similar to the case of the second moment of the field, only the normalized fourth moment is meaningful because the intensities are known only in

Table 2.--Indexes for producing distinct values of M_4

Case	i	j	n	m
1	1	2	3	4
2	1	2	4	3
3	1	3	2	4
4	1	1	1	2
5	1	1	1	3
6	1	1	1	4
7	1	1	2	3
8	1	1	2	4
9	1	1	3	4
10	2	2	1	2
11	2	2	1	3
12	2	2	1	4
13	2	2	2	3
14	2	2	2	4
15	2	2	3	4
16	3	3	1	2
17	3	3	1	3
18	3	3	1	4
19	3	3	2	3
20	3	3	2	4
21	3	3	3	4
22	4	4	1	2
23	4	4	1	3
24	4	4	1	4
25	4	4	2	3
26	4	4	2	4
27	4	4	3	4
28	1	2	1	2
29	1	3	1	3
30	1	4	1	4
31	2	3	2	3
32	2	4	2	4
33	3	4	3	4

arbitrary units and the phase differences are known only to within additive constants. The normalized fourth moment is defined by

$$M_4 = \frac{\langle U_i U_j^* U_n U_m^* \rangle}{\sqrt{\langle U_i U_i^* \rangle \langle U_j U_j^* \rangle \langle U_n U_n^* \rangle \langle U_m U_m^* \rangle}} \quad (30)$$

By analogy with the second moment, this gives

$$M_4 = \frac{\langle \sqrt{I_1 I_j I_n I_m} \exp[i(\beta_{1j} + \beta_{nm})] \rangle}{\sqrt{\langle I_1 \rangle \langle I_j \rangle \langle I_n \rangle \langle I_m \rangle} \exp[i(\langle \beta_{1j} \rangle + \langle \beta_{nm} \rangle)]} . \quad (31)$$

In the computation we average the real and imaginary parts of the numerator of M_4 ; namely, we obtain the averages $\langle R_4 \rangle$ and $\langle J_4 \rangle$ where

$$\langle R_4 \rangle \equiv \langle \sqrt{I_1 I_j I_n I_m} \cos(\beta_{1j} + \beta_{nm}) \rangle \quad (32)$$

$$\langle J_4 \rangle \equiv \langle \sqrt{I_1 I_j I_n I_m} \sin(\beta_{1j} + \beta_{nm}) \rangle . \quad (33)$$

For the first case in Table 2, R_4 and J_4 are calculated by noting that

$$R_4 = R_{12} R_{34} - J_{12} J_{34} \quad (34)$$

$$J_4 = J_{12} R_{34} + R_{12} J_{34} \quad (35)$$

where R_{1j} and J_{1j} were previously calculated values of the real and imaginary parts of the instantaneous second moment and are given in Eqs. (20) and (21). The second and third cases in Table 2 are calculated similarly. Cases 4 to 27 in Table 2 have one pair of equal indexes, $i = j$. These are calculated by noting that

$$R_4 = I_1 R_{nm} \quad (36)$$

$$J_4 = I_1 J_{nm} \quad (37)$$

where I_1 is the intensity at antenna 1 (and also j since $i = j$); R_{nm} and J_{nm} are the real and imaginary parts of the instantaneous second moment for the remaining antenna pair as given in Eqs. (20) and (21). Finally, cases 28 to 33 in Table 2 are the squares of instantaneous second moments (since

$n = i$ and $m = j$) and are thus calculated using

$$R_4 = (R_{ij})^2 - (J_{ij})^2 \quad (38)$$

$$J_4 = 2 R_{ij} J_{ij} . \quad (39)$$

The inverse of the denominator of M_4 can be written as $R_{4D} - iJ_{4D}$, where

$$R_{4D} \equiv \cos(\langle \beta_{ij} \rangle + \langle \beta_{nm} \rangle) / d \quad (40)$$

$$J_{4D} \equiv \sin(\langle \beta_{ij} \rangle + \langle \beta_{nm} \rangle) / d . \quad (41)$$

Here

$$d = \sqrt{\langle I_i \rangle \langle I_j \rangle \langle I_n \rangle \langle I_m \rangle} , \quad (42)$$

$$\text{so} \quad M_4 = (\langle R_4 \rangle + i \langle J_4 \rangle) (R_{4D} - iJ_{4D}) . \quad (43)$$

For cases 1 to 3 in Table 2 these definitions of R_{4D} and J_{4D} are used literally. For cases 4 to 27, in which $i = j$, we have $\beta_{ij} = 0$ and $I_i = I_j$, so the following simplified expressions are used:

$$R_{4D} = \cos(\langle \beta_{nm} \rangle) / d \quad (44)$$

$$J_{4D} = \sin(\langle \beta_{nm} \rangle) / d \quad (45)$$

with $d = \langle I_i \rangle \sqrt{\langle I_n \rangle \langle I_m \rangle}$. These trigonometric evaluations and the square root in d are the same as were used in normalizing the second moment, so they need not be computed a second time. For cases 28 to 33 in Table 2, in which $i = j$ and $n = m$, we use

$$R_{4D} = R_D^2 - J_D^2 \quad (46)$$

$$J_{4D} = 2R_D J_D \quad (47)$$

where R_D and J_D are obtained using Eqs. (22) and (23). Finally, the real and imaginary parts of the normalized fourth moment are obtained using

$$\text{Re}(M_4) = \langle R_4 \rangle R_{4D} + \langle J_4 \rangle J_{4D} \quad (48)$$

$$\text{Im}(M_4) = \langle J_4 \rangle R_{4D} - \langle R_4 \rangle J_{4D} \quad (49)$$

2.7 Extrema

For all four antennas, the maximum and minimum observed intensities are obtained. These extremal intensities are normalized by dividing by the mean intensity, because the intensity is measured in arbitrary units. Likewise the maximum and minimum observed phase difference is obtained for each of the six antenna pairs. These extremal phase differences are normalized by subtracting the mean phase difference of the antenna pair, because this mean is an arbitrary offset. Besides being intrinsically interesting, these extrema will take on any greatly erroneous values that appear in the intensities and phase differences. Hence, the extrema reveal erroneous data that are included in all of the other mm-wave statistics described in this report.

2.8 Probability Distribution Functions

We calculate the probability distribution function (PDF) of each of the four intensities. We have control over the range of intensity values included in these PDFs, and foreknowledge of the intensity extrema allows us to efficiently divide the legitimate range of observed values into bins, thereby discarding obviously erroneous data. The PDFs are calculated as histograms by adding unity to the histogram value in a given bin each time the intensity lies within the given bin. These histograms are normalized after the desired amount of data has been included within them. In the same manner we obtain the six phase difference PDFs, one for each antenna pair.

2.9 Fourier Transforms

We calculate the power spectra of each of the four intensities and six phase differences. The computer programs allow us to also calculate cross-

spectra between only two quantities, e.g., between intensities from different antennas, or phase differences from different antenna pairs, or between an intensity and phase difference. By cross-spectra we mean cospectra, quadrature spectra, coherence spectra, or phase spectra of two different quantities.

The fast Fourier transform algorithm is used on 4096-point time series, corresponding to 40.96 s of data. A number of these transforms, nominally 10 of them, are averaged together to increase the statistical reliability. The resulting transforms are combined to produce the aforementioned power and cross-spectra, which are, in turn, each averaged to 36 spectral values in 36 approximately logarithmically spaced frequency bins.

Fourier components of yet lower frequency are obtained by block averaging the time series to 4096 points per data tape (or per time-stationary interval). The data tapes are roughly 2400 s in duration, so averages of roughly 0.6 s suffice. The fast Fourier transforms of these 0.6-s averaged time series are also combined to produce the aforementioned power and cross-spectra and are averaged to 36 logarithmically spaced frequency bins. Finally, these low-frequency spectra are combined with their high-frequency counterparts to form composite spectra having 72 frequency bins. There is adequate spectral overlap between the lowest frequency in the high-frequency part and the highest frequency in the low-frequency part.

2.10 Figures of Merit

Certain redundancies in the mm-wave data make it possible to calculate quantities that would have known values if the measurements were perfect. We call these quantities figures of merit, since their deviations from their ideal values indicate the level of precision in the mm-wave instrumentation.

The first such figure of merit is the ρ type given by

$$\rho^2 \equiv \{[(v_0)_{ij}^2 - (v_{180})_{ij}^2]^2 + [(v_{90})_{ij}^2 - (v_{270})_{ij}^2]^2\} / I_1 I_j . \quad (50)$$

There is one ρ -type figure of merit for each of the six antenna pairs. The ρ type is, in effect, the squared modulus of the MCF of the mm-wave instrumentation. Ideally it would have the value unity at each instant, and its

deviations from unity place a limit on the accuracy of measuring the propagation MCF at each antenna separation. We calculate the mean and central variance for these six ρ -type figures of merit.

The second figure of merit is the Σ type given by

$$\Sigma \equiv [(V_0)_{ij}^2 + (V_{90})_{ij}^2 + (V_{180})_{ij}^2 + (V_{270})_{ij}^2] / (I_i + I_j) . \quad (51)$$

This type, one for each of six antenna pairs, should also be unity at each instant. We calculate the mean and central variance of each of the six Σ 's.

The last figure of merit is an obvious one called the "phase" type. If i , j , and k are three distinct antennas such that the k antenna lies between the i and j antennas, then the phase-difference sum $\beta_{ik} + \beta_{kj} - \beta_{ij}$ should ideally be a constant determined by the arbitrary phase-difference offsets of the antenna pairs. Except for these offsets this phase-difference sum would ideally be zero. Because of these offsets, the mean value of this figure of merit is meaningless, but the variance about the mean is a measure of the precision of the phase-difference measurements. This variance is the phase-type figure of merit. The phase-difference variance from each of β_{ik} , β_{kj} , and β_{ij} should be much larger than this figure of merit, otherwise at least one of the phase differences is suspect. There are four such phase-type figures of merit when the antennas are taken three at a time as above, and one when all four antennas are included. The latter is the variance of $\beta_{12} + \beta_{23} + \beta_{34} - \beta_{14}$. We calculate these five figures of merit.

3. QUANTITIES COMPUTED FROM THE NOAA MICROMETEOROLOGICAL DATA

3.1 Introduction

The NOAA micrometeorological data are obtained at two towers, 3.6 m in height, located adjacent to the propagation path at approximately one-third and two-thirds of the distance from the mm-wave receiver to the transmitter. These are designated as stations 1 and 2 respectively, and are shown on Fig. 1. The two optical paths were located 50 m and 65 m east of the mm-wave path. The micrometeorological towers were 80 m east of the mm-wave path, and the

optical rain gauge/disdrometer paths were 90 m east. Each tower has a three-axis sonic anemometer with a platinum resistance-wire thermometer in the center of the sonic array, a nearby Lyman- α hygrometer with another wire thermometer within its gap, a prop-vane anemometer, and a psychrometer for mean temperature and humidity. The wire thermometers and Lyman- α hygrometer were sampled at 100 Hz. The sonic and prop-vane anemometers were sampled at 25 Hz. Beginning with the 0.39-Hz pulse, the psychrometer gives six commutation cycles repeated at the 25-Hz rate. A commutation cycle consists of data from the wet and dry bulbs and two reference values, four quantities in all. The psychrometer then returns toward thermal equilibrium until the next 0.39-Hz pulse calls for data; this minimizes self-heating in the psychrometer due to power dissipation. Station 2 has a ~~Vaisala~~ mean temperature and humidity instrument sampled at 25 Hz, but the ~~Vaisala~~ readings of humidity are judged inferior to those of the psychrometer. Station 2 included an up-looking pyranometer for solar radiation and cloud-shadow-occurrence measurements, and station 1 included a barometer; these were sampled at 25 Hz. A combined optical C_n^2 and optical cross-wind meter was operated on the path from near the mm-wave transmitter to station 1 and another from near the mm-wave receiver to station 2; these optical paths overlap. Optical rain gauges were deployed near both stations and six weighing bucket rain gauges were deployed along the path. At station 1 the optical rain gauge included a disdrometer. The data from these optical instruments were sampled at 0.39 Hz. The reduction of the data from the rain instruments is not discussed in this report.

Additional optical instrumentation was deployed during the fourth experiment session. A 10.6- μm CO_2 laser, for measurement of infrared C_n^2 in clear air and for phase-difference spectra in rain, was operated from near the mm-wave transmitter to inside the mm-wave receiver trailer. A third large-aperture optical C_n^2 and cross-wind meter was operated over the northern two-thirds of the range directly below its existing counterpart. The purpose was to measure vertical shear of the path-averaged optical cross wind. A He-Ne laser scintillometer and LED scintillometer were deployed over the same short path to measure the inner scale of turbulence by its effect on optical scintillation. At station 1 an up-looking photocell was installed to compare cloud cover measurements with those of the up-looking pyranometer at station 2. In addition, another psychrometer was installed at station 2 to determine the instrument's reliability by comparison with its existing counterpart.

Except for the CO₂ laser, these additional instruments were recording data during the second half of the fifth session as well.

The heights of the instrumentation as well as subjective estimates of the 3 σ errors in the heights are as follows: The mm-wave beam and CO₂-laser beam average 3.68 m \pm 0.1 m; the Lyman- α gap, horizontal sonic transducers, prop-vane, and platinum wires are at 3.61 m \pm 0.05 m; the psychrometer inlets are at 1.91 m \pm 0.05 m; the upper-level optical wind and C_n² meters and the optical inner-scale meter are at 3.78 m \pm 0.1 m; and the lower-level optical wind and C_n² meter are 2 m \pm 0.02 m below the upper-level meters.

3.2 Conversion to Units

Unlike the mm-wave data, the micrometeorological data must be converted to physical units like degrees Celsius or meters per second. This conversion depends on mean temperature for the sonic anemometers and on mean humidity for the Lyman- α hygrometers. The 0.39-Hz data is converted to units giving a datum from each instrument every 2.56 s. The middle four of the six commutation cycles from the psychrometer are averaged to provide wet- and dry-bulb temperatures at the 0.39-Hz rate. The temperatures from the platinum resistance-wire thermometers and the voltage counts from the Lyman- α hygrometers are averaged over 2.56-s bins to determine their trends. Comparison of these Lyman- α voltage counts averaged over the entire tape with the similarly averaged psychrometer humidity establishes the Lyman- α calibration.

The resistance-wire signals are converted to degrees Celsius and Lyman- α signals are converted to absolute humidity in grams of water vapor per cubic meter, all at their 100-Hz data rate. The prop-vane signals are converted at their 25-Hz data rate to wind speed in meters per second and angle in degrees. This wind angle is zero if the wind is perpendicular to the front of the instrument boom and increases if the vane turns clockwise as viewed from below. The wind components along the sonic axes are converted to meters per second, at their 25-Hz rate. The solar pyranometer output is expressed as a fraction of full sun (1.395 W/m²) at its 25-Hz rate. The barometer signal is converted to millibars at its 25-Hz rate.

The angle between the horizontal sonic axes is 120° to allow a greater acceptance of wind angle variation. Consequently the measured horizontal

sonic wind components are not orthogonal. Our sonic configuration is shown by Kaimal (1980a; Figs. 2 and 3). Orthogonal components are obtained from the nonorthogonal ones such that the u -component is perpendicular to the instrument boom and is positive when the wind is toward the boom and the v -component is parallel to the boom, and is positive when the wind is blowing right to left of a person facing the boom. If we let V_A and V_B denote the wind components along the "A" and "B" sonic axes as depicted by Kaimal (1980a; Figs. 2 and 3), then u and v are given by

$$u = V_A + V_B \quad (52)$$

$$v = (V_B - V_A)/\sqrt{3} . \quad (53)$$

The vertical axes of the sonic anemometer are maintained to within 0.1° of vertical so that the measured vertical wind component, w , is negligibly contaminated by horizontal wind fluctuations. The u , v , and w components then form a right-handed orthogonal triad. Although the boom is rotated into the wind at the beginning of each data run, there remains a slight difference between our notation for u , v , w and the standard micrometeorological notation that the u -component is along the time-averaged direction of the wind (i.e., it is the streamwise component) and that v is the cross-stream component.

Angle encoders at both meteorological towers give the angle of the instrument boom relative to geographic directions. These encoders give angles changing from 0° to 90° , to 180° , to 270° as the boom rotates from facing north to facing east, to facing south, to facing west (N, E, S, W), respectively. (As a result of an error, these encoder angles are for directions W, N, E, S for the first two data tapes of the third experiment session.) We define the geographic wind angle as the encoder angle minus the prop-vane angle. As mentioned before, the vane angle is relative to the boom; it increases clockwise when one looks up at the boom from below, and is zero for wind blowing into the face of the boom. The geographic wind angle is then 0° , 90° , 180° , and 270° for wind blowing from the N, E, S, and W, respectively. (Except for the first two data tapes of the third experiment session when these angles are for wind from the W, N, E, and S, respectively.) The optical cross wind telemetered from station 1 is obtained over the southern two-thirds of the mm-wave range and is positive for wind from the east. The optical cross wind telemetered from station 2 is obtained over the northern two thirds of the range and is positive for wind from the west.

3.3 Averages, Variances, and Cross-Correlations

Table 3 lists the averages performed in each computation. An average is denoted by the angle brackets. The symbols for the quantities are as follows: q is the Lyman- α humidity in grams per cubic meter; T_L is the temperature in Celsius from the resistance wire within the Lyman- α gap; T_S is the temperature in Celsius from the resistance wire within the sonic anemometer; u , v , w are the orthogonalized sonic anemometer wind components in meters per second as discussed in Sec. 3.2; V and θ are the prop-vane wind speed in meters per second and angle in degrees, respectively; S is the pyranometer solar flux.

Table 3.--Kinds of averages performed on the NOAA micrometeorological data

Averages	$\langle q \rangle$, $\langle T_L \rangle$, $\langle T_S \rangle$, $\langle u \rangle$, $\langle v \rangle$, $\langle w \rangle$, $\langle V \rangle$, $\langle \theta \rangle$, $\langle \sqrt{u^2 + v^2} \rangle$, $\langle S \rangle$
Mean squares	$\langle q^2 \rangle$, $\langle T_L^2 \rangle$, $\langle T_S^2 \rangle$, $\langle u^2 \rangle$, $\langle v^2 \rangle$, $\langle w^2 \rangle$, $\langle V^2 \rangle$, $\langle \theta^2 \rangle$, $\langle u^2 + v^2 \rangle$, $\langle S^2 \rangle$
Cross-correlations	$\langle u w \rangle$, $\langle v w \rangle$, $\langle u v \rangle$, $\langle q w \rangle$, $\langle T_L w \rangle$, $\langle T_S w \rangle$, $\langle q T_L \rangle$, $\langle q T_S \rangle$, $\langle T_L T_S \rangle$, $\langle \sqrt{u^2 + v^2} w \rangle$

Note: See text for an explanation of the symbols.

The averages listed in Table 3 are obtained for both micrometeorological stations. In the case of cross products like $\langle T_S w \rangle$, which have a 100-Hz quantity, T_S , multiplied by a 25-Hz quantity, w , we average four consecutive values of the 100-Hz quantity before performing the product and including the term in the summation.

The mean squares and cross-correlations given in Table 3 are not of interest in themselves. After the averaging is completed the mean squares are converted to variances taken about the mean (centralized variances) and the cross-correlations are likewise converted. The following equations give the

desired central moment on the left side and the required calculation on the right side. For the variances, where Q may be w , u , v , V , T_S , T_L , or q , we use

$$\langle (Q - \langle Q \rangle)^2 \rangle = \langle Q^2 \rangle - \langle Q \rangle^2 . \quad (54)$$

For the centralized cross-correlations, where the pair Q_1, Q_2 may be u, w or v, w or u, v or q, w or T_L, w or T_S, w or T_L, q , we use

$$\langle (Q_1 - \langle Q_1 \rangle)(Q_2 - \langle Q_2 \rangle) \rangle = \langle Q_1 Q_2 \rangle - \langle Q_1 \rangle \langle Q_2 \rangle . \quad (55)$$

We subtract the mean of quantities like w , which should have a zero mean value, because instrumental offsets cause the measured values to have nonzero means, and these offsets must be subtracted.

3.4 Turbulence Fluxes

All of the quantities discussed in this section are obtained from averages previously performed. The correlations discussed in the previous section form the basis for the calculation of the fluxes.

The quantities $\langle (T_S - \langle T_S \rangle)(w - \langle w \rangle) \rangle$ and $\langle (q - \langle q \rangle)(w - \langle w \rangle) \rangle$ are the vertical fluxes of temperature and humidity, respectively. Temperature flux can be converted to heat flux by multiplying by the constant-pressure heat capacity of air, and humidity flux can be converted to latent heat flux by multiplying by the latent heat of vaporization. The above temperature flux is obtained by correlating the fluctuating temperature from the resistance-wire thermometer within the sonic array with the fluctuating vertical velocity from the sonic anemometer. The Lyman- α hygrometer is spatially separated from the sonic array so that it does not disturb the turbulent wind field at the array. The spatial separation slightly reduces the humidity flux from its true value. However, we also calculate the temperature flux using the resistance wire within the Lyman- α gap from the cross-correlation $\langle T_L w \rangle$. The ratio of the two temperature fluxes,

$$\langle (T_L - \langle T_L \rangle)(w - \langle w \rangle) \rangle / \langle (T_S - \langle T_S \rangle)(w - \langle w \rangle) \rangle , \quad (56)$$

is a correction factor for this spatial separation. Because of the high correlation and/or anticorrelation between temperature and humidity fluctu-

tuations, the humidity flux can be multiplied by this ratio to correct it for the spatial separation.

To obtain the vertical flux of horizontal momentum we must cross-correlate fluctuating vertical wind speed with the fluctuating horizontal wind component along the time-averaged wind direction (the streamwise component). Given the mean wind angle $\langle\theta\rangle$ from either the vane or sonic anemometer, the streamwise component u_θ and cross-stream component v_θ are given in terms of the u and v components by

$$u_\theta = u \cos\langle\theta\rangle + v \sin\langle\theta\rangle \quad (57)$$

$$v_\theta = -u \sin\langle\theta\rangle + v \cos\langle\theta\rangle . \quad (58)$$

Letting primes denote zero-mean fluctuations, e.g., $u_\theta' = u_\theta - \langle u_\theta \rangle$ and $v' = v - \langle v \rangle$, then we have

$$u_\theta' = u' \cos\langle\theta\rangle + v' \sin\langle\theta\rangle \quad (59)$$

$$v_\theta' = -u' \sin\langle\theta\rangle + v' \cos\langle\theta\rangle . \quad (60)$$

The vertical momentum flux is given by multiplying the quantity

$$\langle u_\theta' w' \rangle = \langle u' w' \rangle \cos\langle\theta\rangle + \langle v' w' \rangle \sin\langle\theta\rangle \quad (61)$$

by the mass density of the air. Calculation of the quantities

$$\langle u' w' \rangle = \langle u w \rangle - \langle u \rangle \langle w \rangle \quad (62)$$

and

$$\langle v' w' \rangle = \langle v w \rangle - \langle v \rangle \langle w \rangle \quad (63)$$

has already been discussed in the previous section. The vertical flux of cross-stream momentum

$$\langle v_\theta' w' \rangle = -\langle u' w' \rangle \sin\langle\theta\rangle + \langle v' w' \rangle \cos\langle\theta\rangle , \quad (64)$$

and the horizontal flux of momentum obtained from

$$\langle u_{\theta}' v_{\theta}' \rangle = 1/2(\langle v'^2 \rangle - \langle u'^2 \rangle) \sin(2\langle \theta \rangle) + \langle u' v' \rangle \cos(2\langle \theta \rangle) \quad (65)$$

should both be zero for a horizontally homogeneous surface layer, but they are computed anyway. In addition, for station 2 we calculate the speed flux given by

$$\langle (\sqrt{u^2 + v^2} - \langle \sqrt{u^2 + v^2} \rangle) (w - \langle w \rangle) \rangle = \langle \sqrt{u^2 + v^2} w \rangle - \langle \sqrt{u^2 + v^2} \rangle \langle w \rangle. \quad (66)$$

We can calculate the momentum flux using (61) in a variety of ways depending on how we choose $\langle \theta \rangle$. We could, for instance, take $\langle \theta \rangle$ to be the average of the vane angles. The conventional method is to set the average cross-stream component to zero, i.e., $\langle v_{\theta} \rangle = 0$, so from (58) $\langle \theta \rangle = \arctan(\langle v \rangle / \langle u \rangle)$ as given by Kaimal (1980a). However, this $\langle \theta \rangle$ is sensitive to the poorly-known offset voltages of the sonic anemometer. On the other hand, we can assume a horizontally homogeneous surface layer and set $\langle v_{\theta}' w' \rangle = 0$ in (64) to define $\langle \theta \rangle$; this definition of $\langle \theta \rangle$ is independent of sonic offset voltages. Using this latter $\langle \theta \rangle$, (61) gives for the momentum flux

$$\langle u_{\theta}' w' \rangle = \sqrt{\langle u' w' \rangle^2 + \langle v' w' \rangle^2}.$$

This result is independent of sonic offset voltages, but depends on horizontal homogeneity. We calculate this latter momentum flux, but we also use the mean vane angle to calculate the expressions in (61), (64), and (65).

3.5 Spatial Structure Parameters

The spatial separation of the two resistance-wire thermometers and of the Lyman- α hygrometer and the resistance wire within the sonic anemometer enable us to calculate temperature structure parameters and temperature-humidity cross-structure parameters. The temperature structure parameter is given by

$$C_T^2 = \langle (T_S' - T_L')^2 \rangle / r_{SL}^{2/3} \quad (67)$$

$$= (\langle T_S'^2 \rangle - \langle T_S \rangle^2 + \langle T_L'^2 \rangle - \langle T_L \rangle^2 - 2\langle T_S T_L \rangle + 2\langle T_S \rangle \langle T_L \rangle) / r_{SL}^{2/3} \quad (68)$$

where primes denote zero-mean fluctuations and r_{SL} is the distance between the resistance-wires in the sonic anemometer and the Lyman- α gap. The second formula (68) shows that this structure parameter can be calculated from quantities already discussed in Sec. 3.3.

If we had additional Lyman- α hygrometers positioned within the sonic anemometer yielding fluctuating humidities q_S' , then we could calculate the temperature-humidity cross-structure parameter defined by

$$C_{Tq} = \langle (T_S' - T_L')(q_S' - q') \rangle / r_{SL}^{2/3}. \quad (69)$$

However, if we assume that this hypothetical hygrometer would give $\langle T_S' q_S' \rangle = \langle T_L' q' \rangle$ and $\langle T_S' q' \rangle = \langle T_L' q_S' \rangle$ (the latter requires horizontal isotropy), then we have

$$C_{Tq} = 2(\langle T_L' q' \rangle - \langle T_S' q' \rangle) / r_{SL}^{2/3} \quad (70)$$

$$= 2(\langle T_L q \rangle - \langle T_L \rangle \langle q \rangle - \langle T_S q \rangle + \langle T_S \rangle \langle q \rangle) / r_{SL}^{2/3}, \quad (71)$$

where (71) shows that the calculation obtains from quantities already discussed in Sec. 3.3.

3.6 Time-Lagged Structure Parameters

The time-lagged structure parameters of temperature, C_T^2 , humidity, C_q^2 , C_q^2 , and the temperature-humidity cross-structure parameter, C_{Tq} , are defined by

$$C_{T_S}^2 = \langle [T_S(t) - T_S(t + \tau)]^2 \rangle / (\langle V \rangle \tau)^{2/3}, \quad (72)$$

$$C_{T_L}^2 = \langle [T_L(t) - T_L(t + \tau)]^2 \rangle / (\langle V \rangle \tau)^{2/3}, \quad (73)$$

$$C_q^2 = \langle [q(t) - q(t + \tau)]^2 \rangle / (\langle V \rangle \tau)^{2/3}, \quad (74)$$

$$C_{T_L q} = \langle [T_L(t) - T_L(t + \tau)][q(t) - q(t + \tau)] \rangle / (\langle V \rangle \tau)^{2/3}, \quad (75)$$

where t is time, τ is time lag, and $\langle V \rangle$ is the average wind speed. The data are digitized at 100 Hz, so τ must be a multiple of 0.01 s. Let the height above ground be denoted by Z , then $Z/5$ should be in the inertial range of

sizes. We define a dimensionless factor by

$$F \equiv (Z/5)(100 \text{ samples/s})/\langle V \rangle . \quad (76)$$

We then define three integers $J_1 = F$, $J_2 = F/2$, and $J_3 = F/4$, where the integers are rounded up from the real numbers. These integers are the number of 0.01-s data samples to skip to calculate the above four structure parameters for both stations at three values of time lag. The time lags used are thus $\tau_1 = J_1(0.01 \text{ s})$, $\tau_2 = J_2(0.01 \text{ s})$, and $\tau_3 = J_3(0.01 \text{ s})$; these correspond approximately to spatial lags of $Z/5$, $Z/10$, and $Z/20$. The integers and lags can be different at the two stations because $\langle V \rangle$ can differ between the stations.

Of course, the time-lagged structure parameters and cross-structure parameters can also be obtained from the spectral level of the appropriate power spectra and cospectra, which are discussed in Sec. 5.9.

3.7 Extrema

We obtain the minimum and maximum observed values of several quantities for each averaging period. These quantities are the wind speed and wind angle from the prop-vane anemometer and the solar flux from the pyranometer.

3.8 Probability Distribution Functions

The probability distribution functions (PDFs) are calculated for the pyranometer solar flux and the wind angles from the two prop-vane anemometers. The joint probability distribution functions (JPDFs) of Lyman- α humidity and its associated resistance-wire temperature is calculated for both stations. The PDFs of the fluctuating humidity or temperature can be obtained by summing the JPDF over all temperature or humidity bins, respectively. These PDFs obtained from JPDFs are sometimes called marginal PDFs. Since for clear air the fluctuations of real and imaginary parts of the refractive index depend almost entirely on only temperature and humidity fluctuations, we can obtain the JPDF of these real and imaginary parts from the temperature-humidity JPDF.

Of course, the marginal PDFs of refraction and absorption can be obtained from this latter JPDF as well.

The method of calculating these PDFs and JPDFs as histograms using foreknowledge of the extrema to divide efficiently the data into bins is the same as was discussed for the mm-wave PDFs in Sec. 2.8.

3.9 Fourier Transforms

We calculate the power spectra of the fluctuating temperature and humidity from the resistance-wires and the Lyman- α hygrometer, as well as the temperature-humidity cospectra and quadrature spectra from these instruments. We also calculate the power spectra of all three orthogonalized components of the fluctuating wind from the sonic anemometers, as well as the cospectra and quadrature spectra of these components taken in pairs. The cospectra and quadrature spectra are calculated for temperature and vertical velocity, and for humidity and vertical velocity.

The fast Fourier transform (FFT) algorithm is used on 4096-point time series. This corresponds to 40.96 s of data if only 100-Hz quantities are involved or 163.84 s of data if at least one quantity is of the 25-Hz sampling rate. A number of these FFTs are averaged together, nominally 10 of them, to increase the statistical reliability. As with the mm-wave Fourier transforms, the FFTs are combined to produce power spectra and cross-spectra that are similarly averaged into 29 logarithmically spaced frequency bins.

3.10 Refraction and Absorption Structure Parameters

The zero-mean fluctuations in the real and imaginary parts of the refractive index, denoted n_R' and n_I' , respectively, are related to those of temperature and humidity by

$$n_R' = \frac{A_T}{\langle T \rangle} T_L' + \frac{A_q}{\langle q \rangle} q' \quad (77)$$

$$n_I' = \frac{B_T}{\langle T \rangle} T_L' + \frac{B_q}{\langle q \rangle} q' \quad (78)$$

where $\langle T \rangle$ is the mean Kelvin temperature, the effects of pressure fluctuations are neglected, and these equations are valid for fluctuations much smaller than the means. The dimensionless sensitivity coefficients A_T , A_q , B_T , and B_q depend on mean temperature, humidity, pressure, and the electromagnetic wave length; they are calculated from the radio-frequency refractive-index equation, as well as the sum of dispersion and absorption contributions from water vapor and oxygen resonances, oxygen and nitrogen nonresonant absorption, and the water vapor anomalous absorption. The computer programs for this calculation are not discussed here.

Equations (77) and (78) provide statistics of refraction and absorption from those of temperature and humidity. For instance, the refractive-index structure parameters are given by

$$C_{n_R}^2 = \frac{A_T^2}{\langle T \rangle^2} C_{T_L}^2 + \frac{A_q^2}{\langle q \rangle^2} C_q^2 + \frac{2A_T A_q}{\langle T \rangle \langle q \rangle} C_{T_L q} \quad (79)$$

$$C_{n_I}^2 = \frac{B_T^2}{\langle T \rangle^2} C_{T_L}^2 + \frac{B_q^2}{\langle q \rangle^2} C_q^2 + \frac{2B_T B_q}{\langle T \rangle \langle q \rangle} C_{T_L q} \quad (80)$$

$$C_{n_R n_I} = \frac{A_T B_T}{\langle T \rangle^2} C_{T_L}^2 + \frac{A_q B_q}{\langle q \rangle^2} C_q^2 + \frac{A_T B_q + A_q B_T}{\langle T \rangle \langle q \rangle} C_{T_L q} \quad (81)$$

If these structure parameters are replaced by their corresponding power spectra and cospectra, then these equations give the power spectra and cospectra of refraction and absorption in terms of those of temperature and humidity. Likewise, by analogous replacement, these equations express the variances and cross-correlations of refraction and absorption in terms of those of temperature and humidity.

Clearly, all the relevant statistics of refraction and absorption fluctuations can be obtained from the already-calculated micrometeorological statistics once the sensitivity coefficients are known. In particular, the linear relationships (77) and (78) make it easy to calculate the joint probability distribution function of n_R' and n_I' from that of fluctuating temperature and humidity.

4. PROBLEMS WITHIN THE DATA

4.1 Introduction

The greatest fraction of personnel time expended on the data processing software has been used to fix problems in the data. The discovery and diagnosis of these problems has been challenging and time consuming. During the July 1983 session, the data acquisition system dropped occasional bytes, dropped data frames of 0.01-s duration as well as entire blocks of data of 0.16-s duration, and wrote parity errors on the data tapes. The acquisition system was modified for subsequent sessions. The mm-wave data contain the expected data dropouts during periods of phase-lock loss, but they also contain occasional spikes, step changes in signal gain, harmonic noise due to vibration of the steel I-beam holding the receivers, and other noise of unknown origin. During the first session, the intensity at antenna 4 is incorrect. The micrometeorological data had several instrument failures during that session. The Lyman- α hygrometer at station 1 was not working; one of the optical wind and C_n^2 meters was not working; the resistance-wire thermometer signals exhibited cold spikes and hot spikes that are characteristic of contamination of the wire by hygroscopic particles; and the sonic anemometer signals contained numerous spikes (one per several seconds per channel). Most of these problems have been solved by clever but time-consuming software development.

4.2 Cures for Data Acquisition Errors

A data frame is the digitized data from all instruments in each one-hundredth of a second. The first byte in each frame is synchronization (sync) information. It was found that some of these sync bytes are missing from the data tape. Since the sync bytes should arrive with every frame, it was possible to insert the missing byte when the data tapes were rewritten for our data processing computer.

Entire data frames were found to be missing with no gap in frame sync bytes. The first experiment session had a 10-Hz clock written to tape, so precise frame loss detection is impossible. The 25-Hz data are written to tape by repeating the same value four times for each 25-Hz channel; missing

data frames manifest themselves by fewer than four repetitions of 25-Hz data. A special flag is set to unity in the first data frame of this 25-Hz repetition and set to zero for the last three frames in the repetition. Using this special flag it is possible to identify how many frames are missing, assuming not more than three frames were lost. We then replace the missing frame or frames by duplicating the frame preceding the occurrence of lost frames and setting the special flags when necessary. This restores the integrity of the 25-Hz and 0.39-Hz data and the temporal continuity of the data. Beginning with tape 12 of session 2 through session 5, the lost frame detection is much easier since the 100-Hz clock channel shows each frame that is out of sequence. Changes in the data acquisition system for runs after the tape 12 of session 2 have apparently stopped the frame-loss problem.

The data acquisition system writes data to magnetic tape one block at a time; a block consists of 16 frames, i.e., 0.16 s of data. During session 1, if the read-after-write check failed, then the block was rewritten on tape. The time consumed in the rewrite caused the next block of data to be lost. Thus entire data blocks are missing from session 1 data tapes. The rewrite was disabled for subsequent experiment sessions to avoid this block-loss mechanism. We cannot recreate lost blocks. However, their approximate positions on the data tapes can be identified using the system time (accurate to 0.1 s in session 1 and 0.01 s in subsequent sessions) that is written into each frame. The positions of these lost blocks are written to the "pedigree" disk file so that these data gaps can be avoided during Fourier transformation. So far, no block losses have been found following changes in the data acquisition system that were implemented just before tape 12 of session 2.

The data acquisition system wrote parity errors onto the data tapes. Roughly one-half of all data tapes contain a parity error. By turning off the error processing, we can read the data tape in an unsafe mode. To date this has been tried on only two data tapes. The problem of the parity errors exists in all five experiment sessions.

4.3 Cures for Millimeter-Wave Data Problems

All 28 mm-wave channels require a correction as a result of nonlinearity of the detectors. (The crystal detectors in the signal combiner are not

perfect-square-law detectors in the radio-frequency power regime used.) The extent of nonlinearity was measured for each of the 28 channels and fitted by a polynomial. In the data analysis each datum for each mm-wave channel and for every 0.01 s was corrected by evaluating a fourth-order polynomial (roughly 7 million polynomial evaluations per data tape). One set of polynomial coefficients is used for session 1, another set for session 2 through tape 10 of session 3, and yet another set thereafter. This is necessary because different RF input power was used.

The intensity at antenna 4, I_4 , was not measured during session 1 because of a hard-wiring error. Fortunately, the redundancy in the mm-wave data allows us to calculate I_4 as follows. If ρ^2 in Eq. (50) is obtained from an antenna pair including antenna 4, then setting $\rho^2 = 1$ allows us to calculate I_4 from the other channels. Likewise setting $\Sigma = 1$ in Eq. (51) gives the same result. We wrote a separate computer program to evaluate these methods of synthesizing an intensity. The program compared the normalized variance of the three intensities I_1 , I_2 , and I_3 with their synthesized values from every relevant antenna pair as well as averages of the synthetic intensities over every combination of such antenna pairs. We determined that setting $\Sigma = 1$ produced better results than setting $\rho^2 = 1$ and that averaging the synthesized intensities improved the reliability. For the test case the difference between normalized variances from measured and synthesized intensities ranged from 13.5% to a few tenths of a percent for the $\Sigma = 1$ method, and the normalized variance from the synthesized I_4 was 17% smaller than that from I_1 , I_2 , and I_3 . There is no guarantee that such good results will be obtained from all of session 1 data tapes. At present we use the $\Sigma = 1$ method to synthesize three values of I_4 from the three antenna pairs containing antenna 4 and average these three I_4 values together to produce I_4 for each 0.01-s data frame.

The mm-wave data contain trends that have no correspondence to meteorological trends, nor do the trends in one mm-wave channel appear related to trends in other channels. These trends are apparently caused by drift in receiver gains. Consequently we filter the four intensities and six phase differences using single-pole digital low-pass filters having a roughly 125-s time constant. The filter value is subtracted from the phase differences but divided into the intensities. We retain the unfiltered mean value of the four

intensities. (The figures of merit are obtained from unfiltered data.) However, this filtering requires that we discard about 5 min of data from the beginning of each data tape to initialize the filter.

The mm-wave data contain the expected periods of phase-lock loss. These are of variable duration but typically less than 20 s. There are a variety of types of these data dropouts. The mildest type appears to have intact data, but the intensity drops to half its usual value. The most severe type reduces all mm-wave channels to noise. We detect these phase-lock-loss periods visually using computer-generated microfilm stripcharts. We note the beginning and ending times of each such loss on these stripcharts and enter them in the parameters file for use in subsequent processing. Thus we can exclude the phase-lock losses from subsequent processing. This greatly complicates our programming because we must archive the beginning and ending times, determine what averaging intervals contain such a loss, determine whether or not the loss extends across the boundary of an averaging interval, keep account of the number of samples averaged in each interval, avoid the intervals in the high-frequency FFT, and replace the data with fake values for both the digital filtering and low-frequency FFT.

The mm-wave data also occasionally contain spurious spikes of unknown origin in one or several channels. Sometimes these spikes come in groups of many randomly spaced spikes. We identify these spikes from the microfilm stripcharts and note the time interval containing the spike. We then treat the interval as a phase-lock loss and exclude all mm-wave data in this interval from the data processing. This creates the same complications for our processing as do the phase-lock loss periods. A sophisticated "despiker" algorithm could be used to salvage more data.

On some data tapes, one or more mm-wave channels will exhibit a step change occurring in a time less than 0.01 s. Later, other such step changes may occur, either in the same direction or the opposite. At present we are not processing the data tapes containing this type of error.

Most of the mm-wave data contain noise. One source of noise is harmonic vibration of the steel I-beam that supports the mm-wave receivers. This noise tends to come and go and may be generated by wind gusts stressing the receiver semitrailer, which transmits the stress to the ground and then to the I-beam

supports. The differential motion of parts of the I-beam toward and away from the transmitter causes an artificial phase difference. The most common and largest amplitude of this type of noise is at roughly 5 Hz. Higher frequencies have also been observed. A form of noise in the phase differences that does not seem to be caused by I-beam vibration is a roughly 24-Hz oscillation modulated by a roughly 3-Hz oscillation giving a popcorn-on-a-string effect. This noise can cover entire data runs and persist from one run to another. Even higher frequency noise sometimes appears in intensities as well as in phase differences. The mm-wave Fourier transform is used to identify the frequencies and bandwidths of these noise types. Time-domain convolution filters are used on the time series of the four intensities and six phase differences. Low-pass filtering is especially effective on the phase differences. For any one of the 10 time series there may be one, none, or several such filters acting on different frequencies with different bandwidths.

4.4 Cures for Micrometeorological Data Problems

For those instruments that are not functioning properly during a data run or session, we simply process their signal anyway. It is then necessary to ignore the reduced data from these instruments when the averaged results are interpreted. In session 1, this is the case with the Lyman- α hygrometer at station 1 as well as with one of the optical wind and C_n^2 meters. The wet bulb in the psychrometer at station 1 is dry over most of session 1.

The platinum resistance-wire thermometers have numerous cold and hot spikes that have the same signature as those observed in the marine surface layer by Schmitt et al. (1978). These are particularly evident in session 1. In the marine case the wires rapidly become contaminated by salt spray; the hygroscopic nature of the sodium chloride causes random evaporative cooling and condensative heating of the wire because the fluctuating humidity continually drives the adhering salt-water solution away from equilibrium. We hypothesize that our signals are contaminated by some hygroscopic particles adhering to our wires. This effect has never before been observed in over-land data. We cannot test this hypothesis because the experiment session ended before the effect was observed. However, considering only session 1 data, it is a plausible hypothesis because of the high relative humidities (above 85%) and the close similarity of the signal to that observed for salt-spray-

contaminated data. We do not know the source of hygroscopic aerosol, but we speculate that it may be related to fertilization of the soil or herbicide spraying or washing of the wires in a weak solution of baking soda during manufacture. Field tests were conducted during session 4 under high humidity conditions, but the effect did not reappear during the test. In session 2 the electronics were tested as a source of these spikes but found not to be at fault. However, the hot and cold spikes were present in data taken during session 2.

The cold- and hot-spike phenomenon has serious consequences for our statistics. As shown by Schmitt et al. (1978), temperature structure parameters and heat fluxes are seriously overestimated in marine surface-layer data. The effects are spectrally broad so that simple digital filtering will not help. In effect, the resistance-wire signal is responding to a combination of the air temperature variation and the time-derivative of the humidity. In the future we will examine whether or not this effect can be parameterized. If so, then it may be possible to use the temporal derivative of humidity from the Lyman- α hygrometer to correct the temperature signal from the resistance wire that is within the Lyman- α gap. Such a correction will be a run-by-run, trial-and-error approach based on the parameterization having variable parameters. In the mean time we calculate contaminated statistics with a cautionary note as to their accuracy.

There are occasional spikes in one or more of the 100-Hz channels that are of electronic origin unrelated to the above-mentioned signal contamination. We observe these on computer-generated microfilm stripcharts and note times immediately preceding and following these spikes. The data processing then skips all of the given station's 100-Hz and 25-Hz data within the interval defined by these noted times. This is the same procedure as was used for the mm-wave processing, and it imposes the same complications on the processing software.

During experiment sessions 1 and 2, all three axes of both sonic anemometers produced numerous spikes that were triggered by power-line noise and sonic electronics that were excessively sensitive to such effects. These spikes occurred at a rate of roughly one per several seconds per sonic axis. Their occurrences and strengths are random and sometimes coincident in several axes. Fortunately, in almost all cases a spike consists of only one erroneous

datum. A despiking subroutine has been written that recognizes the spikes by the sudden change of signal, first in one direction then in the other, that exceeds a threshold set at 1 standard deviation of the time series. This threshold was chosen by trial and error. If the standard deviation of the despiked data differs significantly from that of the original data, then the despiking is repeated. This procedure removes the spikes and has very little effect on the data. Of many thousands of spikes removed, only four double-datum spikes of relatively low amplitude remain in the data of session 1. Although the despiking subroutine can remove double-datum spikes by first averaging the data in temporally adjacent pairs, these few remaining spikes are judged to be too insignificant for this procedure. Moreover, the remaining spikes can be excluded from the data processing by previously discussed methods. The problem of the sonic spikes is thus solved.

The existence of sonics spikes prohibited nulling of the sonic electronics in the field for sessions 1 and 2. Normally this null calibration produces zero signal from the sonics when the axes are covered so that no wind is present. Thus all the sonic axes have offset wind readings amounting to as much as ± 0.6 m/s per axis. This is not a problem for the vertical axes, because we subtract $\langle w \rangle$ for all of our calculated statistics involving w , and the vertical axes were maintained within 0.1° of vertical, so horizontal wind fluctuations negligibly contaminate the measured vertical fluctuations. The offset is serious for the horizontal axes. Fortunately there is an adjacent prop-vane anemometer with which to compare wind readings, so the offset can be measured.

Take the sonic A component as an example. The true sonic A component, A_t , is given in terms of the measured and despiked A component, A_m , and the offset O_A by

$$A_t = (A_m - O_A) K^{-1}, \quad (82)$$

where K is the wake correction factor given by Kaimal (1980b). The inverse of K appears on the right side of (82) because Kaimal defines K as the ratio of measured to true sonic components. Also, K is a function of the angle between the wind vector and the sonic arm. We would like to calculate the A component from the prop-vane anemometer, A_p , and require that $\langle A_p \rangle = \langle A_t \rangle$. However, we do not a priori know the sonic-derived angle between the wind vector and the

sonic arm because of the offset. Thus we cannot make the wake correction to A_m or eliminate data when the wind is outside of the $\pm 45^\circ$ acceptance angle. Instead, we average (82), eliminating data when the vane angle is outside the $\pm 45^\circ$ acceptance angle, and similarly average A_p . Replacing $\langle A_t \rangle$ by $\langle A_p \rangle$, we have from (82),

$$\langle A_p \rangle = \langle A_m K^{-1} \rangle - O_A \langle K^{-1} \rangle, \quad (83)$$

wherein K is calculated using the vane angle to infer the angle between the wind vector and sonic arm. The offset is obtained from (83):

$$O_A = (\langle A_m K^{-1} \rangle - \langle A_p \rangle) / \langle K^{-1} \rangle. \quad (84)$$

To obtain O_A , we thus calculate the three averaged quantities in (84) using the vane angle for both K and the $\pm 45^\circ$ acceptance-angle criterion. Equation (84) is not exact, but it need only be a good statistical approximation. We have had excellent results using (84). That is, using (84) for O_A in (82) and the analogous calculation for the B sonic component, we then obtain the angles between the wind vector and sonic arms from the sonic data. We use this sonic-derived angle to determine both K and the $\pm 45^\circ$ acceptance-angle criterion. The resulting A_t gives $\langle A_t \rangle = \langle A_p \rangle$ to excellent approximation. The simpler method of setting $K = 1$ in (84) and not eliminating any data based on the acceptance-angle criterion gives poorer results.

5. OVERVIEW OF THE DATA PROCESSING SOFTWARE

5.1 Introduction

As mentioned in Sec. 1, the data processing software is designed to produce answer files that do not limit interpretation of the data, to cure aforementioned problems within the data, and to produce graphic visualization of data validity at several steps in the processing. The first step is to make a copy of each data tape using a PDP-11/70 computer. This protects the original data tape from being destroyed or altered in subsequent use. The remainder of processing is done on a Cyber 750 computer. This section describes the software used on the Cyber 750. Figure 2 is a flow chart of the computer programs and magnetic tape and disk storage.

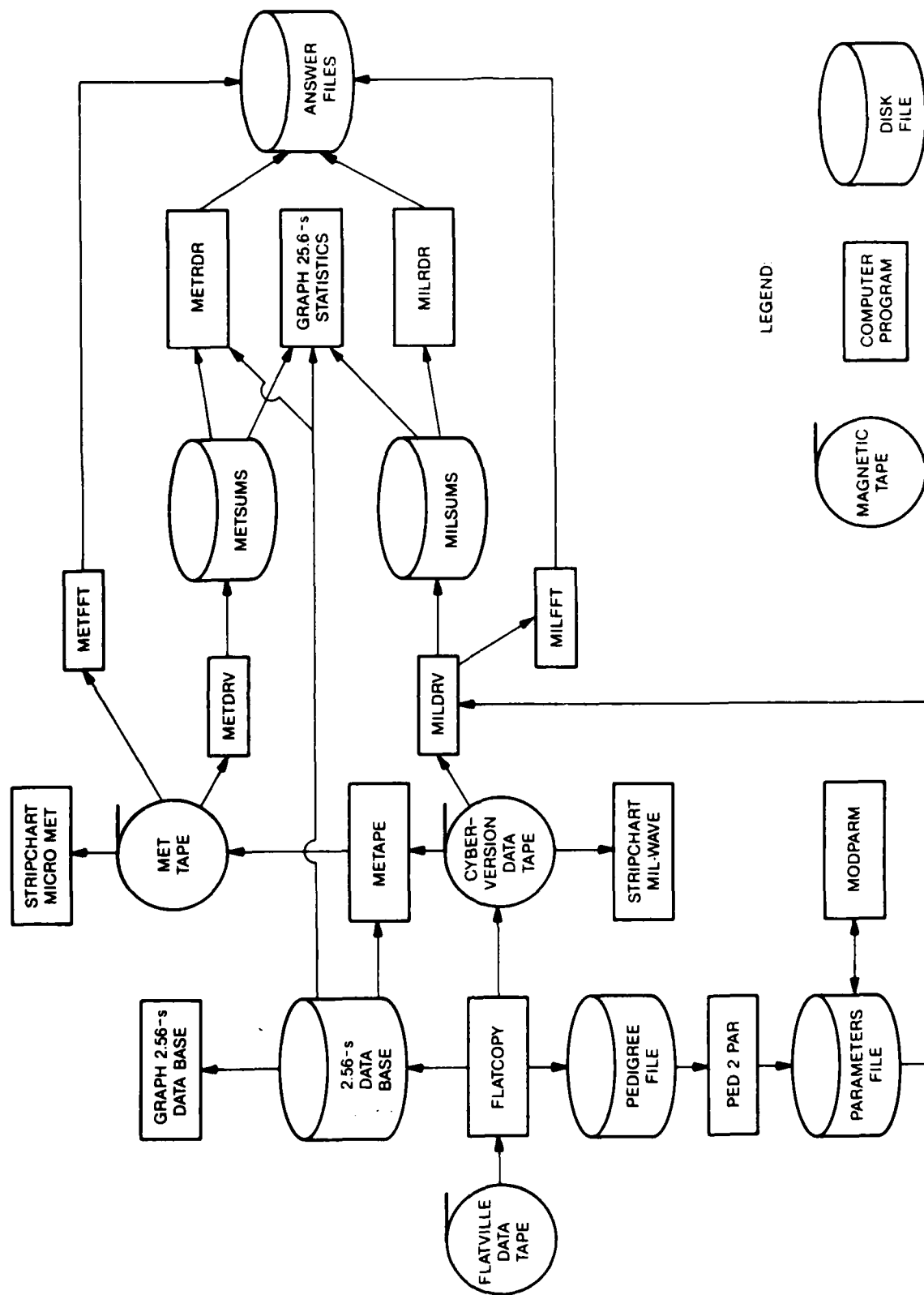


Figure 2.--Overview of the data processing software.

5.2 FLATCOPY

The first step in Cyber processing is program FLATCOPY shown on Fig. 2. FLATCOPY reads the 1600-bpi Flatville data tape (the copy made on the PDP-11/70), which has 1024 words per block, converts the data to 60-bit words, and writes the results to the 6250-bpi Cyber-version data tape. It is this translated Cyber version that is efficiently read by the Cyber 750 in subsequent processing. By using 6250 bpi and blocks of 4096 words, a single Cyber-version magnetic tape contains almost all of the data from a Flatville data tape; the remaining data, if any, are discarded.

FLATCOPY also replaces the missing sync bytes and data frames, and locates the missing data blocks. The times of occurrence of skipped data frames and of the approximate first and last times bracketing a block loss are written to a disk file known as the pedigree file; this file is shown on Fig. 2. The pedigree-file information is used in subsequent processing.

FLATCOPY also extracts the 0.39 Hz data and averages the Lyman- α voltage counts as well as platinum resistance-wire temperatures into 2.56-s bins. This information is written to a 2.56-s meteorological data base disk file that is used in subsequent processing. This 2.56-s data base disk file is shown on Fig. 2. The following processing of 0.39-Hz data occurs in FLATCOPY. The optical disdrometer data are converted to drop-size distribution and the rain rate in volts; both are recorded every 2.56 s in the disk file. The V α is α l α signals are converted to temperature in Celsius and to both relative humidity and absolute humidity, and recorded every 2.56 s in the disk file. The barometer signal is converted to millibars and likewise sent to the 2.56-s disk file. Every 2.56 s, the psychrometer wet- and dry-bulb temperatures are derived in Celsius; absolute humidity is also obtained, and all three are written to disk. Psychrometer data are rejected if a frame replacement occurred during the psychrometer commutation cycle; otherwise, spurious results would be obtained. The optical cross-wind and C_n^2 meter data are obtained every 2.56 s in units of meters per second and $m^{-2/3}$ and likewise written to the disk file. The angle encoder's angles in degrees as well as the vane angles averaged in 2.56-s bins and prop-vane wind speeds averaged in 2.56-s bins are written to the 2.56-s data base.

For the fourth and fifth experiment sessions additional optical instrumentation was deployed and their outputs are converted to engineering units and

written to the 2.56-s data base. One such instrument was an additional optical cross-wind and C_n^2 meter at a lower height directly beneath the station 2 optical cross-wind and C_n^2 meter. The purpose is to measure shear in the optical cross wind. Another pair of optical sensors, a He-Ne laser scintillometer with a large-aperture, modulated LED scintillometer, are used together to obtain the inner scale of turbulence. The nominal C_n^2 values obtained from both scintillometers using inertial-range formulas for their log-amplitude variances are recorded in the 2.56-s data base as are the resulting optical inner-scale values.

For rain, fog, snow, or blowing snow the 2.56-s data base contains all of the NOAA meteorological information. An exception is experiment session 5, during which the Lyman- α hygrometer and its resistance-wire thermometer are shielded from precipitation in an attempt to measure the turbulence fluctuations during precipitation events. For clear-air conditions, data from the sonic anemometer, Lyman- α hygrometer, and resistance-wire thermometers must also be analyzed; this is discussed in the following sections.

5.3 METAPE

Program METAPE reads the 100-Hz and 25-Hz micrometeorological data from the Cyber-version data tape, effects cures to the sonic anemometer problems, converts the signals to engineering units, and writes the results to a meteorological working tape. This MET tape is shown in Fig. 2. To this end it also reads the 2.56-s data base disk file and performs whole-tape averages of the temperature, humidity, and Lyman- α voltage counts; these quantities are used in the conversion-to-units for the sonic anemometers and Lyman- α hygrometers. The output to the MET working tape consists of all of the resistance-wire temperatures and Lyman- α humidities written at 100 Hz, as well as the solar flux, sonic wind components, sonic horizontal wind speeds, prop-vane wind speeds and angles written at 25 Hz; all these quantities are written in engineering units. In addition, two flags are written at the 25-Hz rate to the MET working tape; these flags designate whether or not the wind angle at the sonic anemometer lies within the $\pm 45^\circ$ acceptance range of the sonic-axis configuration. These flags are used in later processing to reject sonic data for wind angles beyond $\pm 45^\circ$.

The handling of the sonic data is particularly complex. Program METAPE first reads the sonic components and prop-vane signals from the Cyber-version

data tape. If necessary, the sonic signals are despiked in intervals of 40.96 s of data at a time and then converted to units of meters per second. The prop-vane signals are likewise converted to wind speed in meters per second and to angle in degrees. These results are written to a temporary disk file. Meanwhile the averages in (84) are computed so that the sonic offsets can be determined as discussed in Sec. 4.4. When the entire Cyber-version data tape has been thusly processed, the offsets for the horizontal sonic wind components are obtained from (84). The exhausted Cyber tape is now rewound and read from the beginning to provide the resistance-wire temperatures, Lyman- α humidities, and solar flux. Simultaneously, the temporary disk file is rewound and read to provide the prop-vane speeds and angles already converted to units and the despiked sonic wind components. The sonic offsets are then subtracted from their respective components. Note, however, that determining the sonic offsets by comparison with the prop-vane anemometer is an option that is not used in processing every data tape; alternatively, the offsets from the field log can be used. At the 25-Hz rate the angle between the horizontal wind vector and each sonic axis is calculated and used to correct the sonic components for their wake averaging and to set the flags designating whether or not the wind angle is within the $\pm 45^\circ$ acceptance range. The wake-averaging correction is given by Kaimal (1980b). Although the wake of one sonic transducer crosses the second sonic axis when the wind angle is beyond $\pm 45^\circ$, wind tunnel tests of a related sonic anemometer by Hanafusa et al. (1980) show no effect on the wind measured along this second sonic axis. Using the wake correction gives us confidence in the $\pm 45^\circ$ acceptance angle. The horizontal sonic components are converted to orthogonal components as described in Sec. 3.2. The horizontal wind speed is calculated from the latter sonic components. Finally the data are written to the MET working tape.

5.4 Stripchart Data Visualization

We now discuss the programs in Fig. 2 labeled GRAPH 2.56-s DATA BASE, STRIPCHART MIL-WAVE, and STRIPCHART MICRO MET. These programs check the data validity and yield the time intervals that we must delete from further processing because of erroneous data. All graphs are produced on microfilm so that the enormous amount of graphical information can be conveniently stored.

In Sec. 5.2 we discussed all of the quantities that program FLATCOPY archived in the 2.56-s data base disk file. The program labeled GRAPH 2.56-s DATA BASE in Fig. 2 makes a graph of each of these quantities versus time during the data run, and one point is plotted for each 2.56 s. In addition it graphs the averaged rain-drop size distribution. It also graphs all of the temperatures on a single graph; these are the four 2.56-s-averaged resistance-wire temperatures and the two dry- and wet-bulb psychrometer temperatures as well as the two Väisälä temperatures. These graphs show us the trends in temperature, humidity, optical C_n^2 and cross wind, rain rate, solar flux, and even barometric pressure. At this point the malfunction of instruments becomes evident. For instance, the fact that the wet bulb in the psychrometer at station 2 is actually dry is evident in session 1, and program METAPE is then commanded to use the humidity from the psychrometer at station 1 to convert the Lyman- α signals from station 2 to physical units. The failure of one of the optical cross-wind and C_n^2 meters is evident in session 1. The trends in temperature reveal whether such trends will dominate temperature variance calculated over the entire data tape.

The program labeled STRIPCHART MIL-WAVE in Fig. 2 produces a stripchart of the six phase differences and four intensities on one microfilm stripchart; 10 s of data is displayed in each frame. A related program can produce a stripchart of the raw mm-wave voltage squares if need be. These stripcharts reveal the presence of phase-lock losses, spikes, step changes, or other problems in the mm-wave data. The time intervals to be skipped in subsequent processing are obtained from these stripcharts. The program also produces printed summaries of the averages, rms, and extrema of the 10 quantities in 100 s intervals. In addition, averages and rms of the 10 quantities are also produced for 20-s intervals and are graphed with the entire data run displayed on single graphs for each of the quantities. These latter graphs display the trends in the mm-wave data.

The program labeled STRIPCHART MICRO MET in Fig. 2 is actually two programs. One produces a single microfilm stripchart for data from the four resistance-wire thermometers and two Lyman- α hygrometers at the rate of 10 s per frame. The second produces stripcharts of the u, v, w components of the sonic anemometers and overplots on these the corresponding u and v components calculated from the prop-vane anemometers; this gives 10 curves per stripchart

at a rate of 20 s per frame. These stripcharts yield the time intervals to be skipped in later processing in case of erroneous data. As with the mm-wave stripcharts, summaries are printed of 100-s averages, rms, and extrema, and 20-s averages and rms are plotted for each quantity to reveal trends. The extrema are used to set the minimum and maximum bins for the probability distribution function calculations.

5.5 PED 2 PAR and MODPARM

Several parameters are needed for the processing of the data. These include times bracketing erroneous data that is to be skipped during processing, the location of spikes, the integration period to be used, etc. In addition, missing block locations obtained from the pedigree file must be provided to the processing programs. A compact file called the parameters file has been defined to retain these parameters for each tape to be processed. Two programs create, modify, and/or display the contents of the parameter file. These are labeled PED 2 PAR and MODPARM in Fig. 2.

The PED 2 PAR program allows two modes of operation. If a non-empty pedigree file is provided, then PED 2 PAR reads the file and extracts from it the timing data identifying missing data blocks. PED 2 PAR searches the parameters file for the times to be skipped during processing and either replaces the missing block times if there is an existing entry or makes a new entry if there is not. In the second mode of operation, PED 2 PAR displays the missing-block data for all data tapes in the parameters file in both absolute time (Greenwich Mean Time) and time relative to the beginning of the tapes.

The MODPARM program allows interactive access to the parameters file. The program first attempts to read the file and verify that the version of the file is at least the minimum needed for the current version of the MODPARM program. MODPARM then presents a menu from which to choose the data tape of interest and those parameters from that tape that the user wishes to inspect or modify. The program then displays the current values of the parameters, and the user is given an opportunity to modify them, thereby altering the parameters file. An example of modifying the parameters file is to enter the beginning and ending times of intervals to be skipped in subsequent processing; identification of such time intervals using our stripcharts was discussed in the previous section.

As shown in Fig. 2, the parameters file is read by the MILDRV program to obtain the parameters needed for performing its processing steps. The output file MILSUMS contains a copy of the values of the parameters file so that a record is available to confirm the validity of parameters used in processing.

5.6 MILDRV and METDRV

The quantities calculated as averages from the mm-wave and micrometeorological data were discussed in Secs. 2.2 to 2.6 and in Sec. 3.3. These quantities are calculated as running sums (rather than averages) in the programs MILDRV and METDRV for the mm-wave and micrometeorological data respectively. The advantages of outputting running sums over time intervals much shorter than a data run will become clear in the next two sections. As shown in Fig. 2, MILDRV reads the data from the Cyber-version tape and outputs the running sums to a disk file called MILSUMS, and METDRV reads the MET tape and outputs to METSUMS (actually METSUMS consists of several distinct disk files). We output the running sums for specified averaging periods; at present we use 25.6-s periods. The one exception is the structure parameters, which we output as averages. Also, the extrema found in each 25.6-s period are recorded in the disk files. The PDFs and JPDFs are also calculated by MILDRV and METDRV and written to the disk files as unnormalized histograms. The number of points summed is also written to these disk files; this number is variable because erroneous data are skipped, and it is different for mm-wave data versus micrometeorological data. This number can differ between micrometeorological stations because only one station may have erroneous data that is skipped, and different statistical quantities from a given station may have different numbers of points summed because sonic data may be dropped due to wind angles outside the $\pm 45^\circ$ acceptance range and because only some statistics depend on sonic data. The data reduction in MILDRV and METDRV obviously depends on the stripcharts in an essential way because the stripcharts yield the time intervals containing erroneous data that is to be skipped.

It is MILDRV that cures problems in the mm-wave data, as discussed in Sec. 4.3. MILDRV calculates the polynomial-fit correction to all 28 mm-wave channels and synthesizes I_4 for experiment session 1. MILDRV also performs the digital filtering needed to remove erroneous trends in the mm-wave data, and to remove high-frequency noise and noise due to vibration of the I-beam holding the mm-wave receivers.

MILDRV has a second mode of processing in support of the mm-wave fast Fourier transform program, MILFFT. In this mode MILDRV reads the Cyber-version data tape, performs the polynomial-fit correction to the 28 mm-wave channels, synthesizes I_4 if session 1 data are used, and calculates the phase differences. However, in this mode MILDRV does not perform any digital filtering. In so doing, MILDRV uses the parameters file to locate erroneous or lost data and thereby identify all sequential 5.12-s intervals of temporally continuous data. The four intensities and six phase differences are then output to a temporary disk file spanning the entire data tape in blocks of 5.12-s duration. This temporary disk file contains gaps caused by erroneous or lost data. A new 5.12-s block is attempted beginning with the first good datum following erroneous or lost data. Thus the temporal extent of a gap is from the end of one 5.12-s block to the next good datum that is followed by 5.12 s of temporally-continuous and error-free data. The temporary disk file is used by MILFFT.

5.7 Graphing the 25.6-s Statistics

The program labeled GRAPH 25.6-s STATISTICS in Fig. 2 is actually two programs; one graphs the results in MILSUMS and the other those in METSUMS. This program takes the running sums in the disk files, produces averages by dividing by the appropriate number of points summed, converts such quantities as mean squares to more meaningful quantities like central variances, and finally graphs these quantities versus time with one point every 25.6 s per statistic.

At this point these graphs give us a look at the trends in all of our statistics, only a few of which are redundant with the trends visualized in the previous graphing of the 2.56-s data file and the stripcharting. The graphs of the extrema are particularly sensitive to erroneous data that might have eluded us or were wrongly included because the time intervals skipped were incorrect when the data were input to MILDRV or METDRV. If an error is found, the runs of MILDRV and/or METDRV can be repeated.

MILSUMS and METSUMS are repairable files. If an error occurs in a 25.6-s bin, then MILDRV or METDRV can recalculate just this one bin without reprocessing the entire MET or Cyber-version tapes. It is then possible to rewrite the MILSUMS or METSUMS files including the corrected 25.6-s bin.

We check these graphs for statistical stationarity and specify times t_1 to t_2 over which the statistics are sufficiently stationary. A given data tape may have more than one period of stationarity without being stationary as a whole. An extreme example would be a data tape that consists of clear-air data for part of the run but rain data over the remainder of the run. In this case we can use the graphs to specify times t_1 to t_2 for later accumulating the clear-air data and times t_1' to t_2' for accumulating the rain data. By studying these graphs, we can include or exclude data at will in subsequent processing.

5.8 MILRDR and METRDR

Given an interval t_1 to t_2 of stationary statistics as described in the previous section, the programs labeled MILRDR and METRDR on Fig. 2 read the disk files MILSUMS and METSUMS and sum the 25.6-s partial sums from t_1 to t_2 while also summing the numbers of points in each 25.6-s partial sum. These total sums from t_1 to t_2 are converted to averages by dividing by the total number of points summed, and quantities like mean squares are converted to more meaningful quantities like central variance. The PDFs and JPDFs stored for each 25.6 s are summed and then normalized. The extrema of the 25.6-s data are found. The resulting averages (which include such quantities as variances and cross-correlations), the PDFs and JPDFs, and the extrema are identical to those that we could calculate from t_1 to t_2 if we skipped the intermediate step of storing 25.6-s running sums and histograms. The exceptions to this identity are the structure parameters that are stored in the disk file METSUMS as averages. METRDR then averages these 25.6-s-averaged structure parameters from t_1 to t_2 . This is actually an advantage for the time-lagged structure parameters because wind speed variability is less on a 25.6-s time interval than from t_1 to t_2 , and the relationship between time-lagged and spatial structure parameters relies on wind speed stationarity.

Final normalizations of mm-wave data are performed by MILRDR. For instance, the MCF and fourth moments of the field are converted to their normalized values, as discussed in Secs. 2.5 and 2.6.

Finally, MILRDR and METRDR write the accumulated statistics to the disk file labeled ANSWER FILES in Fig. 2. The answer files may contain only one set of statistics for a given data tape if only one set of times t_1 and t_2 is

specified, but it may contain additional sets if additional times t_1' and t_2' are specified. We have already noted the advantages of data validation and data selection in creating the files METSUMS and MILSUMS of 25.6-s running sums. In addition, this partial sum procedure allows additional processing of differing sets of times t_1 to t_2 to be performed in the distant future without recalculation at the high data rates of 100 Hz and 25 Hz.

5.9 MILFFT and METFFT

Sections 2.9 and 3.9 describe what spectra and cross-spectra are calculated and how this is accomplished for mm-wave and micrometeorological data, respectively. The programs MILFFT and METFFT in Fig. 2 accomplish these transforms and write the averaged results to the answer files. In addition, mm-wave spectra that are not averaged in frequency bins are saved and examined so that noise in the mm-wave intensities and phase differences can be identified for subsequent filtering done by MILDRV in producing the MILSUMS file.

Section 5.6 describes the temporary disk files created by the second mode of MILDRV processing. These files are then read by MILFFT to produce the Fourier transforms. METFFT creates its own analogous disk files for Fourier transformation without a second mode of processing that exists within METDRV. METFFT does not use the parameters file and therefore cannot transform data tapes that have block drops; data tapes preceding tape 12 of session 2 are therefore excluded. However, times bracketing bad data observed on the micrometeorological stripcharts are entered so that bad data do not enter the disk files to be transformed.

In this mode METFFT reads the MET working tape and outputs 5.12-s blocks of temporally-continuous error-free data to four temporary disk files. The choice of these 5.12-s blocks and the temporal extent of gaps between them, if any, is the same as for MILDRV in Sec. 5.6 (except block drops are not considered). There are two disk files for each micrometeorological station. One file holds the 100-Hz data, namely the temperatures from the two resistance-wire thermometers and the Lyman- α hygrometer. The other file holds the 25-Hz data, namely from the three axes of the sonic anemometer and the three 100-Hz quantities averaged by fours to produce 25-Hz data. The temporal integrity of the 100-Hz data derives from any errors within the 100-Hz data, whereas that of the 25-Hz data derives from errors in both the 100-Hz data and the sonic

anemometers and from the wind angle being outside the cone of acceptance for the sonic anemometer.

Once the mm-wave or micrometeorological disk files are created, MILFFT and METFFT use the same versatile Fourier transform program to produce spectra. The data are read from these files in sets of 40.96 s of continuous data, that is, eight 5.12-s blocks that have no gaps between them. The FFT is performed on a pair of quantities simultaneously and written to another temporary disk file, then another pair is read from the first file, and so on. The user can select a given number of available 40.96-s intervals, and each is Fourier transformed and written to disk. These transforms are read from the disk. The desired power spectra and cross-spectra are formed for each 40.96-s interval and are then averaged together to increase statistical reliability. These spectra still retain their full dependence on frequency and can be graphed to diagnose instrument problems and/or saved in a permanent disk file. Such graphs are especially important for further mm-wave processing because the frequencies and strengths of the various types of noise in the mm-wave data must be identified for subsequent digital filtering before the MILSUMS file is written. Finally, the spectra are averaged into logarithmically spaced frequency bins and graphed as well as written to the answer files.

To produce the low-frequency Fourier transform, the data in the temporary disk file described in Sec. 5.6 are low-pass filtered with a single-pole RC-type filter and then averaged into bins of about 0.6 s such that there are 4096 temporal bins per data tape or per given section of a data tape. The gaps between the 5.12-s blocks are filled with interpolated values. These data are then Fourier transformed in pairs of quantities, as for the high-frequency FFT, and written to a temporary disk file. When all pairs have been transformed, the desired power spectra and cross-spectra are formed and corrected for the effects of low-pass-filter and bin averaging. These spectra are then averaged into logarithmically spaced frequency bins, graphed, and written to the answer files.

5.10 Using the Answer Files

The set of all answer files from all data tapes provides a very versatile data base for interpreting the data and preparing publications. This flexibility is the desired end product alluded to in Sec. 1. Computer programs can

be written and modified to present the reduced data in any graphical or tabular manner desired. For instance, programs can be written to plot all the MCFs versus antenna spacing for the clear-air data, with one curve for each desired refractive-structure parameter value, then alternatively plotted versus antenna spacing scaled by a theoretical wave coherence length. Alternatively, these clear-air MCFs could be plotted for various values of surface-layer stability rather than refractive-structure-parameter values. The MCFs from turbulence, rain, fog, and snow data could all be plotted on a single graph for comparison by accessing the answer files for these diverse meteorological conditions. One could tabulate all of the temperature and humidity structure parameters and cross-structure parameters from the various different methods of calculating them (spatial, time-lagged, optical scintillation) to search for data consistency or errors. Clearly these examples are insignificant compared with the myriad relationships that could be investigated using the answer files.

5.11 Archiving of Disk Files

The Cyber-version data tape and MET tape are, of course, magnetic tapes and can therefore be stored for further processing as long as desired or practical. The various disk files in Fig. 2 cannot reside on disk indefinitely because of disk-storage costs. Consequently, the 2.56-s data base file as well as the MILSUMS and METSUMS files are dumped to magnetic tape and deleted from disk after the answer files are made. Thus these files can be returned to disk if further data processing is desired in the future. Likewise, the answer files are dumped to magnetic tape and deleted from disk when desired. It is expected that the magnetic tapes for the answer files will be retained indefinitely.

6. REDUCED MILLIMETER-WAVE AND MICROMETEOROLOGICAL DATA

6.1 Introduction

As an example of our data processing results, we present reduced data from the answer files of data tapes 20, 22 to 25, and 27 of experiment session 1. It should be remembered that the intensity at antenna 4 is synthesized, as

discussed in Sec. 4.3. The probability distribution functions are normalized to unit area under a curve connecting the histogram peaks. That is, the sum of the probability over all bins is made equal to the number of bins divided by the range of the independent variable.

6.2 Tabular Results

Tables 4 and 5 are mm-wave statistics averaged over the whole of session 1 for tapes 24 and 20, respectively. In interpreting these results one should keep in mind that the root-mean-square (rms) intensity decreased by 30% in an almost linear fashion over the duration of tape 20 data, with a much less dramatic change in rms phase differences. On the other hand, tape 24 had nearly constant rms intensities and rms phase differences.

As expected, the intensity variance is much less than unity. Ideally all four antennas should give equal variances. Agreement is good, but the synthesized intensity at antenna 4 gives the least agreement for tape 24. The minimum and maximum intensities are normalized by dividing by the mean intensity. Table 4 shows that over the whole of tape 24 the intensities swung from about 0.5 to greater than 1.5 of the mean intensity.

The phase variances in these tables differ from one antenna pair to the next, as they should because of the differing antenna separations. The minimum and maximum phase differences likewise show corresponding variability. As seen in Table 4, the largest observed phase differences exceeded 3 radians. The mixed intensity-difference and phase-difference correlation given in Eq. (7) is very much smaller than either the intensity variance or phase-difference variance. Thus amplitude and phase are relatively uncorrelated. The phase-type figures of merit are much smaller than any of the phase-difference variances; this verifies the consistency of the phase-difference measurements.

The ρ -type figures of merit in Tables 4 and 5 suggest that the MCF should not be trusted to better than about 5% accuracy. In Tables 4 and 5 the ρ type and Σ type are close to unity, as desired, even for antenna pairs 3, 5, and 6, which use the synthesized intensity at antenna 4. The variances of both ρ -type and Σ -type figures of merit show that there is very little temporal variation about the mean values of these figures of merit.

Table 4.--Millimeter-wave statistics from the answer files
obtained by averaging all of tape 24 of session 1, July 1983

<u>Intensity Statistics</u>			
Antenna number	Intensity variance	Normalized minimum intensity	Normalized maximum intensity
1	0.0210	0.540	1.70
2	0.0219	0.523	1.74
3	0.0216	0.423	1.75
4	0.0287	0.433	1.74

<u>Phase Difference Statistics</u>				
Antenna pair	Phase- difference variance	Minimum phase difference	Maximum phase difference	Eq. (7)
1	0.081	-1.32	1.08	-7.12 (-6)
2	0.315	-2.46	2.37	-8.54 (-6)
3	0.703	-3.25	3.09	-1.50 (-5)
4	0.193	-1.67	1.75	-7.90 (-6)
5	0.563	-3.24	2.87	-9.86 (-6)
6	0.408	-2.47	2.29	-4.87 (-6)

<u>Figures of Merit</u>				
Antenna pair	ρ type	ρ -type variance	Σ type	Σ -type variance
1	1.07	2.85 (-5)	1.10	4.66 (-4)
2	1.05	4.48 (-4)	1.03	7.41 (-4)
3	1.02	5.85 (-5)	0.934	3.13 (-3)
4	1.03	2.57 (-4)	1.01	2.06 (-3)
5	1.00	3.61 (-5)	0.944	4.18 (-3)
6	0.976	8.43 (-5)	0.869	1.75 (-3)

Antenna numbers	Phase type (a variance)
1&2&4	8.16 (-4)
1&3&5	2.51 (-3)
2&3&6	1.36 (-3)
4&5&6	9.24 (-4)
1&3&4&6	2.49 (-3)

Note: Numbers in parentheses indicate powers of 10.

Table 5.--Millimeter-wave statistics from the answer files
obtained by averaging all of tape 20 of session 1, July 1983

<u>Intensity Statistics</u>			
Antenna number	Intensity variance	Normalized minimum intensity	Normalized maximum intensity
1	0.0059	0.694	1.34
2	0.0046	0.716	1.26
3	0.0066	0.638	1.43
4	0.0066	0.635	1.34

<u>Phase Difference Statistics</u>				
Antenna pair	Phase- difference variance	Minimum phase difference	Maximum phase difference	Eq. (7)
1	0.024	-0.58	0.68	-2.06 (-6)
2	0.104	-1.32	1.19	-3.59 (-6)
3	0.193	-1.50	1.74	-1.50 (-6)
4	0.063	-1.13	1.02	-2.18 (-6)
5	0.163	-1.54	1.41	-7.09 (-7)
6	0.131	-1.41	1.38	-1.45 (-6)

<u>Figures of Merit</u>				
Antenna pair	ρ type	ρ -type variance	Σ type	Σ -type variance
1	0.979	1.27 (-4)	0.89	1.28 (-3)
2	1.00	7.10 (-5)	0.88	1.16 (-3)
3	0.964	1.10 (-4)	0.81	1.53 (-3)
4	1.04	1.71 (-4)	1.06	3.02 (-4)
5	1.01	1.96 (-4)	1.02	1.75 (-3)
6	1.02	4.34 (-4)	0.99	6.05 (-3)

Antenna numbers	Phase type (a variance)
1&2&4	3.00 (-4)
1&3&5	5.83 (-4)
2&3&6	4.99 (-4)
4&5&6	8.57 (-4)
1&3&4&6	4.93 (-4)

Note: Numbers in parentheses indicate powers of 10.

Table 6 is a summary of the micrometeorological data from tape 24, which were taken at about 11:30 a.m, July 1983. These averages were obtained from 480 s into the run to its end at 2400 s. The values of the structure parameters imply that the humidity structure parameter overwhelmingly dominates the calculated mm-wave refractive-index structure parameter. The values of temperature structure parameters from optical and fine-wire instruments are in excellent agreement. The small but nonzero value of the mean of the cross-stream wind component is a measure of the inaccuracy of determining the true streamwise direction.

6.3 Graphical Results

Figure 3 shows the intensity probability distribution function (PDF) for antenna 1 for session 1, tape 24. Gaussian and lognormal PDFs having the same mean and variance are also plotted. There is little difference between the Gaussian and lognormal PDFs for such small values of variance. However, the data are clearly skewed and more nearly follow the lognormal PDF, as is expected theoretically.

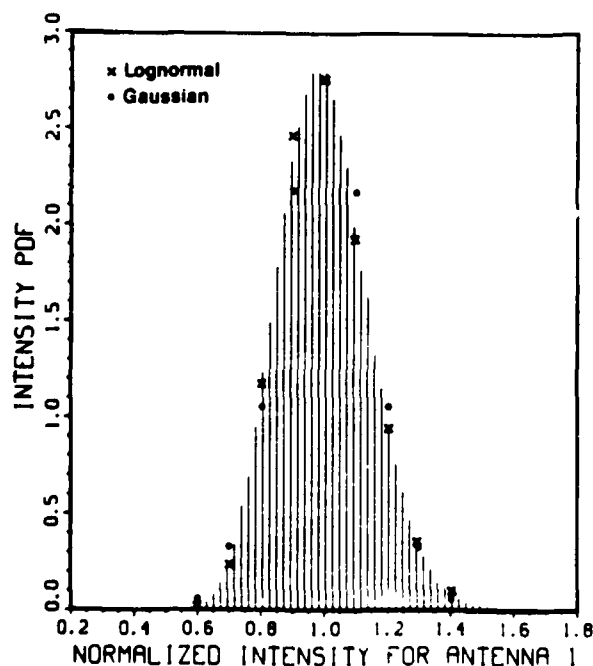


Figure 3.--Probability distribution function of intensity for antenna 1, session 1, tape 24, July 1983. Gaussian and lognormal distributions are also shown. Normalized intensity is scaled to unit mean value. The distribution is normalized to unit area under the histogram.

Table 6.--Summary of micrometeorological data from tape 24,
taken at 11:30 a.m., July 1983

Average Values	
Humidity	19 g/m ³
Temperature	32°C
Wind speed	5.3 m/s
Wind angle	10°
Pressure	993 mb
Solar flux	94% of full sun
Wind stress	-0.14 (m/s) ²
Humidity flux	0.1 (g/m ²)/s
Temperature flux	0.03°C m/s
Stability	-0.03
Square Roots of Variances	
Humidity	0.72 g/m ³
Temperature	0.35°C
Wind speed	1.2 m/s
Wind angle	11°
Streamwise wind component	1.1 m/s
Cross-stream wind component	1.0 m/s
Vertical wind component	0.54 m/s
Structure Parameters	
C_n^2 from optical scintillometers	$2 \times 10^{-13} \text{ m}^{-2/3}$
C_T^2 from optical C_n^2	$0.03^\circ\text{C}^2 \text{ m}^{-2/3}$
C_T^2 from resistance wires	$0.03^\circ\text{C}^2 \text{ m}^{-2/3}$
C_q^2 from Lyman- α hygrometers	$0.2 (\text{g/m}^3)^2 \text{ m}^{-2/3}$
C_{Tq} from resistance wires and Lyman- α hygrometers	$0.075^\circ\text{C} (\text{g/m}^3) \text{ m}^{-2/3}$
C_n^2 for radio frequencies*	$5.9 \times 10^{-12} \text{ m}^{-2/3}$

*Obtained from Eq. (79), using C_T^2 , C_n^2 , and C_{Tq} from the resistance-wire thermometer and Lyman- α hygrometer with A_T and A_q obtained from the radio refractive-index equation.

Figure 4 shows the phase-difference PDF for antenna pair 4 of session 1, tape 24. A Gaussian PDF having the same mean and variance is also plotted. Clearly the phase difference is Gaussian, as is expected theoretically.

Figure 5 shows the structure function of phase versus receiver separation. Tape 20 corresponds to the 6:50 p.m. data and tapes 22 to 27 correspond to times 8:40 a.m. to 3:50 p.m. of the following day. The six receiver separations correspond to the six antenna pairs. At a given receiver separation, the value of the structure function of phase is just the phase-difference variance for the corresponding antenna pair. Also plotted is a theoretical prediction for the 6:50 p.m. data assuming a 14-m horizontal outer scale.

Figure 6 shows the modulus of the mutual coherence function; the 3:50 p.m. data of tape 27 are not included. Since the intensity PDF is lognormal and the phase-difference PDF is Gaussian, it follows theoretically that the MCF should equal $\exp(-D/2)$ where D is the sum of the structure functions of log-amplitude and phase; this relationship is satisfied to within 0.5% in the mm-wave data. Although not shown, the imaginary part of the MCF is very much smaller than the real part, as is expected theoretically.

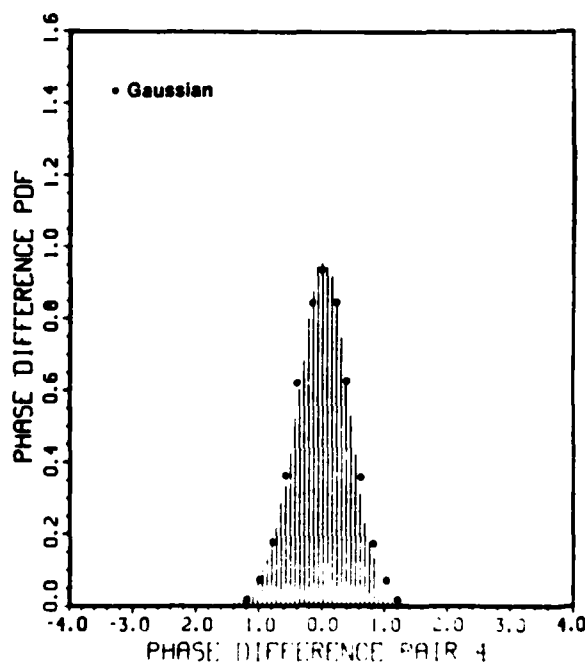


Figure 4.--Probability distribution of phase difference in radians for antenna pair 4, session 1, tape 24, July 1983. A Gaussian distribution is also shown. This distribution is normalized to unit area under the histogram.

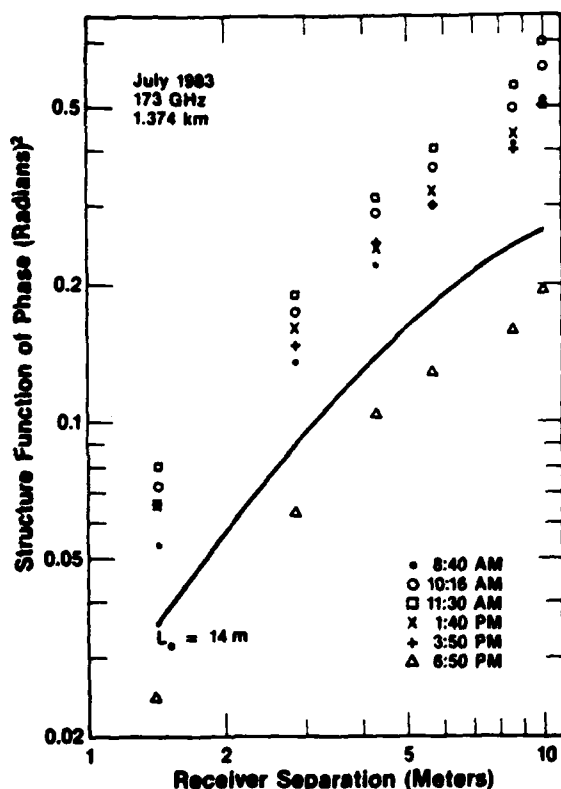


Figure 5.--The structure function of phase. The solid line represents a theoretical prediction for the 6:50 p.m. data, assuming a 14-m horizontal outer scale.

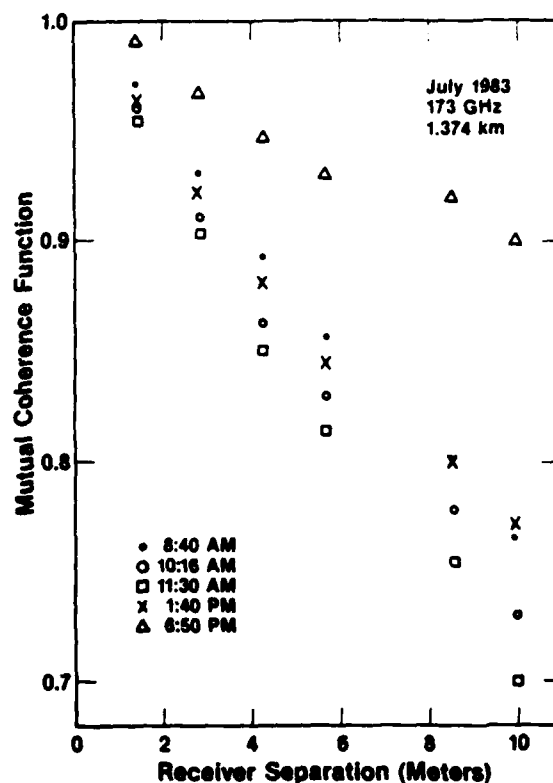


Figure 6.--The modulus of the mutual coherence function.

Figure 7 shows the normalized intensity variance plotted versus its theoretical formula for inertial-range turbulence. Here, C_n^2 is deduced from the micrometeorological data. The straight line shows agreement with theory. Lack of agreement could be caused by the outer scale of turbulence or inaccurate calibration of the Lyman- α hygrometer.

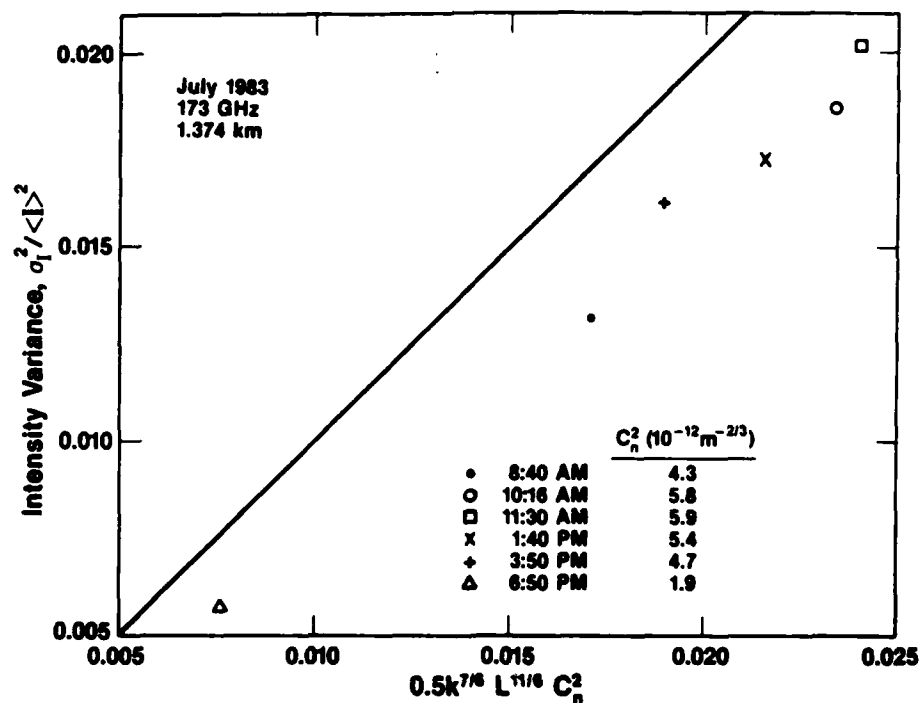


Figure 7.--The normalized variance of intensity versus its inertial-range formula. The straight line shows theoretical calculations.

7. ACKNOWLEDGMENTS

This work was supported by the Army Research Office under MIPR 122-85. We thank William Moninger for his careful review of the manuscript.

8. REFERENCES

- Hanafusa, T., Y. Kobori, and Y. Mitsuta, 1980. Single-head sonic anemometer-thermometer. The Boulder Low-Level Intercomparison Experiment, Report No. 2, NOAA/ERL, Boulder, CO, 7-13.
- Kaimal, J. C., 1980a. Sonic anemometers. In Air-Sea Interaction: Instruments and Methods. Plenum Press, New York, 81-96.

Kaimal, J. C., 1980b. BAO sensors for wind, temperature, and humidity profiling. The Boulder Low-Level Intercomparison Experiment, Report No. 2, NOAA/ERL, Boulder, CO, 1-6.

Schmitt, K. F., C. A. Friehe, and C. H. Gibson, 1978. Humidity sensitivity of atmospheric temperature sensors by salt contamination. J. Phys. Oceanogr. 8:151-161.

END

DTIC

9-86